Temporal Variability of Strombolian Explosive Activity at Yasur Volcano, Vanuatu

Dissertation

Zur Erlangung des Doktorgrades der Naturwissenschaften im Department Geowissenschaften der Universität Hamburg

vorgelegt von

Kristina Meier

aus

Bückeburg

Hamburg

2014

Als Dissertation angenommen vom Fachbereich Geowissenschaften
der Universität Hamburg

Auf Grund der Gutachten von Prof. Dr. Matthias Hort
und Dr. Joachim Wassermann

Hamburg, den 02.07.2014

Prof. Dr. Christian Betzler
Leiter des Fachbereichs Geowissenschaften

Zusammenfassung

Strombolianische Vulkane gehören aufgrund ihrer dauerhaften Aktivität zu den weltweit meist untersuchten Vulkantypen. Zahlreiche Beobachtungen des Eruptionsverhaltens haben ein zunehmendes Verständnis Strombolianischer Aktivität ermöglicht. Eine systematische Untersuchung von zeitlichen Veränderungen im Eruptionsverhalten steht jedoch noch aus. Bisher wurden ausschließlich Teilaspekte des Ausbruchverhaltens beleuchtet. Ein Großteil der Erkenntnisse gilt zudem alleinig für den italienischen Vulkan Stromboli. Dies begrenzt die Einsicht in die zugrunde liegenden Prozesse. Für ein umfassendes Verständnis ist ein integrativer Ansatz und ein Abgleich mittels Beobachtungen an anderen Vulkanen erforderlich. Aus diesem Grund sollen das Eruptionsverhalten des Mt. Yasur in Vanuatu und die damit verbundenen geophysikalischen Signale in der vorliegenden Arbeit näher untersucht werden.

Hierfür werte ich einen Datensatz von etwas mehr als 58000 Eruptionen aus. Der Datensatz besteht aus Infrarot, Doppler Radar, Infraschall und Seismik Daten und umfasst deutliche Änderungen im Eruptionsverhalten. Aschereiche sowie aschearme Eruptionsformen wurden während der Aufzeichnungen abwechselnd beobachtet. Hierdurch kann erstmalig ein systematischer Zusammenhang zwischen Oberflächenaktivität und aktivem Entgasungsverhalten hergestellt werden. Jede Eruptionsform kann hinsichtlich Materialbewegung, Temperatur und Überdruck beschrieben werden. Der zeitliche Trend in diesen Daten belegt das regimeartige Fortbestehen einer Eruptionsform über Tage hinweg.

Die Interpretation aller Daten zeigt zudem eine starke Ähnlichkeit zwischen den beobachteten Eruptionsformen am Yasur und am Stromboli. Es besteht ein allgemeiner Zusammenhang zwischen Eruptionsform und Eruptionsintensität im Hinblick auf Ejektageschwindigkeit und Überdruck. Die Wellenform der aufgenommenen Infraschallsignale variiert je nach Eruptionsform. Bisher war es üblich hieraus Änderungen der Eruptionsdynamik abzuleiten. Die Modellierung von Infraschallausbreitung unter aschereichen und aschearmen Bedingungen belegt jedoch, dass die hierfür nötige Voraussetzung der gleichmäßigen Wellenausbreitung nicht gegeben ist. Ein umfassendes Verständnis der Ausbreitungsbedingungen ist für eine korrekte

Interpretation der Eruptionsdynamik unerlässlich.

Ich verfolge daher einen generischen Ansatz, um Änderungen im Entgasungsverhalten zu erfassen. Ich betrachte Änderungen in der Eruptionsrate, der Eruptionsintensität sowie in der Inter-Eruptionszeit. Ebenso untersuche ich die zeitliche Struktur der aufgezeichneten Eruptionssequenz. Der gewählte Ansatz erlaubt mir zu zeigen, dass das Entgasungsverhalten von einem nicht-zufälligen Prozess gesteuert wird. Die beobachteten Eruptionsintensitäten und Inter-Eruptionszeiten genügen skaleninvarianten Verteilungen. Die Form dieser Verteilungen variiert in Funktion des Entgasungsverhaltens und steht gleichzeitig in Verbindung mit der beobachteten Oberflächenaktivität. Die skaleninvariante zeitliche Struktur der Eruptionssequenz belegt darüber hinaus, dass Schwankungen im Entgasungsverhalten nicht zufällig erfolgen.

Im Ganzen ermöglichen die am Yasur gewonnenen Ergebnisse neue Einblicke in die Ursprünge Strombolianischer Aktivität. Im Gegensatz zu früheren Arbeiten scheint das Eruptionsverhalten insgesamt weder unveränderlich noch zufällig zu sein. Analoge Untersuchungen am Stromboli bestätigen diesen Befund. Dies schränkt die Modelle für die zugrunde liegenden Mechanismen maßgeblich ein. Die derzeit existierenden Modelle können die erhaltenen Ergebnisse nur bedingt erklären. Ich entwickele daher ein neues Modell, um das Eruptionsverhalten an Strombolianischen Vulkanen zu erklären.

Summary

Owing to their permanent activity Strombolian volcanoes are a matter of frequent research. Numerous studies have shown that variations in explosive style or in activity level bear important information to understand the mechanisms that drive activity. A systematic study of the temporal variability of Strombolian activity is however still outstanding. It is common to focus on individual observations or to limit research to a single volcano. To date almost all findings are confined to Stromboli volcano, Italy. This leads to a biased view and allows only specific insights into the processes driving activity. For a more comprehensive understanding it is necessary to compare various observations at different volcanoes. The main goal of this study is therefore to investigate the activity of Yasur volcano, Vanuatu, and its associated geophysical signals to improve our understanding of Strombolian behavior.

To this end I analyze a continuous data set of about 58000 Strombolian explosions recorded at Yasur in late 2008. The data set consists of infrared, Doppler radar, infrasound and seismic data, and covers a transition in explosive style from ash-rich to ash-free explosions followed by a phase of high ash discharge. Its analysis permits to establish a solid link between surface activity and explosive degassing for the first time. It allows the characterization of each explosive style in terms of material movement, temperature and excess pressure. The joint temporal trend in these data reveals the regime-like persistence of a given explosion form over days.

The interpretation of all data further suggests that explosion types at Yasur overall equal those at Stromboli. With regard to explosion velocity and excess pressure there is a general correlation between explosive style and intensity. In terms of infrasonic waveforms the signal shape varies across explosive regimes. Usually this would be taken as an indicator for a different explosion dynamics. Modeling of infrasound propagation under ash-free and ash-rich conditions however shows that an explicit comparison of waveforms is challenging in the presence of different near-source conditions. A proper comprehension of the propagation setting is essential for a correct interpretation of the explosion dynamics.

I therefore follow a generic approach to capture the variability of explosive gas release: I quantify explosive degassing in terms of explosion rate and intensity as well as in terms of return time. Likewise I study the temporal structure of the recorded explosion sequence. This permits me to show that explosive degassing is controlled by a single, non-random process. Explosion magnitudes and return times feature scale-invariant behavior. Variations in this behavior mirror changes in degassing, and correlate with changes in surface activity. The scale-invariant temporal structure of the explosion sequence moreover demonstrates that temporal fluctuations in degassing are correlated in time.

On the whole the results at Yasur encourage a new view of Strombolian behavior. In contrast to previous work surface activity and explosive degassing result to be neither random nor stationary. Analog observations at Stromboli volcano corroborate this idea. This bears important constraints for our understanding of the mechanisms driving activity. Common models fail to explain all observations. As a consequence I set out to develop a new model for active degassing at Strombolian volcanoes.

Contents

Chapter 1

Introduction

Volcanoes rank among the most impressive natural phenomena, and have always fascinated humans. Accounts of their behavior appear in the mythology of almost all cultures that evolved in their vicinity (*Decker and Decker*, 1991). Yet while being fascinating their eruptions present the largest natural hazard next to earthquakes, floods and storms. Due to their fertile soil volcanic regions are however one of the most densely populated on Earth today (*Small and Naumann*, 2001). As a result a significant number of people is affected by volcanic activity worldwide. Depending on eruption size and style there is a variety of volcanic hazards. These can be either of primary nature directly related to volcanic activity, e.g. lava flows (e.g. *Vicari et al.*, 2011), ash fall (e.g. *Horwell and Baxter*, 2006), pyroclastic flows (e.g. *Belousov et al.*, 2007) and gas avalanches (e.g. *Kling et al.*, 2005), or of secondary form arising from a combination of volcanic and non-volcanic processes, i.e. lahars (e.g. *Waythomas et al.*, 2012), landslides (e.g. *Harris et al.*, 2011) and tsunamis (e.g. *Tinti et al.*, 2006). Besides that major volcanic eruptions may modulate atmospheric chemistry impacting climate on a global scale (e.g. *Robock*, 2002). The systematic study of volcanic hazard is therefore a matter of general concern.

To assess volcanic hazard it is essential to approach it from different perspectives. While socio-cultural studies elucidate habitation patterns, and thus help to determine vulnerabilities of people and assets at risk, volcano monitoring is critical to hazard mitigation (see *Scarpa and Tilling*, 1996). To issue reliable early warnings it is however crucial to understand the way volcanoes work. In general this is tackled by a multitude of approaches. These include investigations of different scientific disciplines such as geology (e.g. *Walker*, 1990), geochemistry (e.g. *Edmonds*, 2008) and geophysics (e.g. *Harris and Ripepe*, 2007a) as well as laboratory and field experiments at different volcanoes (e.g. *Spieler et al.*, 2004; *Marchetti et al.*, 2009). Yet among all active volcanoes there are merely few in permanent eruption. It is

therefore common to focus on a couple of observations and to study single processes in particular (e.g. *Sahetapy-Engel et al.*, 2004; *Chouet et al.*, 2005; *Caplan-Auerbach et al.*, 2008, 2010; *Donnadieu et al.*, 2011; *Spampinato et al.*, 2012). This provides valuable first insights into the forces driving activity. However, putting the results in a more general context is challenging due to the limited amount of information. To draw representative conclusions it is necessary to analyze numerous observations.

It is for this reason that Strombolian-type volcanoes are a matter of frequent research. Their continuous, regular activity allows for numerous observations in a relatively short time span. In contrast to most other volcanoes they further exhibit an open vent that can be directly observed. They offer thus ideal conditions for studying volcanic processes in a comprehensive perspective.

1.1 Strombolian Activity

Volcanic activity of Strombolian-type was first defined at Stromboli volcano, Italy (*Mercalli*, 1881). It is bound to basaltic volcanoes and consists of continuous non-explosive degassing interrupted by recurrent short-lived explosions of gas and incandescent magma (e.g. *Houghton and Gonnermann*, 2008, for review). Explosions generally occur from a small number of long-lived vents that eject between 0.01 and 10 m^3 of pyroclasts to heights of 100 - 200 m (*Cole et al.*, 2005; *Chouet et al.*, 1974; *Ripepe et al.*, 1993; *Barberi et al.*, 1993). At Strombolian volcanoes this 'normal' form of activity is persistent, although it varies in style and intensity. Explosions can be divided into ash-free and ash-rich types depending on the grain size of the ejected material (*Chouet et al.*, 1999; *Ripepe and Marchetti*, 2002; *Patrick et al.*, 2007). Subject to the level of activity explosions may further be less or more frequent and/or intense (e.g. *Harris and Ripepe*, 2007a; *Ripepe et al.*, 2008).

Long-standing research has created a convincing general model to explain this form of activity. Today it is widely agreed that the particular modes of gas release reflect different mechanisms of gas segregation (*Parfitt*, 2004; *Burton et al.*, 2007b; *Namiki and Manga*, 2008). Open-system degassing is associated with non-explosive behavior as gas escapes through permeable pathways inside the conduit (*Allard et al.*, 1994; *Polacci et al.*, 2008). *Burton et al.* (2007b) have stressed the important role of gas percolation in this context. Using constraints from literature data on the petrology and texture of erupted material and geochemical measurements of gas emissions together with a model of gas solubility they developed a conceptual model for quiescent degassing (see figure 1.1). In their model steady-state gas release is sustained via magma circulation of ascending vesiculating and descending degassed magma in

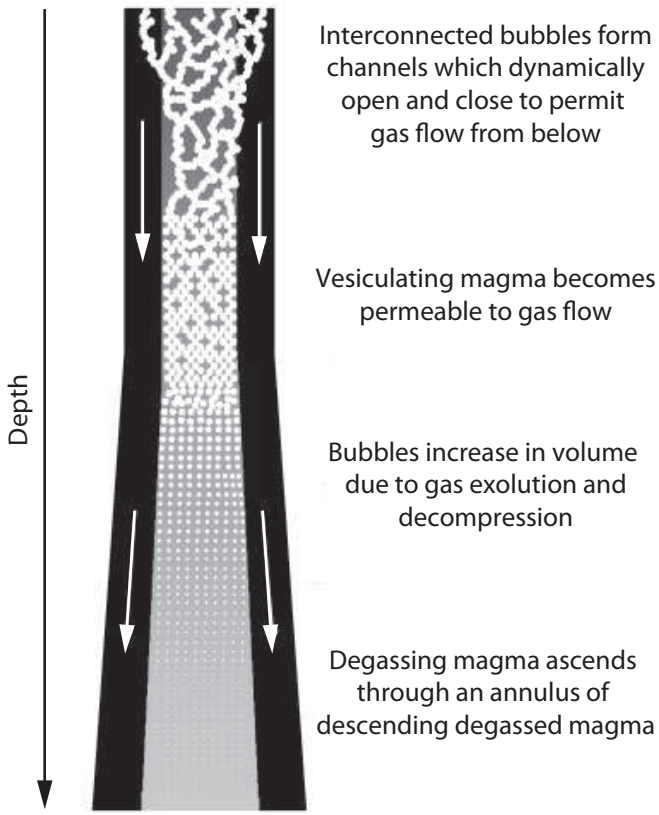

Figure 1.1: Schematic sketch of the current model for quiescent degassing (modified after *Burton et al.* (2007b)). Juvenile magma ascends from depth through an annulus of descending degassed magma. During ascent the void fraction of the magma increases due to gas exsolution and decompression. At a vesicularity of ∼0.5 the magma becomes permeable to gas flow, and interconnected bubbles start to form pathways permitting efficient degassing from below.

the conduit (compare *Kazahaya et al.*, 1994; *Stevenson and Blake*, 1998; *Palma et al.*, 2011). Continuous vesiculation drives the ascending magma towards the percolation transition above which it becomes permeable to gas flow. In this way the transition from closed- to open-system conditions allows for quiescent gas escape without the eruption of magma.

Explosive gas release, in contrast, is driven by gas overpressure (e.g. *Vergniolle et al.*, 1996; *James et al.*, 2009; *Del Bello et al.*, 2012). Explosions are thought to result from the decoupled rise and bursting of pressurized gas slugs at the top of the magma column (see figure 1.2) (e.g. *Chouet et al.*, 1974; *Blackburn et al.*, 1976; *Vergniolle and Jaupart*, 1986; *Ripepe et al.*, 1993; *Burton et al.*, 2007a). The actual mechanism of slug formation is however still a point of debate (see *Parfitt*, 2004, for review). Two models have been derived from mathematical modeling and/or laboratory ex-

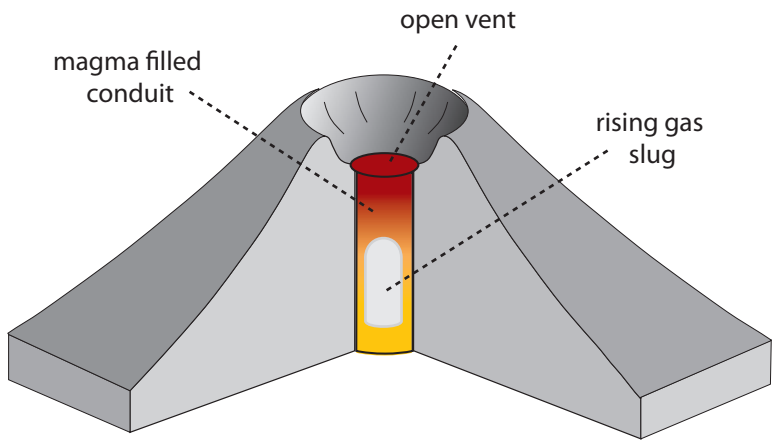

Figure 1.2: Schematic sketch of a gas slug rising in a volcanic conduit (modified after *Gerst* (2010)). Strombolian explosions are thought to originate from the bursting of a slug at the magma free surface.

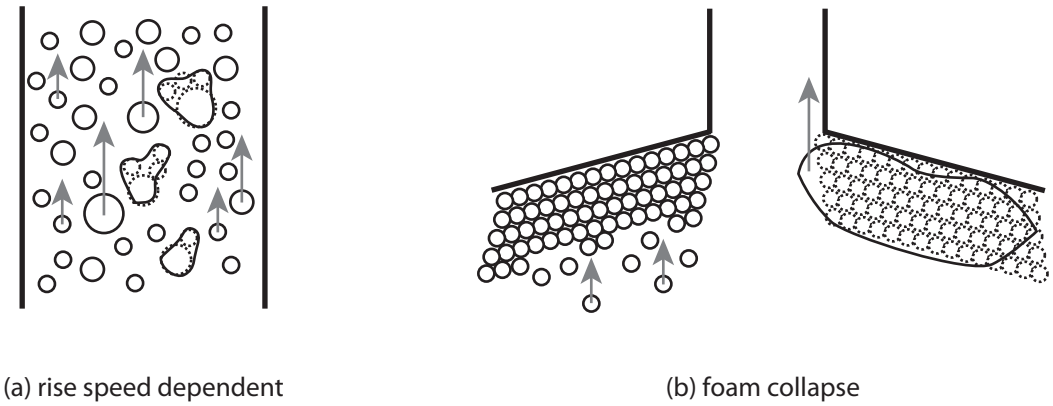

Figure 1.3: Schematic sketch illustrating the current models of slug formation. In the rise speed dependent model the differential rise speed of various-sized bubbles in the conduit leads to coalescence, and thus to the formation of larger bubbles which ultimately coalesce into a slug. In the foam collapse model small bubbles accumulate below a structural boundary in the conduit, e.g. below the top of an intercalated magmatic reservoir, until a critical bubble layer thickness is reached. The bubble layer then collapses into a slug.

periments (see figure 1.3). In the first model rise speed dependent bubble coalescence leads to the formation of larger bubbles which ultimately coalesce into a slug (*Wilson and Head*, 1981; *Parfitt and Wilson*, 1995); in the second model slugs originate from the accumulation and collapse of a foam layer at geometrical discontinuities within the plumbing system (*Jaupart and Vergniolle*, 1988, 1989). In both cases gas slugs rise at much faster rates than the melt to cause Strombolian explosions at the surface. In principle, both models are thus consistent with Strombolian behavior.

Yet neither of both models has been validated against direct observations in sensu stricto. An examination of both models with respect to eruption pattern has been carried out only for Hawaiian activity (*Parfitt and Wilson*, 1994; *Vergniolle and Jaupart*, 1990; *Vergniolle*, 1996; *Parfitt*, 2004). For Strombolian activity no such study exists so far due to the lack of a suitable base of observations.

Ongoing research at Stromboli volcano has left a puzzling set of observations. In fact, there is some controversy concerning the characteristics of Strombolian behavior. The relationship between explosive style and explosive degassing is poorly constrained and subject of contradictory observations (*Lautze and Houghton*, 2007; *Patrick et al.*, 2007). Furthermore, it is unclear whether explosive activity can be perceived as a stationary random phenomenon. Several authors have argued that explosive activity is random based on visual or seismic observations (*Settle and McGetchin*, 1980; *Bottiglieri et al.*, 2005; *De Martino et al.*, 2011a,b). This is however at odds with the presence of temporal correlations as well as with systematic variations in explosive degassing (*Jaquet and Carniel*, 2001; *Ripepe et al.*, 2002). In any case, it is questionable whether individual observations of selected instruments reliably capture the nature of explosive degassing.

To resolve this controversy an integrative approach is needed. For a more comprehensive understanding it is necessary to compare various observations at different volcanoes. In this thesis I therefore investigate the activity of Yasur volcano on Tanna island, Vanuatu, by means of a multi-parametric geophysical approach, and compare my findings to observations at Stromboli volcano. In this way I gather a consistent base of observations with which to test the models of slug formation.

1.2 Structure of the Thesis

This thesis is structured in four main chapters:

Chapter 2 covers a description of the volcanic history of Tanna island, and gives an overview of the formation and eruptive activity of Mt. Yasur. The measurement campaign at Mt. Yasur is explained, and the actual activity of the volcano is pictured in detail. The chapter ends with a first classification of Yasur's surface activity based on visual observations into ash-free and ash-rich explosions.

Chapter 3 deals with the geophysical fingerprint of the different explosion forms found at Mt. Yasur. Doppler radar, infrared camera and infrasound data are used to quantify surface activity in terms of material movement, temperature and excess

pressure. Through the combined analysis of these data it is shown that a given explosion form persists over days. The screening of all data further allows to capture the differences between ash-free and ash-rich explosion types. In general, ash-free explosions feature higher explosion velocities and excess pressures compared to their ash-rich counterparts. In terms of infrasonic waveforms the signal shape varies across explosive regimes. It remains however unclear whether this mirrors a definite change in explosion dynamics. Modeling of infrasound wave propagation under ash-free and ash-rich conditions demonstrates that time-dependent changes in the propagation medium may cause signal alteration. It is therefore impossible to draw an exclusive conclusion.

As a consequence I adopt a generic approach to examine the temporal variability of explosive degassing in **Chapter 4**. Different statistical measures are used to capture explosive gas release from Doppler radar, infrasound and seismic data. Explosive degassing is characterized in terms of explosion rate and intensity as well as in terms of return time. The investigation of these measures with regard to explosive style permits to establish a systematic link between explosive degassing and surface activity. The analysis of explosion magnitudes and return times equally demonstrates the power-law character of explosive gas release. Temporal changes in this character are shown to reflect changes in surface activity. A separate examination of the related temporal dynamics reveals that temporal fluctuations in degassing are correlated in time. In summary, the work at Yasur suggests that Strombolian activity is neither random nor stationary. Analog investigations of long term Doppler radar data recorded at Stromboli support this idea. Since this is at odds with the current models of activity, the chapter closes with the presentation of a new model for active degassing at Strombolian volcanoes.

Finally, **Chapter 5** draws the overall conclusions of the presented work, and provides some recommendations for possible future research.

Chapter 2

Data Set

This chapter provides some relevant background information on the data set used in this work. It includes a summary of the tectonic setting and eruptive history of Mt. Yasur as well as a comprehensive description of the current activity of the volcano. Practical aspects of the simultaneous collection of Doppler radar, infrared, infrasound and seismic data at Yasur are presented in detail. For a review of the different techniques the reader is referred to *Hort et al.* (2003); *Spampinato et al.* (2011); *Johnson et al.* (2004); *McNutt* (2005), respectively. Please note that parts of the information given in this chapter will be reused in subsequent chapters as each chapter has been written in a self-contained manner, and is independent of the others.

2.1 Yasur Volcano, Vanuatu

Mt. Yasur is one of the most active volcanoes of the Vanuatu island archipelago (*Bani et al.*, 2012). It is located on the island of Tanna in the southern segment of the Vanuatu volcanic arc (see figure 2.1 a). This arc defines the convergent margin between the Australian plate and the spreading North Fiji basin (*Auzende et al.*, 1995; *Calmant et al.*, 2003). The rate of plate convergence reaches almost 12 cm/yr near Tanna (*Monzier et al.*, 1984; *Taylor et al.*, 1995). According to *Louat et al.* (1988) the island lies approximately 150 km east of the Vanuatu trench and 150 km above the Benioff zone. It covers 550 km^2 and developed through successive phases of volcanic activity and reef limestone growth.

Tanna's volcanic history can be divided into three major episodes (*Carnay and MacFarlane*, 1979). The first two episodes in late Pliocene and Pleistocene generated the

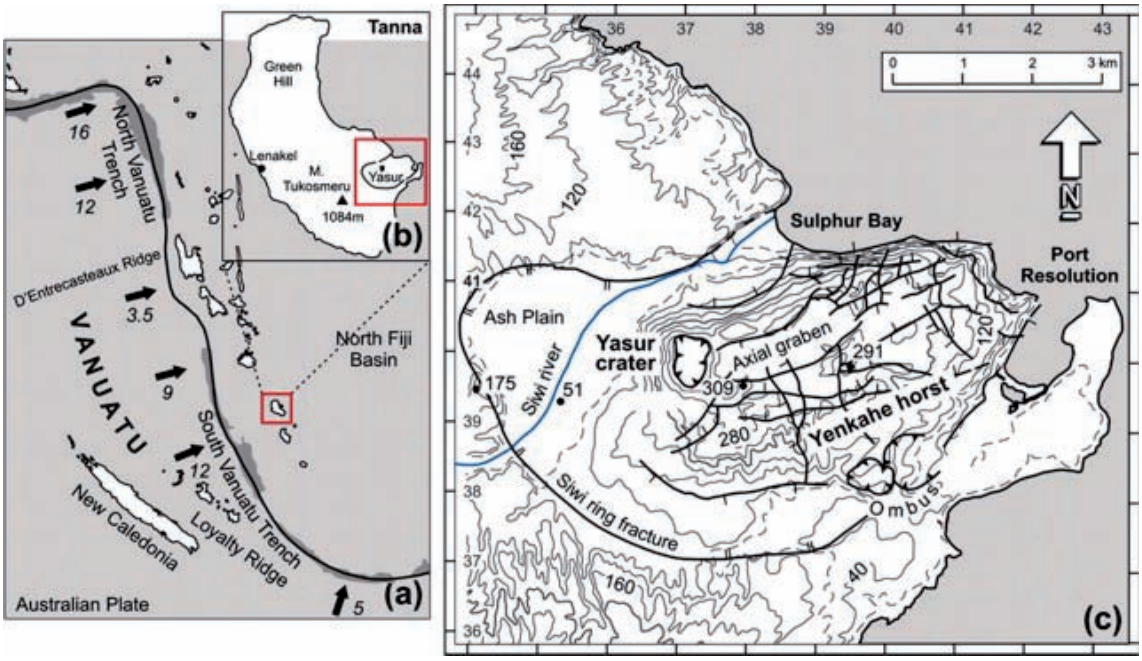

Figure 2.1: (a) Map showing the Vanuatu arc in the SW Pacific, the position of the 6-7 km deep Vanuatu trench, convergence rates (indicated by arrows in cm/yr), and the location of Tanna island (redrawn from *Pelletier et al.* (1998) and *Calmant et al.* (2003)). (b) Schematic map of Tanna island with the locations of the main volcanic centers (redrawn from *Carnay and MacFarlane* (1979)) (c) Map of south-eastern Tanna showing the Yasur cone and Yenkahe horst, bounded by the Siwi ring fracture (redrawn from *Nairn et al.* (1988) and *Allen* (2005)). After *Métrich et al.* (2011).

Green Hill and Tukosmeru volcanics in the north and south of the island (see figure 2.1 b). A complex pyroclastic series indicates a caldera-forming event during this period (*Robin et al.*, 1994). The third episode known as Yenkahe phase started in late Pleistocene. Volcanic activity began to concentrate in the south-eastern part of Tanna and an eruption of moderate volume (∼1-2 km^3) produced the Siwi ignimbrite of basalt-andesitic to andesitic composition (*Carnay and MacFarlane*, 1979; *Nairn et al.*, 1988; *Robin et al.*, 1994; *Allen*, 2005). This triggered a caldera-type collapse along the Siwi ring fracture (see figure 2.1 c) followed by a new cycle of volcanic unrest. Rapid uplift of the caldera floor caused resurgence of the Yenkahe horst and volcanic activity renewed creating the now inactive Ombus volcanic center (*Carnay and MacFarlane*, 1979; *Nairn et al.*, 1988; *Robin et al.*, 1994). Comparing the horst's uplift of more than 150 mm/yr (*Chen et al.*, 1995) to the regional uplift since the late Quaternary (∼1.6 mm/y, see *Neef et al.*, 2003) the volcanic origin of uplift becomes clear. Historical records of local uplift of the Yenkahe area (e.g. 10-15 m in 1878, see *Chen et al.*, 1995) furthermore argue for horst resurgence due to magma emplacement. This is in line with the results of *Métrich et al.* (2011).

Investigating early as well as current magma and volatile supply at Yasur, these authors conclude that gradual storage of unerupted degassed magma could easily account for the observed resurgence.

Recent eruptive activity in the Siwi caldera is restricted to the presently active Yasur cinder cone (*Simkin and Siebert*, 1994). Since about 1400 years eruptive activity has focused at this volcano on the western edge of the Yenkahe horst (*Métrich et al.*, 2011). The actual growth of the cone probably began about 800 years ago and is still ongoing (*Nairn et al.*, 1988). The volcano has been considered to be continuously active, since its first sighting by Captain Cook in 1774, with periods of high activity in 1974, 1975, 1977, and since 1994 (*Simkin and Siebert*, 1994). However, long term measurements of SO_2 emission rates during the current period suggest strong variations in activity level (*Bani and Lardy*, 2007).
Today Mt. Yasur rises 379 m above sea level and has a nearly circular 400-m-wide summit crater. This crater contains three active vents as shown in figure 2.2. Normal activity consists of sustained degassing along with explosions of Strombolian to mild-Vulcanian vigor. Explosions occur with an average frequency of 1-3 per minute erupting magma of basalt-trachyandesitic composition (*Oppenheimer et al.*, 2006; *Métrich et al.*, 2011). Seismic signatures caused by explosions are similar to those

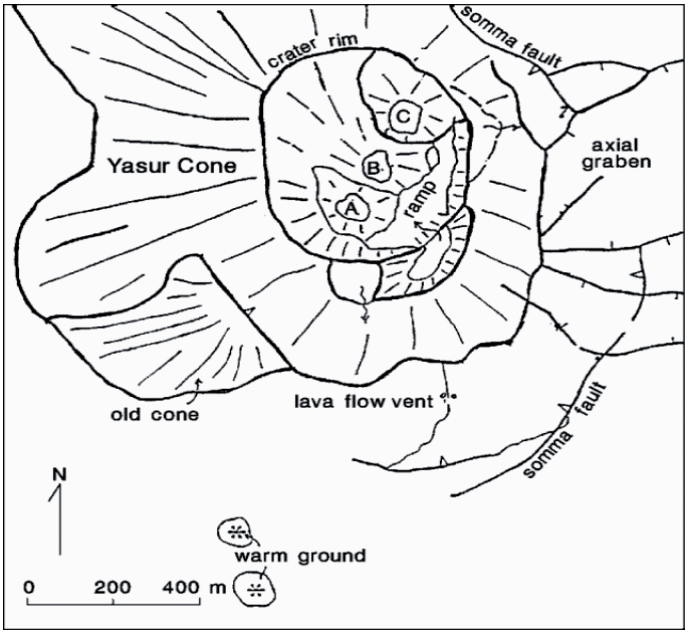

Figure 2.2: Schematic map of the Yasur crater area (after *Nairn et al.* (1988)). The letters A, B and C denote the three active vents in the 400-m-wide summit crater.

found at Stromboli volcano indicating a similar causative mechanism (*Nabyl et al.*, 1997). This is corroborated by a recent investigation of volcanic gases released by explosions (*Oppenheimer et al.*, 2006). Their different composition compared to passive gas emissions implies that deep volatile exsolution drives explosive activity. Like at Stromboli, the exsolved gas is thought to rise in form of gas slugs causing explosions at the surface. Detailed analysis of the seismic signals associated with this process suggests that a single feeder system is maintaining Yasur's activity (*Kremers et al.*, 2013). Petrological characterization of eruptive products from vents A and C supports this idea (*Kremers et al.*, 2012). The chemical similarity of these products points to a homogeneous magma supply through a common feeder system at depth.

2.2 Experiment Setup

Our measurement at Yasur took place between August and September 2008. It was mainly designed to map conduit and near-surface processes, such as the development and rise of gas slugs up to their final explosion. The accomplished experiment setup is shown in figure 2.3. It consisted in five main monitoring clusters, i.e. one at the crater rim and four on the ash plane around the volcano.

The cluster at the crater rim incorporated a large part of instruments to monitor Yasur's surface activity. Since vent A was clearly most active, we installed one Doppler radar and one infrared camera to record its degassing behavior. In addition, we deployed a second Doppler radar to observe vent C. Likewise we set up two infrasound sensor arrays to track the pressure signals associated with activity as well as one short period seismometer recording high frequency transients related to explosions. Within the realm of possibilities this layout was the most appropriate for a later quantification of the surface activity dynamics.
The second monitoring cluster, involving one broadband infrasound sensor along with three short period and one broadband seismic station, was located partly on the flanks of the volcano in the south-east. The location of the broadband acoustic sensor was chosen to ensure the recording of the low frequency signature of the pressure waves generated by explosions.
The remaining three clusters north-west of the volcano were composed of a broadband seismometer and two or three short period seismic stations. Additionally, we co-located two infrasound arrays with the broadband seismometers of the two larger clusters. This was necessary for measuring the effect of air coupled seismic waves on our broadband seismic recordings. Furthermore, it facilitates the correlation of acoustic, seismic and Doppler radar signals, because the exact start time of the acoustic signal at the source can be determined. The general setup of the seismic

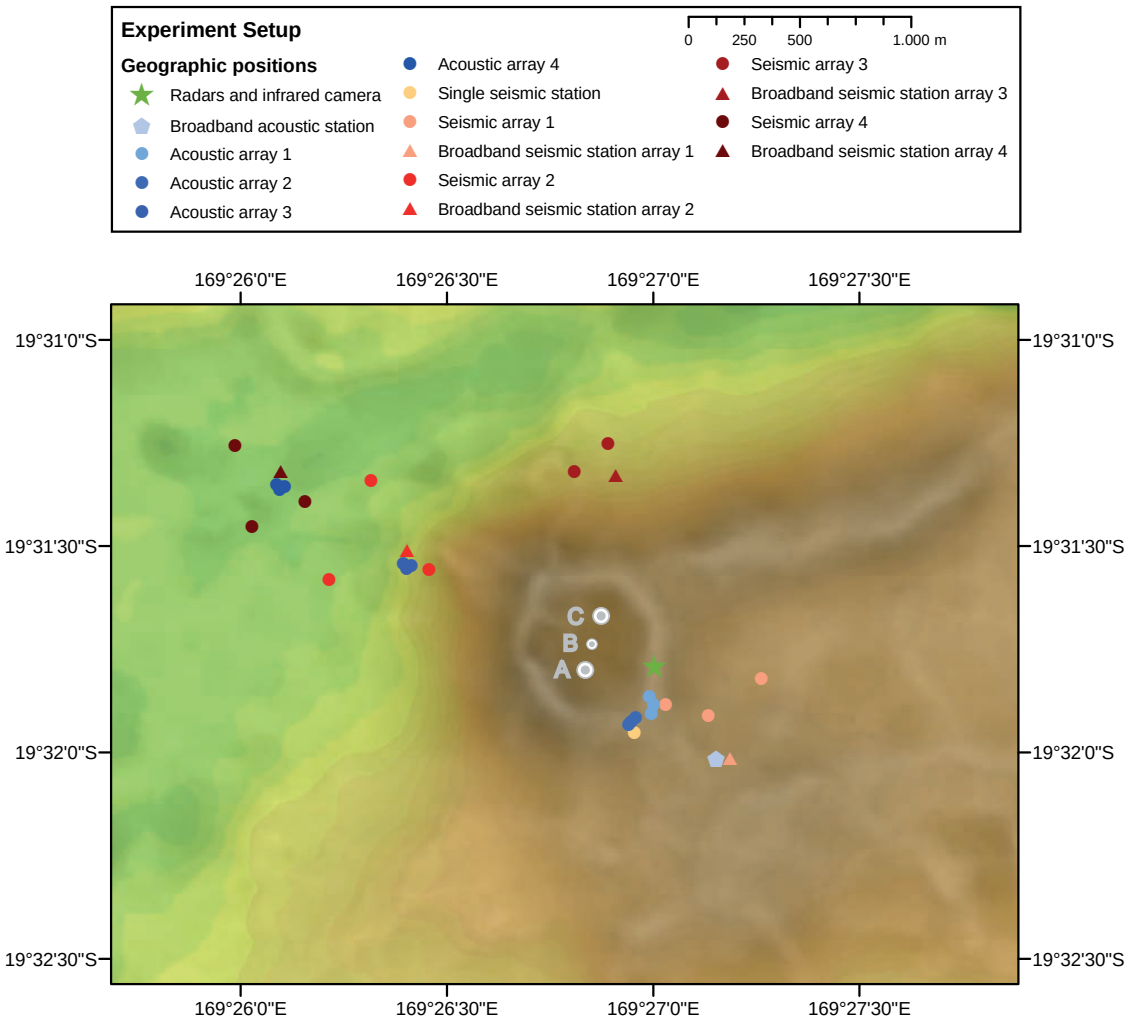

Figure 2.3: Experiment setup at Yasur volcano. The location of the different instruments is shown on top of a digital elevation model. The relief of the area is color-coded from green to brown corresponding to low and high elevation, respectively.

stations was considered most suitable for monitoring the occurrence of LP signals before explosions, but also for the use of array and network techniques during data processing.

At the time of our experiment the activity of Yasur was at a relatively high level with several explosions per minute. This is consistent with SO_2 emission rates recorded during nine days of our measurement. SO_2 emissions were monitored by a mini-DOAS beside a Doppler radar tracking plume speed. Analysis of these data yields

SO_2 discharge rates ranging between 640 t/d and 1100 t/d (*Wagner*, 2011). This is on the high end reported at Yasur (*Bani and Lardy*, 2007), and demonstrates the elevated activity of the volcano.
Despite the elevated level of activity, the surface activity was normal during the 15 days of our experiment. Direct visual observations of vent A showed permanent degassing and recurrent Strombolian explosions. These were characterized by either a clear bursting of lava bubbles or a more jet-like explosion pattern. Daily observations further revealed a prominent transition in explosive style from mostly ash-free explosions dominated by ballistic clasts to explosions showing a very large ash load or even only consisting in ash emissions. The aim of the following chapters is to unravel this behavior. For this purpose I first investigate Doppler radar, infrared and infrasound recordings of ash-free and ash-rich explosions, and discuss my findings in the context of previous observations made at Stromboli.

Chapter 3

Surface Activity Regimes

In the first part of this chapter I study the geophysical fingerprint of Yasur's different explosive styles. The observed explosion forms are characterized by means of Doppler radar, infrared camera and infrasound data. The combination of these data reveals significant differences between ash-free and ash-rich explosion types. While high explosion velocities and temperatures relate to ash-free activity, ash-rich explosions feature low velocities and temperatures. Furthermore, ash-free explosions generate high excess pressure signals exhibiting high frequencies opposed to low-amplitude, low-frequency signals accompanying ash-rich activity. In general, variations in explosion intensity correlate with changes in explosive style and point to a different explosion dynamics. To further assess the latter it would be common to compare infrasonic waveforms. In the second part of this chapter I however demonstrate that an explicit comparison of waveforms is challenging in the presence of different near-source conditions. Modeling of infrasound propagation under ash-free and ash-rich conditions highlights that a proper knowledge of the local atmospheric properties at the vent is essential as time-dependent changes in the propagation medium may cause signal alteration.

3.1 Strombolian Surface Activity Regimes at Yasur volcano, Vanuatu, as observed by Doppler Radar, Infrared Camera and Infrasound

3.1.1 Abstract

In late 2008 we recorded a continuous multi-parameter data set including Doppler radar, infrared and infrasound data at Yasur volcano, Vanuatu. Our recordings cover

a transition in explosive style from ash-rich to ash-free explosions followed by a phase of high ash discharge. To asses the present paradigm of Strombolian behavior in this study we investigate the geophysical signature of these different explosive episodes and compare our results to observations at Stromboli volcano, Italy. To this end we characterize Yasur's surface activity in terms of material movement, temperature and excess pressure. The joint temporal trend in these data reveals smooth variations of surface activity and regime-like persistence of individual explosion forms over days. Analysis of all data types shows ash-free and ash-rich explosive styles similar to those found at Stromboli volcano. During ash-free activity low echo powers, high explosion velocities and high temperatures result from the movement of isolated hot ballistic clasts. In contrast, ash-rich episodes exhibit high echo powers, low explosion velocities and low temperatures linked to the presence of cold ash-rich plumes. Furthermore, ash-free explosions cause high excess pressure signals exhibiting high frequencies opposed to low-amplitude, low-frequency signals accompanying ash-rich activity. To corroborate these findings we compare fifteen representative explosions of each explosive episode. Explosion onset velocities derived from Doppler radar and infrared camera data are in excellent agreement and consistent with overall observations in each regime. Examination of infrasound recordings likewise confirms observations, although a weak coupling between explosion velocity and excess pressure indicates changes in wave propagation. The overall trend in explosion velocity and excess pressure however demonstrates a general correlation between explosive style and explosion intensity, and points to stability of the uppermost conduit on time scales shorter than at Stromboli volcano.

3.1.2 Introduction

In general Strombolian volcanoes show a variety of eruptive styles. These include episodes of lava effusion, highly energetic paroxysmal explosions and normal surface activity. Normal activity is characterized by permanent non-explosive degassing interrupted by mild explosions, which can be divided in two different types depending on the grain size of the ejecta (e.g. *Chouet et al.*, 1999; *Ripepe and Marchetti*, 2002). According to *Patrick et al.* (2007) Type 1 explosions are dominated by coarse ballistic clasts, while Type 2 explosions consist of an ash-rich plume, with (Type 2a) or without (Type 2b) large numbers of ballistic particles. At Stromboli volcano, Italy, both explosive styles can occur at a given vent, however various studies indicate a common relation between explosion type and vent location (*Ripepe and Marchetti*, 2002; *Chouet et al.*, 2003; *McGreger and Lees*, 2004; *Marchetti and Ripepe*, 2005; *Scharff et al.*, 2008). A particular gross explosive style normally persists for days to weeks at a certain location suggesting stability of the uppermost conduit on these timescales (*Patrick et al.*, 2007).

Several years of research have helped to link the individual explosive forms to variations in texture and composition of volcanic products (*Lautze and Houghton*, 2005, 2007; *D'Oriano et al.*, 2010), but also to contrasting geophysical signatures (*Harris and Ripepe*, 2007a, for review). As a result characteristic waveforms in seismic (e.g. *Marchetti and Ripepe*, 2005), infrasound (e.g. *McGreger and Lees*, 2004) and infrared signals (e.g. *Harris and Ripepe*, 2007a) as well as differences in explosion velocities (e.g. *Patrick et al.*, 2007), pressures (e.g. *Ripepe and Marchetti*, 2002) and thermal amplitudes (e.g. *Ripepe et al.*, 2005a) may be attributed to ash-free and ash-rich explosions. Yet all these findings mainly hold for Stromboli volcano, Italy, which is most researched regarding its activity.

To put these results in a wider context, and to broaden our knowledge about Strombolian explosions, it is important to compare observations at different volcanoes. To this end we collected a multi-parameter data set at Yasur volcano, Vanuatu, in late 2008. Despite its very regular activity this volcano is barely studied, and offers hence ideal conditions to assess our present understanding of Strombolian activity. During 15 days we recorded a continuous data set including Doppler radar, infrared, infrasound and seismic data. A total of about 58000 Strombolian explosions were observed covering a transition in explosive style from ash-rich to ash-free explosions followed by a phase of high ash discharge. In this study we focus on the observations made by Doppler radar, infrared camera and infrasound. Seismic recordings have been discussed in (*Kremers et al.*, 2013).
In order to explore Yasur's different explosive styles we characterize surface activity in terms of material movement, temperature and excess pressure related to explosions. Based on these data we then analyze the geophysical signature of ash-free and ash-rich activity and compare characteristic features of each explosive episode. To elaborate our findings we investigate fifteen ash-free and ash-rich explosions in detail. In particular, we compare explosion onset velocities derived from Doppler radar and infrared camera data as well as infrasonic waveforms. Our results expose significant differences between ash-free and ash-rich activity and reveal a general correlation between explosion intensity and explosive style. Moreover, the temporal trend in our data demonstrates the persistence of a given explosive style through time. Our results at Yasur are overall in line with observations at Stromboli and strengthen previous findings from quasi-continuous measurements which suggested stability of the uppermost conduit to a certain extent. The continuity of our data set likewise provides a complete picture of explosion style transitions which bears important implications for the origin of explosive styles.

3.1.3 Background

Mt. Yasur belongs to the most active volcanoes of the Vanuatu island archipelago (*Bani et al.*, 2012). It is located in the south-eastern part of Tanna island, which developed through successive phases of volcanic activity and reef limestone growth (*Bani and Lardy*, 2007). Tanna's volcanic history can be traced back to late Pliocene from a series of major volcanic episodes (*Carnay and MacFarlane*, 1979). The most recent episode known as Yenkahe phase produced the Siwi ignimbrite of basalt-andesitic to andesitic composition (*Nairn et al.*, 1988; *Robin et al.*, 1994; *Allen*, 2005) involving the formation of the Siwi caldera.
Recent volcanic activity in the Siwi caldera is restricted to the 379 m high Yasur cinder cone and consists of sustained degassing along with explosions of Strombolian to mild-Vulcanian vigor (*Simkin and Siebert*, 1994). Volcanic gases are continuously released from three active vents named A, B and C, hosted within a nearly circular 400-m-wide summit crater (*Nairn et al.*, 1988; *Oppenheimer et al.*, 2006) erupting magma of basalt-trachyandesitic composition (*Métrich et al.*, 2011). Seismic signatures caused by explosions are similar to those found at Stromboli volcano pointing to a similar causative mechanism (*Nabyl et al.*, 1997). This is confirmed by a recent analysis of volcanic gases released by explosions (*Oppenheimer et al.*, 2006). Their different composition compared to passive gas emissions implies that deep volatile exsolution drives explosive activity. Like at Stromboli, the exsolved gas is thought to rise in form of gas slugs causing explosions at the surface. Detailed analysis of the seismic signals associated with this process suggests that a single feeder system is maintaining Yasur's activity (*Kremers et al.*, 2013). Petrological characterization of eruptive products from vents A and C further supports this idea (*Kremers et al.*, 2012). The chemical similarity of these products points to a homogeneous magma supply through a common feeder system at depth.

At the time of our experiment, in August/September 2008, the activity of Yasur was at a high level with sometimes several explosions per minute. Vent A was clearly most active, and during the first two days of our measurement the surface of the magma column was visible before it retreated in the conduit. Direct observations of the vent exit showed permanent degassing and recurrent Strombolian explosions characterized by either a clear bursting of gas bubbles or a more jet-like explosion pattern. Daily visual monitoring revealed a prominent transition in explosive style from ash-rich jetting over ash-free explosions dominated by ballistic clasts to explosions showing a very large ash load or even only consisting in ash emissions. This was followed by a transitional phase during which activity evolved back towards nearly ash-free explosions.

3.1.4 Doppler Radar Data

To monitor material movement at Yasur, we used a 24 GHz frequency modulated continuous wave Doppler radar (e.g. *Hort et al.*, 2003). This type of radar transmits an electromagnetic wave, and records the amplitude and Doppler shift of the signal that is backscattered by moving objects, i.e. by volcanic ash, lapilli and bombs. In this context the amplitude of the signal gives information about the amount of moving material, while the frequency shift is directly proportional to the objects' velocities along the radar beam. Thus by measuring the amplitudes of all frequency shifts a Doppler spectrum is recovered that reflects the movement of material as a function of velocity.

To record material movement at vent A, we installed a high-resolution radar instrument on the crater rim, 276 m away from the vent exit tilted 27.5° downwards yielding a field of view (FOV) equal to the size of the conduit of about 15 m. Doppler spectra were continuously registered at a frequency of 25 Hz with a velocity resolution of 0.79 m/s. The maximum unambiguous velocity along the radar beam was ± 202 m/s.
During our 15 days measurement campaign the high-resolution instrument was replaced by an older instrument with lower resolution on days ten to twelve. This restricted the maximum unambiguous velocity to be ± 50 m/s during this period. Furthermore, the sensitivity of the older instrument was slightly different. The amplitudes of the radar signals are therefore not comparable. On day 13 the high-resolution instrument was reinstalled, but due to small differences in the alignment of the radar beam a quantitative comparison between the first and the final measurement period should also be done with due care. Nonetheless, considering the general measurement set up, and assuming that ejecta are mainly erupted vertically, positive velocities can be attributed to rising particles, while negative velocities relate to falling ones. In the following we will concentrate on rising particles and refer to their velocities along the radar beam as velocities. Otherwise we will explicitly give direction (e.g. vertical velocity).

To guarantee a proper processing of the data a cross-validation data set of each explosive style was hand-picked and later compared to results from automatic processing via our recently developed software package (*Vöge and Hort*, 2009). An important first step was to find the correct settings for automatic event detection. For this purpose detection parameters were either based on information about the amount of material moving inside the FOV or on its velocities, i.e. either the amplitudes or the frequencies of the radar spectra were considered. The obtained results were then validated using the above mentioned hand-picked data. Event detection based on velocity criteria proved to be better as the amplitudes of the radar signals

showed strong variations due to the differential ash load of explosions. An explosion was declared once the velocity exceeded 10 m/s until returning to values smaller than 5 m/s. Using these settings we performed a simple threshold search to create an event catalog of the entire dataset. Based on this event catalog the so-called echo power of each explosion was determined in order to obtain a first order proxy for the total amount of moving material in the FOV. To characterize activity in terms of explosion intensity we further extracted the maximum velocity of each explosion (for details, see *Scharff et al.*, 2012).

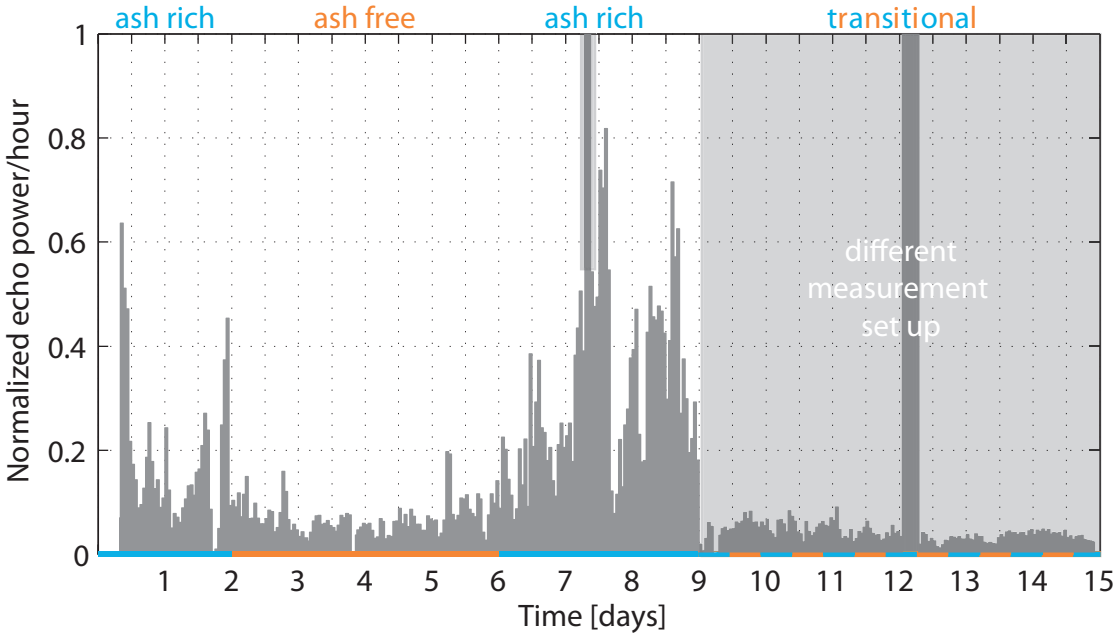

Figure 3.1: Normalized echo power per hour as recorded by Doppler radar. The origin of the x-axis is 23.08.2008 and annotations on the x-axis mark the end of each day. On average intermediate echo power values characterize the first two days of our measurement, whereas low echo powers are present from start of day three to end of day six. This is followed by a remarkable increase in echo power, and high values persist for at least three days. Changes in measurement configuration after day nine inhibited a comparable further recording of echo power. The different explosive styles observed in the field are marked by blue and orange annotations on top of the figure. Bars at the bottom of the figure indicate their duration.

The resulting data are presented in figure 3.1 and figure 3.2. For a better overview the echo power was summed up on an hourly basis. Since the echo power per hour is only a relative proxy for the material moving inside the FOV, it is normalized to the maximum value recorded during our experiment. One interesting observation when looking at both time series is the simultaneous change of the overall trend in echo

power and maximum velocity, especially after day two and day six. Before the end of day two the echo power oscillates around intermediate values, and velocities smaller than 60 m/s characterize activity. From start of day three to end of day six low echo powers prevail, and velocities of up to at least 202 m/s are present. After this period a remarkable increase in echo power as well as a decrease in velocity follows. High echo power values persist for at least three days. However, due to the above mentioned replacement of the Doppler radar, echo power values from days ten to twelve are not comparable. The same is valid for the echo power recorded during the last days of our measurement for reasons of alignment. Concerning the presented velocities, the values of around 50 m/s reported on day ten, eleven and twelve result from saturation of the old instrument. So the maximum velocity of explosions amounted to at least 50 m/s during this period. Absolute velocities recorded in the subsequent time interval must also be treated with caution owing to the slight differences in radar beam alignment. Yet the temporal trend in velocity on day thirteen and fourteen may still be interpreted as a transition back to higher velocities.

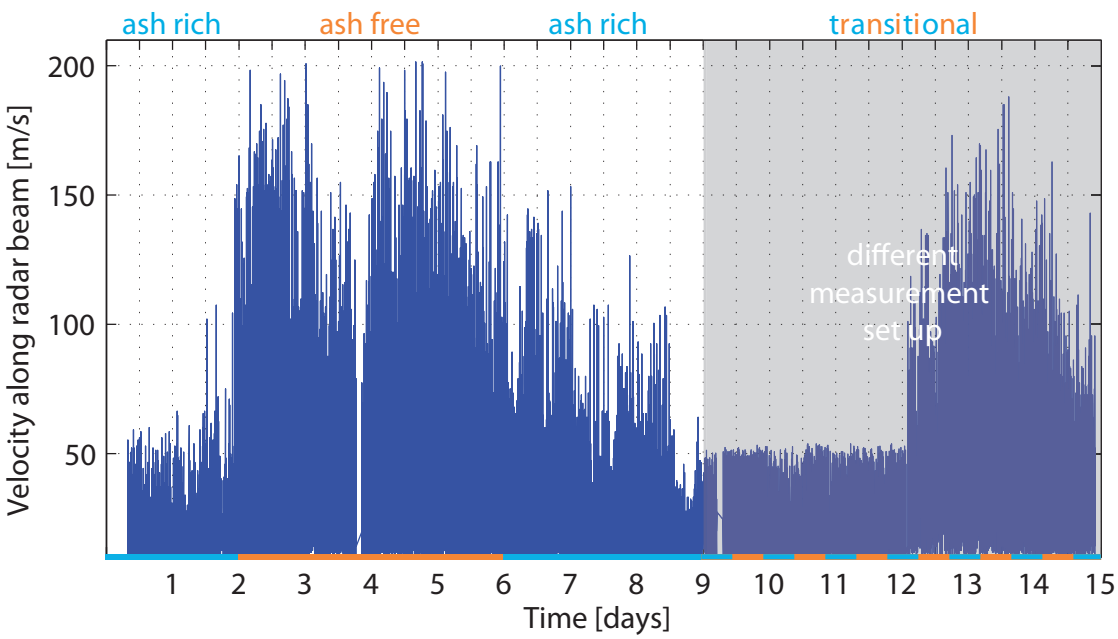

Figure 3.2: Maximum velocity of explosions as recorded by Doppler radar. Annotations on the x-axis equal those in figure 3.1. During the first two days of our measurement activity features low velocities, whereas from start of day three to end of day six high velocities prevail. A notable decrease in velocity follows over at least three days, i.e. over days seven to nine. Subsequent changes in measurement configuration prevented a comparable further recording of velocity. Absolute values of velocity are therefore incomparable during the final measurement period. Yet the temporal trend in velocity on day thirteen, fourteen and fifteen still mirrors a transition back to higher velocities. The observed explosive styles are again tagged by blue and orange annotations.

3.1.5 Infrared Camera Data

Thermal videos of activity at vent A were acquired using a TVS-700 infrared camera produced by NEC-Avio. This camera is equipped with a 320 × 240 uncooled microbolometer focal plane array with a field of view of 26° × 19.6°, a geometrical resolution of 1.4 mrad and a spectral response from 8 to 14 μm. It operates in a temperature range between -20 °C and 500 °C at 25 frames per second. Images are stored in a circular memory buffer at a 12 bit quantization producing an image file size of ∼120 kB.
To reduce the amount of data we recorded activity in a trigger based mode. For this purpose we defined critical temperature values from preliminary footage of explosions. Once these values were exceeded final data storage was triggered, and the content of the circular memory buffer including the onset of each explosion was read out. In order to compare the so-obtained data to Doppler radar data, we set up the camera at the same distance to the vent as the radar with an inclination of 18.9°. At this distance each pixel in the thermal image is about 0.4 m^2 in size, and the field of view covers an area of 127.95 m × 95.35 m.

To get qualitative insights into Yasur's surface activity we analyzed the recorded thermal video sequences using GORATEC Thermography studio®. Due to the amount of data ($\sim 2 \times 10^6$ frames) we analyzed one arbitrary explosion per hour. To discover potential trends in activity the presence or absence of an optically-thick ash plume were used as discriminating characteristics for explosive style. According to this rough classification the temporal trend in activity is overall in line with visual observations from the field. Figure 3.3 shows two representative frame sequences of ash-free and ash-rich explosions recorded at day five and day eight, respectively. Here, the presented temperature values do not correspond to true ejecta temperatures as the recorded thermal signals result from the contribution of gas, ash and ejecta plus any ambient background in each pixel. Still when considering the vent area there are clear differences between both explosions. During ash-free activity the vent exit is visible and high temperatures dominate the area, while ash-rich activity features colder temperatures around the vent. It is thus possible to characterize activity via temperature, although the recorded values are only a proxy for true ejecta temperature. To discriminate between explosions in a quantitative manner we took advantage of this effect. To this end we defined a small area of analysis around the vent (37 m × 27 m) and calculated the average temperature in this area for each frame at a fixed emissivity of 0.96. Based on the frame sequence of each explosion the highest temperature was then picked to determine the maximum average temperature of each explosion.

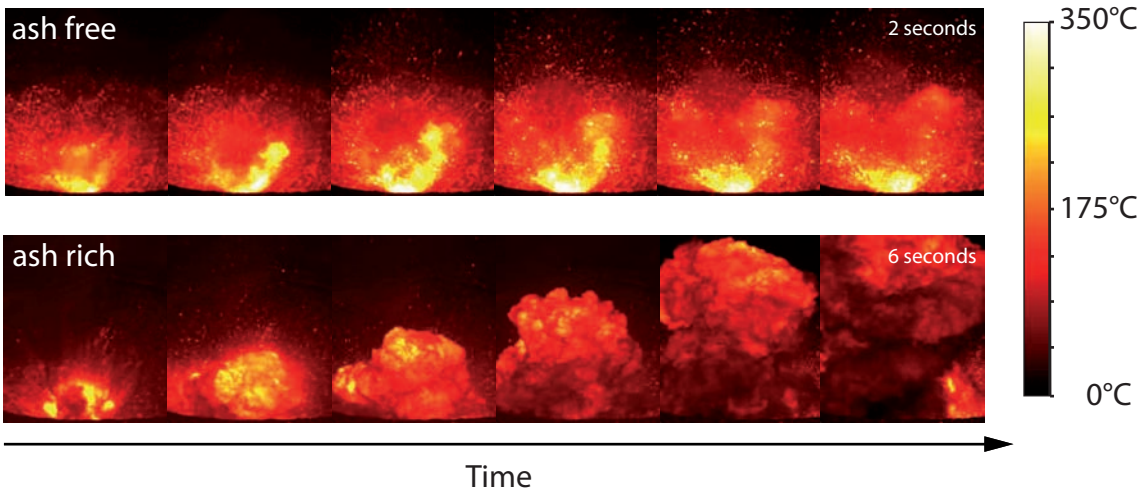

Figure 3.3: Representative infrared camera recordings of ash-free and ash-rich explosions. Two frame sequences of different length are shown. During ash-free explosions the vent exit is permanently visible and high temperatures prevail, whereas ash-rich explosions are dominated by a cold opaque eruptive cloud. To demonstrate its development a frame sequence of six seconds length is presented. As ash-free explosions are related to high velocity ejecta, the sequence of the ash-free regime covers only two seconds.

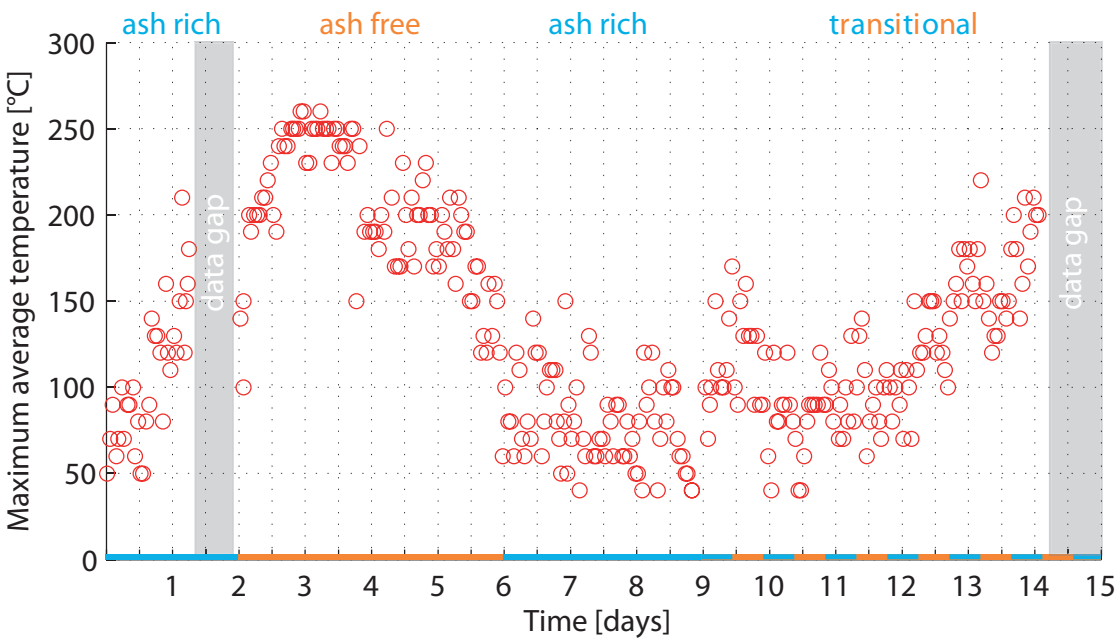

Figure 3.4: Maximum average temperature of explosions as recorded by infrared camera. Annotations on the x-axis again equal those in figure 3.1. Data gaps owing to technical problems are marked in gray. The first one and a half days of our measurement show an increase in temperature from low to intermediate values. A further increase in temperature follows and highest temperatures were measured at day three and four. After these days temperature decreases again, and from day six on low temperatures prevail. Temperatures remain relatively low showing some oscillations until a new increase in temperature starts between day thirteen and fourteen. The different explosive styles are again denoted by blue and orange annotations.

Figure 3.4 displays the resulting maximum average temperature of each studied explosion. The first one and a half days of our measurement indicate an increase in explosion temperature from low to intermediate values. This is followed by a further increase in temperature and high temperature values are present at day three and four. After these days the temperature decreases again, and from day six on low temperatures characterize activity. Temperatures remain relatively low showing some oscillations until the temperature increases again between day thirteen and fourteen.

3.1.6 Infrasound Data

To track pressure signals related to activity we installed four narrow-band infrasonic arrays and one broadband infrasound station at Yasur. The arrays were located close to the radar at a distance of 270 m and 280 m from vent A, and 920 m and 1560 m north-west of the volcano. The broadband station was deployed about 640 m away from vent A in the south-east. All arrays were composed of SensorTechnics 144SM350D-PCB microphones with a differential pressure range from 0 to 350 hPa, and a flat frequency response from 0.05 to 5 Hz. The broadband sensor was a MB2005 microbarometer produced by Martec with a peak to peak pressure range of $\pm$ 100 hPa, and a flat spectral response from 0.03 to 10 Hz. Data were collected at 100 Hz via six-channel PR6-24 Earth Data Loggers as well as by a six-channel Reftek 130. To reduce wind noise in our recordings we equipped each instrument with 10 m long hoses of variable porosity. Time synchronization of all instruments was obtained using GPS receivers.

After bandpass filtering all data from 0.1 to 20 Hz we followed two different approaches to detect explosive events at vent A. In the first approach we used theoretical travel times to the vent to delay all infrasound traces. In a subsequent step, traces from all short period sensors were summed and compared to the trace of the broadband station based on their coherence. An event was detected once the coherence and pressure exceeded 0.85 and 0.1 Pa, respectively, and the event time at the broadband sensor was registered. Based on this time the true event onset at the broadband station was then picked by selecting the maximum pressure and its corresponding time on the raw acoustic records.
The second approach consisted in a simple STA/LTA detection on the delayed-and-summed trace of all infrasound stations. To warrant the detection of small events we chose a STA-window of 3 s length, a LTA-window of 9 s length and a critical threshold of 0.45. Once an event was detected, we determined the onset time and maximum pressure measured at the crater rim, i.e. 270 m away from vent A, using the same picking procedure as in the first approach.

To analyze the frequency content of the associated signals we calculated the power spectral density of the pressure trace recorded at the broadband station. To account for non-stationary variations in power we applied a continuous wavelet transform using a Morlet wavelet with a non-dimensional frequency of 6 following the procedure described in *Torrence and Compo* (1998). For an efficient calculation the data were split into 24-hour segments. For a better overview the power spectral density was stacked in one minute intervals.

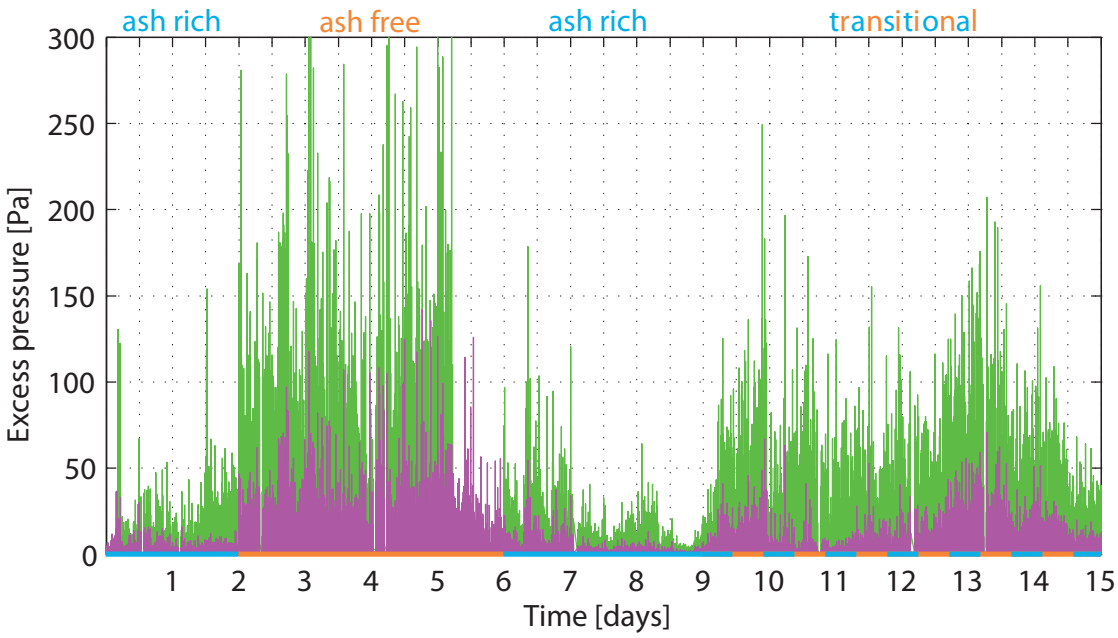

Figure 3.5: Excess pressure of explosions as recorded by infrasound. Annotations on the x-axis again equal those in figure 3.1. Pressures recorded at the crater rim and on the flanks of the volcano are shown in green and magenta, respectively. Despite the difference in absolute values both data sets illustrate the same temporal trend. Low pressure explosions dominate the first two days of our measurement, while activity between the start of day three and the end of day six features high excess pressures. After this time the pressure decreases again, and low pressure explosions characterize activity of day eight and nine. During the subsequent days intermediate excess pressures can be observed exhibiting some oscillations. The different explosive styles are again marked by blue and orange annotations.

The excess pressures of the detected explosions are presented in figure 3.5. Pressures recorded at the crater rim are shown in green, and exhibit overall larger values when compared to pressures measured at the broadband station given in magenta. Nevertheless, both data sets illustrate the same temporal trend. During the first two days of our measurement low excess pressures characterize activity, whereas high

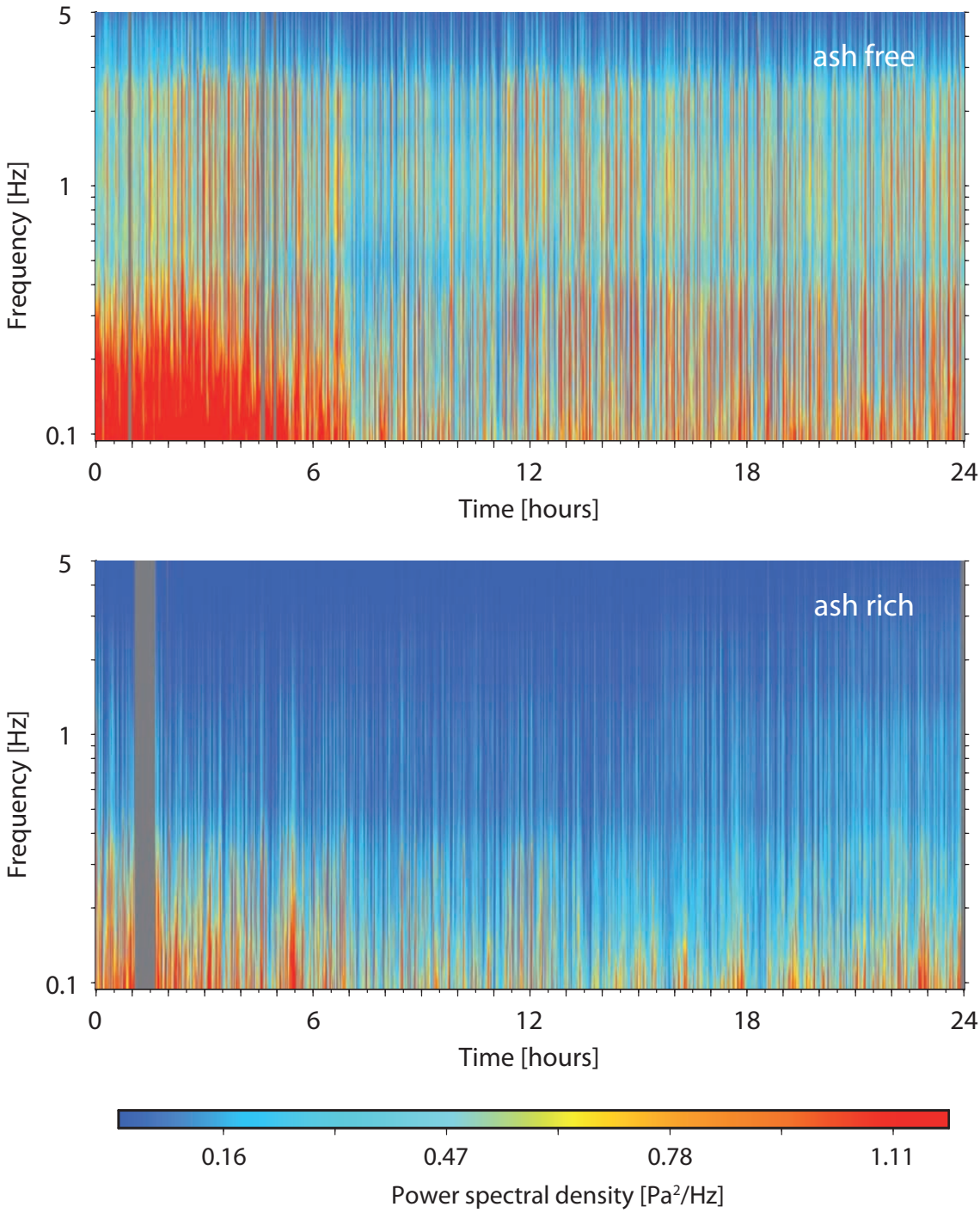

Figure 3.6: Power spectral density as recorded by infrasound on days five and eight. Data were stacked in one minute sections. High powers and high frequencies are present on day five, whereas day eight is characterized by low-power low-frequency signals. The observed explosive styles are denoted by white annotations.

excess pressures dominate days three to six. After this time the pressure decreases again, and day eight and nine feature low pressure explosions. On day ten the pressure increases to intermediate values, which show some oscillations during the final period of our measurement.
The analysis of the power spectral density is overall consistent with these observations. Periods of low and high excess pressures exhibit low and high spectral powers, respectively. Yet there are significant differences in the distribution of power with frequency. During low pressure phases the power concentrates at low frequencies, while high frequencies augment the power distribution in the presence of high excess pressures. To illustrate this behavior we present the power spectral density on days five and eight in figure 3.6. Powers at frequencies of up to 3 Hz can be observed on day five, while the power concentrates between 0.1 - 0.5 Hz on day eight.

3.1.7 Comparison of Regime Characteristics

The comparison between field observations and observations by Doppler radar, infrared camera and infrasound in figures 3.1 to 3.6 shows the contrasting geophysical signature of Yasur's different explosive styles. The joint temporal trend in all data reveals smooth variations of surface activity, and the regime-like persistence of a given explosive style over days. In terms of Doppler radar data the ash-free regime is characterized by high explosion velocities and low echo powers as opposed to low explosion velocities and high echo powers defining the ash-rich regime. Regarding infrared camera recordings high temperatures around the vent are associated with ash-free explosions incorporating hot ballistic clasts, while low temperature values result from the presence of cold ash-rich plumes. Infrasound observations feature wide-band high-pressure signals in the ash-free regime, whereas low-amplitude low-frequency signals accompany ash-rich activity.

To support these overall findings we investigated fifteen explosions of each explosive episode. In particular, we compared their explosion onset velocities derived from Doppler radar and infrared camera data as well as their infrasonic waveforms. The selected explosions are given in table 3.1. To cover each explosive episode we randomly chose explosions from a full day. Onset velocities were determined from the first few Doppler spectra of each explosion as well as from the respective infrared sequences. Details on velocity derivation are described in the Appendix. Velocities were converted regarding the viewing geometry of each instrument under the assumption that ejecta are erupted vertically. As a consequence, the presented onset velocities relate to material movement in vertical direction and can be considered as upper limits.

	Ash-free explosions			Ash-rich explosions		
#	Day	Date	Time	Day	Date	Time
1	4	26.08.2008	12:26:34.959	8	30.08.2008	01:12:58.728
2	4	26.08.2008	14:01:28.877	8	30.08.2008	01:27:26.878
3	4	26.08.2008	15:22:22.985	8	30.08.2008	03:48:40.308
4	4	26.08.2008	17:35:28.399	8	30.08.2008	03:49:16.339
5	4	26.08.2008	21:18:08.186	8	30.08.2008	06:46:42.484
6	4	26.08.2008	22:05:01.946	8	30.08.2008	09:13:10.801
7	4	26.08.2008	22:51:28.025	8	30.08.2008	11:45:59.409
8	5	27.08.2008	00:23:39.903	8	30.08.2008	12:55:23.380
9	5	27.08.2008	01:19:03.836	8	30.08.2008	13:02:33.535
10	5	27.08.2008	01:47:30.945	8	30.08.2008	14:58:14.611
11	5	27.08.2008	03:06:59.300	8	30.08.2008	16:42:19.438
12	5	27.08.2008	04:52:49.502	8	30.08.2008	17:16:38.665
13	5	27.08.2008	05:13:43.125	8	30.08.2008	18:01:24.803
14	5	27.08.2008	07:43:23.312	8	30.08.2008	19:37:03.742
15	5	27.08.2008	08:25:39.376	8	30.08.2008	20:08:06.359

Table 3.1: List of fifteen randomly selected explosions representing the ash-rich and ash-free surface activity regime. Dates and times are given in UTC.

For most explosions we could extract the maximum vertical velocity to characterize the explosion onset. However, in a few cases it was impossible to retrieve the maximum vertical velocity from infrared footage due to the coarse pixel resolution. The ejecta were too small to produce a significant temperature signal, and were only recorded by Doppler radar. Despite these issues, we report the extracted values from infrared data to illustrate the evolution in onset velocity derived from larger particles as they are supported by a clear signal at that velocity in the Doppler radar observations.

The obtained onset velocities are shown in figure 3.7. Overall observations mirror the velocity characteristics of each activity regime, although there is a considerable overlap in onset velocity. During ash-free explosions an increase in onset velocity from about 20 m/s to up to 300 m/s can be observed. In contrast, ash-rich explosions exhibit low-velocity explosion onsets ranging from 5 m/s to 150 m/s. Velocities derived from both instruments are consistent within error bars regardless of explosion type (see figure 3.8). However, tracking high-velocity movements in infrared data appears less precise when compared to Doppler radar data.
Infrasonic waveforms recorded at the broadband station likewise confirm explosion characteristics (see figure 3.9). Ash-free explosions expose maximum excess pressures

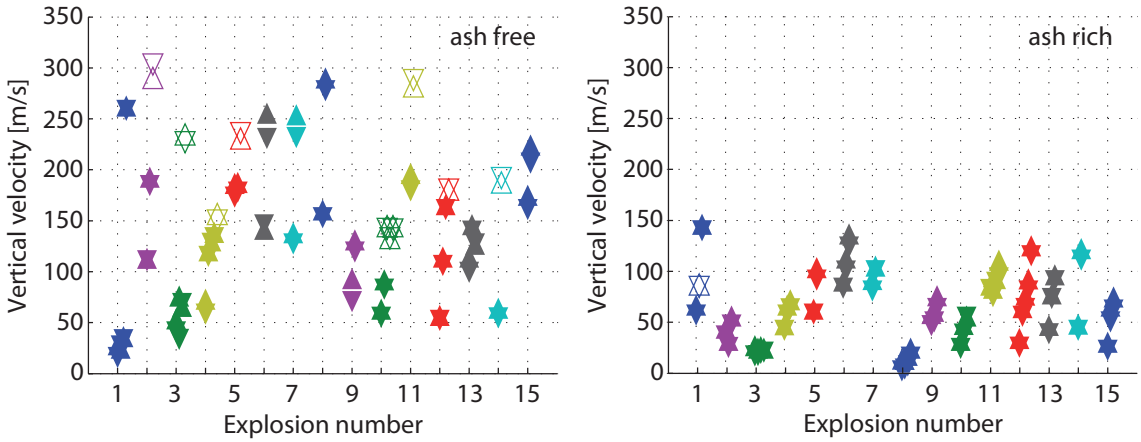

Figure 3.7: Vertical velocities as derived from Doppler radar and infrared camera data in the ash-free and ash-rich surface activity regime. Doppler radar and infrared camera velocities are depicted by downwards and upwards pointing triangles, respectively. Data points are color-coded according to explosion number. Open symbols indicate that it was impossible to extract the maximum vertical velocity from infrared camera data (details on these data points are given in the text). The overview of both surface activity regimes shows that ash-free explosions yield higher vertical velocities when compared to ash-rich explosions.

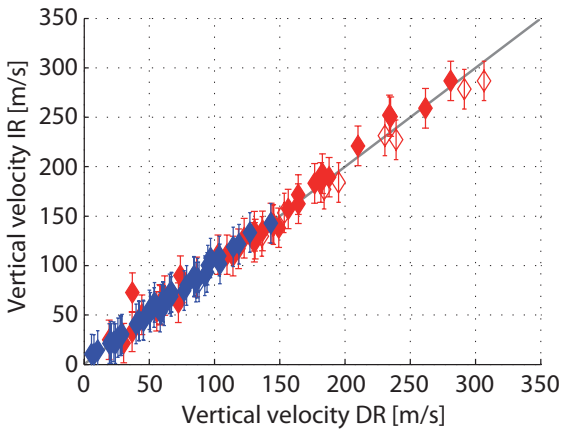

Figure 3.8: Error in vertical velocity derivation from Doppler radar and infrared camera data in the ash-free and ash-rich surface activity regime. Derived Doppler radar and infrared camera velocities are presented on the x- and y-axis, respectively. Red diamonds depict data from the ash-free regime, while blue diamonds mark data associated with ash-rich activity. The symbol width represents the error related to the manual tracking procedure in the Doppler radar data, whereas the tracking error from infrared camera data is shown in form of error bars. Perfect correlation is indicated by a gray line. The diagram illustrates that there is no major difference in velocity in the low-velocity range, however tracking high velocities in infrared camera data appears slightly less precise.

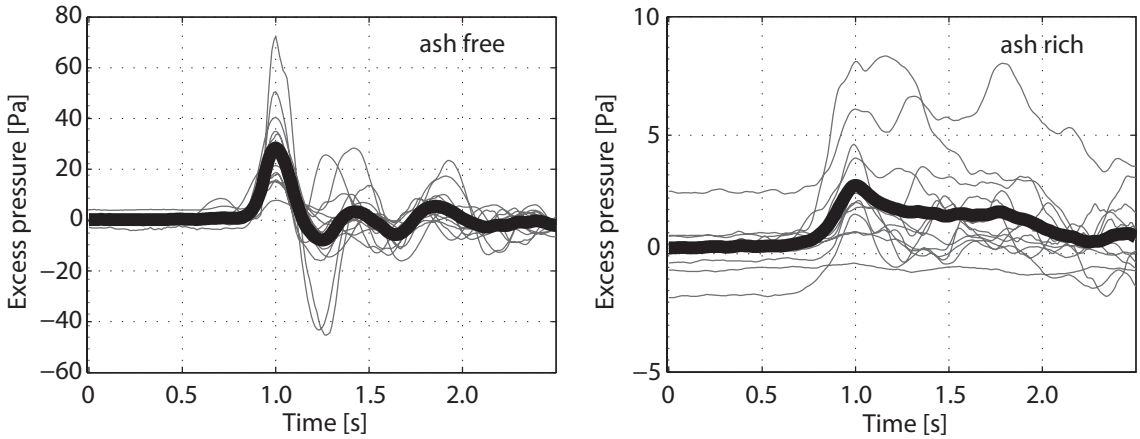

Figure 3.9: Pressure signals as recorded by infrasound in the ash-free and ash-rich surface activity regime. Single pressure traces are shown by thin black lines. The average pressure trace calculated from these signals is presented in bold. Due to significant differences in excess pressure the pressure range on the y-axis is adapted to each activity regime. The comparison of all signals corroborates the observations in figure 3.5 and figure 3.6. Signals recorded during ash-free activity feature high-pressure high-frequency waveforms, while during ash-rich activity low-amplitude low-frequency waveforms prevail.

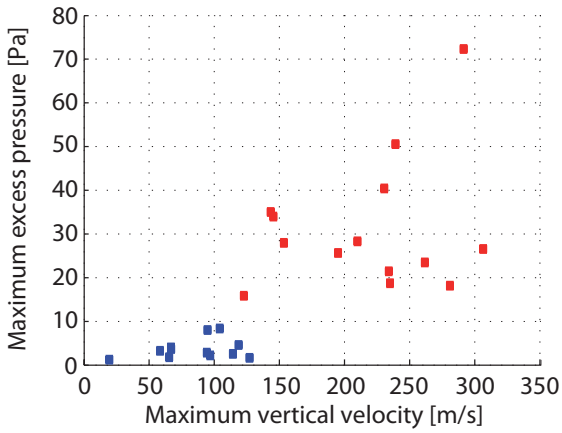

Figure 3.10: Maximum vertical velocity versus maximum excess pressure in the ash-free and ash-rich surface activity regime. Maximum vertical velocities and maximum excess pressures are presented on the x- and y-axes, respectively. Red squares depict data related to ash-free explosions, whereas blue squares mark data associated with their ash-rich counterparts. While the former show overall high maximum vertical velocities and excess pressures, the latter are characterized by low maximum vertical velocities and excess pressures. Regardless of the regime, there is no direct relation between explosion velocity and excess pressure.

of up to 75 Pa, and an impulsive signal onset followed by short-period oscillations. Ash-rich activity, on the contrary, features maximum excess pressures of less than 10 Pa, less impulsive signal onsets, and longer-lasting stretched waveforms.
A comparison of the maximum vertical velocity and maximum excess pressure of each explosion in figure 3.10 highlights the joint trend in onset velocity and pressure. While ash-free explosions show overall high maximum vertical velocities and excess pressures, ash-rich explosions are characterized by lower pressures and velocities. Despite the overall trend, there is no direct relation between explosion onset velocity and excess pressure.

3.1.8 Discussion

The geophysical signatures of Yasur's different explosive styles overall parallel observations at Stromboli volcano. At Yasur differences in radar echo power result from differential ash load of explosions. Whereas the isolated movement of coarse ballistic clasts causes low echo powers, high echo powers relate to the presence of dense ash-rich plumes (see figure 3.1). This is corroborated by qualitative insights from thermal video (see figure 3.3), which are in line with FLIR camera observations at Stromboli (*Patrick et al.*, 2007). Ash-free and ash-rich explosions at Yasur thus equal Type 1 and Type 2 explosions at Stromboli.
Like at Stromboli, explosion velocities of both explosion types exhibit a considerable overlap, however at Yasur there is a clear correlation between explosion velocity and explosive style (see figure 3.2 and figure 3.7). Maximum velocities measured by Doppler radar range up to at least 202 m/s during Type 1 explosions, while Type 2 velocities are limited to 150 m/s. When converting these values to vertical velocities as described in the Appendix we obtain peak explosion velocities of at least 437 m/s and 325 m/s, respectively.
Peak velocities of Type 1 explosions are in good agreement with Type 1 ejecta velocities derived from high-speed imaging at Stromboli's south-western vent (*Taddeucci et al.*, 2012). As pointed out by *Taddeucci et al.* (2012) these velocities are at least a factor of four higher than previously reported. The discrepancies in velocity likely result from different measurement techniques (see *Taddeucci et al.* (2012)), but also from differences in viewing geometry. At Stromboli velocities are usually measured near the inner crater rim, and the magma air interface is rarely visible. This inhibits a direct measurement of initial ejecta velocity. As a consequence, previously reported velocities from Stromboli are conservative values. In contrast, velocities at Yasur were directly measured at the vent, and the surface of the magma column was visible at the beginning of the experiment. Velocities at Yasur are hence closer to true initial velocities at the source. Discrepancies in velocity may, therefore, relate to differences in viewing geometry. The same argument holds when comparing Type

2 peak explosion velocities. Vertical Type 2 velocities of 325 m/s at Yasur are about a factor of five higher than at Stromboli (i.e. 58 m/s, see *Patrick et al.*, 2007).

Just as explosion velocities, temperatures recorded at Yasur exhibit correlated variations in thermal amplitude and explosive style (see figure 3.4). This is in line with observations at Stromboli, where differences in thermal amplitude recorded through time are thought to reflect changes in the type, amount and/or temperature of material ejected (*Ripepe et al.*, 2005a).
However, at Stromboli the relation between thermal amplitude and explosive style is reversed. According to *Ripepe et al.* (2005a) Type 2 explosions at Stromboli's SW crater show higher temperatures than Type 1 explosions at the NE crater. Our data set suggests the opposite for Yasur, higher temperatures are associated with Type 1 explosions. This inconsistence may have various reasons. First, the origin of ash at Yasur and Stromboli may be different. Visual observations of the surface of the magma column at Yasur at the beginning of our experiment suggest that fragmentation of a cold thick magmatic crust causes ash-rich explosions (see figure 3.11). In contrast, at Stromboli ash might originate from fragmentation of hot juvenile magma. Second, contrasting thermal amplitudes at Stromboli may result from differences in source location. A shallower magma level at the SW crater could lead to higher thermal amplitudes irrespective of explosion type. Third, differences in viewing geometry may explain the opposite temperature characteristics. Temperatures at Yasur were measured close to the source and represent initial values. However, at Stromboli the initial thermal signature may be altered when recorded several meters above the source. Delayed heat transfer from ash may have an important effect on temperatures further away from the source.

Similar to explosion velocities and temperatures, the correlation between excess pressure and explosive style (see figure 3.5) likewise agrees with observations at Stromboli. At both volcanoes Type 1 explosions produce high-amplitude pressure waves, while Type 2 activity causes small excess pressures.
At Stromboli pressures range between 20 - 80 Pa and 10 – 30 Pa 350 m away from the source for Type 1 and Type 2 explosions (*Ripepe and Marchetti*, 2002). At Yasur differences in pressures are more pronounced. At a source distance of 640 m Type 1 explosions expose pressures of 10 - 140 Pa, whereas Type 2 explosions show pressures of 2 - 50 Pa (see figure 3.5 and figure 3.9). The higher upper pressure limit for both explosions types demonstrates the overall higher intensity of explosions at Yasur.
Besides their different intensity, infrasonic signals at Yasur and Stromboli are characterized by a different spectral content. At Stromboli signal power is centered between 5 - 6 Hz regardless of explosion type (*Ripepe and Marchetti*, 2002). However, at Yasur Type 1 and Type 2 explosions feature contrasting signal power distributions

Figure 3.11: Image series of surface activity at vent A. Type 1 explosions relate to a clear busting of gas slugs at the magma free surface expelling hot liquid lava fragments. Type 2 explosions involve fragmentation of a cold thick magmatic crust at the magma air interface. Images were acquired by a custom camera at 10 fps. Images courtesy of Alexander Gerst.

between 0.1 - 3 Hz and 0.1 - 0.5 Hz (see figure 3.6). These differences in frequency relate to changes in infrasonic waveforms (see figure 3.9). This may point to a change in explosion dynamics, but may also indicate changes in wave propagation. Since hot volcanic gas moves at high velocities during Type 1 explosions pressure signals can be altered by Doppler shifting (*Woulff and McGetchin*, 1976). In addition to that, lower excess pressures during Type 2 explosions may partly result from diminished acoustic radiation due to ash-load damping. This might explain the weak coupling between explosion velocity and excess pressure (see figure 3.10).

Despite the weak coupling of explosion velocity and excess pressure, the temporal trend in both data types demonstrates a general correlation between explosion intensity and explosive style. Like at Stromboli, both explosion forms are common at one vent, and show regime-like persistence over a certain time period. Comparison of the associated timescales however reveals shorter persistence at Yasur. During our experiment Type 1 and Type 2 explosions persisted for about 4 days (see e.g. figure 3.5), whereas *Patrick et al.* (2007) reported timescales between 13 days and 2 month for Stromboli. The differences in timescale are in line with the markedly higher activity at Yasur. From our data set we calculate an average explosion frequency of 161 events/h, which is about a factor of twelve higher than at Stromboli (i.e. 13 events/h, see *Ripepe et al.*, 2008). Along with the overall higher explosion

intensity, this indicates a faster magma supply and more vigorous activity at Yasur.

The present link between changes in explosion intensity and shifts in explosive style further allows us to speculate about the origin of Type 1 and Type 2 explosions. Visual observations at Yasur show that Type 1 explosions relate to the common perception of Strombolian activity (see figure 3.11). The vigorous bursting of gas slugs at the magma free surface entails rapid expansion and ultimate breakup of fluid magma surrounding the slug nose. This leads to the ejection of coarse, incandescent clasts along ballistic trajectories, which is also observed at Stromboli. Unlike the traditional view of fragmentation, during these explosions it is the inertia of expanding fluid that drives fragmentation (*Namiki and Manga*, 2008).
As already discussed by *Patrick et al.* (2007), fine-scale fragmentation during Type 2 activity cannot be explained in the same way. Fine particles and ash in Type 2 explosions are thought to originate either from backfilled material due to conduit wall slumping and ejecta roll back, or from rheological changes in the uppermost magma column. The interpretation of our data set suggests that changes in magmatic rheology are the main cause of Type 2 behavior for several reasons. First, visual observations of the magma free surface (see figure 3.11) favor fragmentation of a cold thick magmatic crust during low-intensity Type 2 explosions. Second, Type 2 activity was consistently observed at the beginning of our experiment when the magma level was highest. This was followed by a drop in magma level and concurrent Type 1 activity. However, backfilling is normally encouraged by a drop in magma level (*Calvari and Pinkerton*, 2004), which would lead to an opposed cycle of activity. The occurrence of the first Type 1 and Type 2 phase thus argues against the backfilling mechanism. Third, the regime-like persistence of each explosive style dismisses discrete events of material backfill. To explain the consistency in style throughout time a continuous mechanism is needed. Finally, the gradual increase in echo power on day six, seven and eight (see figure 3.1) mirrors a progressive increase of ash content in explosions, which may indicate an increase in brittle fragmentation due to magma aging. The simultaneous decrease in explosion intensity and temperature as well as a lower explosion frequency (see *Meier et al.*, 2014a, chapter 4) additionally supports a decrease in activity which would favor magma outgassing, crystallization and cooling of an increasingly viscous crust at the magma free surface. Irrespective of fine-scale fragmentation, the correlation between explosion intensity and explosive style further suggests that Type 2 behavior consistently involves smaller gas overpressures and volumes than Type 1 activity (*James et al.*, 2009). This is good agreement with results from *Kremers et al.* (2013) who observed smaller seismic ground velocities during Type 2 behavior, and a general correlation between source volume and maximum particle velocity at Yasur.
Despite the above argument, from geophysical data alone it is difficult to reach an exclusive conclusion. Continuous sampling of ejecta at vent A would have helped

to assess changes in magma maturity in the upper conduit and to link our results directly to variations in magma rheology (*Lautze and Houghton*, 2007; *Taddeucci et al.*, 2002). Unfortunately, eruptive products of vent A were only sampled once during our experiment. Still it is worth noting that the comparison to eruptive products of vent C indicates a link between explosion intensity and magma rheology (*Kremers et al.*, 2012). In addition to that, the present differences in explosion intensity between Type 1 and Type 2 explosions may point to variations in magma vesiculation (*Colò et al.*, 2010). These variations feed back to changes in magma viscosity and could have been traced by systematic sampling of ejecta.

3.1.9 Summary and Final Remarks

We studied the surface activity of Yasur volcano, Vanuatu, to assess its relation to, and implications for, typical Strombolian activity. For this purpose we analyzed a continuous multi-parameter data set including Doppler radar, infrared and infrasound data. These data provide new insights into Strombolian explosive styles and source conditions. The specific findings from this study can be summarized as follows:

(1) Ash-free and ash-rich explosive styles at Yasur volcano overall equal Type 1 and Type 2 explosive styles at Stromboli volcano. The isolated movement of hot ballistic clasts during ash-free explosions causes low echo powers, high explosion velocities and high temperatures at the vent. In contrast, the movement of cold particle-rich plumes during ash-rich explosions leads to high echo powers, low explosion velocities and low temperatures at the vent exit. In addition, ash-free explosions feature high excess pressure signals exhibiting high frequencies opposed to low-amplitude low-frequency signals accompanying ash-rich activity.

(2) Irrespective of explosion type there is no direct relation between explosion onset velocity and excess pressure. Differences in excess pressure and signal frequency between explosion types relate to changes in infrasonic waveforms. This suggests a different explosion dynamics, but may also denote changes in local wave propagation.

(3) Surface activity at Yasur follows a joint temporal trend in terms of material movement, temperature and pressure related to explosions. This trend reveals the regime-like persistence of a given explosive style through time. In terms of explosion velocity and excess pressure there is a general correlation between explosive style and explosion intensity.

(4) In comparison to Stromboli Yasur exhibits an overall higher explosion intensity characterized by higher excess pressures. A given explosive style persists over a shorter time period. In combination with a higher explosion frequency, this indicates more vigorous activity and a faster magma supply at Yasur.

(5) The correlation between explosion intensity and explosive style suggests that ash-rich explosions involve smaller gas overpressures and volumes than ash-free explosions. Interpretation of our data with reference to explosion style transitions, magma level fluctuations and explosion style persistence implies that changes in magmatic rheology are the main cause of ash-rich fragmentation. This is corroborated by visual observations of the magma free surface which favor fragmentation of a cold thick magmatic crust during ash-rich explosions.

In general, this study strengthens previous findings from measurements at Stromboli volcano. The continuity of our data set allowed us to broadly track variations in surface activity and thus to improve our understanding of explosion style characteristics and explosion style transitions. Our work highlights the impact of continuous data acquisition campaigns and stimulates similar studies to determine the role of potential changes in volcanic gas emissions during normal Strombolian activity.

3.1.10 Appendix

Derivation Of Explosion Onset Velocities

To derive explosion onset velocities from Doppler radar and infrared camera data we followed a two step procedure. At first, we extracted the maximum velocities at the onset of each explosion from both data types. For this purpose we studied the recorded Doppler spectra in detail and hand-picked the maximum velocities at the onset of each explosion. Picking was performed via a self-developed software with an accuracy of $\pm$ 2.5 m/s.
To gather velocity information from infrared footage we converted the relevant image files to Audio Video Interleave (avi) sequences. Based on these sequences explosion onset velocities were then assessed by using the ImageJ freeware and the MTrackJ plug-in (*Abramoff et al.*, 2004; *Meijering et al.*, 2012). To be consistent we defined an area of analysis equal to the FOV of the radar in which we tracked either the fastest pyroclasts or the front of the ash-plume. Irrespective of explosion type material moved mainly in vertical direction and trajectories were tracked accordingly. A new trajectory was initiated every frame focusing on the fastest movement to derive velocity information in analogy to the radar. As a consequence, velocities were

calculated over a relatively small distance before material exited the analysis area, and an overall time span of six frames (0.24 s) was considered at most. Due to the coarse resolution of our thermal recordings velocity determination was ambiguous by ± 1 pixel from frame to frame, i.e. ± 20 m/s.
After velocity extraction the second step consisted in velocity conversion. The reasons for this were twofold. First, the extracted velocities from both data types represent different velocity components as depicted in figure 3.12. The one-dimensional view of the Doppler radar only accounts for velocity components along the radar beam, but not perpendicular to it. In contrast, the two-dimensional view of the infrared camera projects all velocities onto a plane parallel to the FOV. To compare velocities from both instruments it is therefore necessary to convert the extracted values to the same velocity component. Second, the extracted velocities from both data types are conservative values in case of material movement in vertical direction. As stated above, both data types contain only a certain velocity component instead of actual velocity values. Yet during the well-collimated, initial phases of explosive events ejecta are mainly erupted vertically. We thus decided to convert all extracted velocities to vertical values. As a result, all Doppler radar velocities were divided by the sine of the tilt angle of the Doppler radar α, whereas all velocities from thermal footage were divided by the cosine of the tilt angle of the camera β. The same procedure was applied to the errors in velocity derivation.

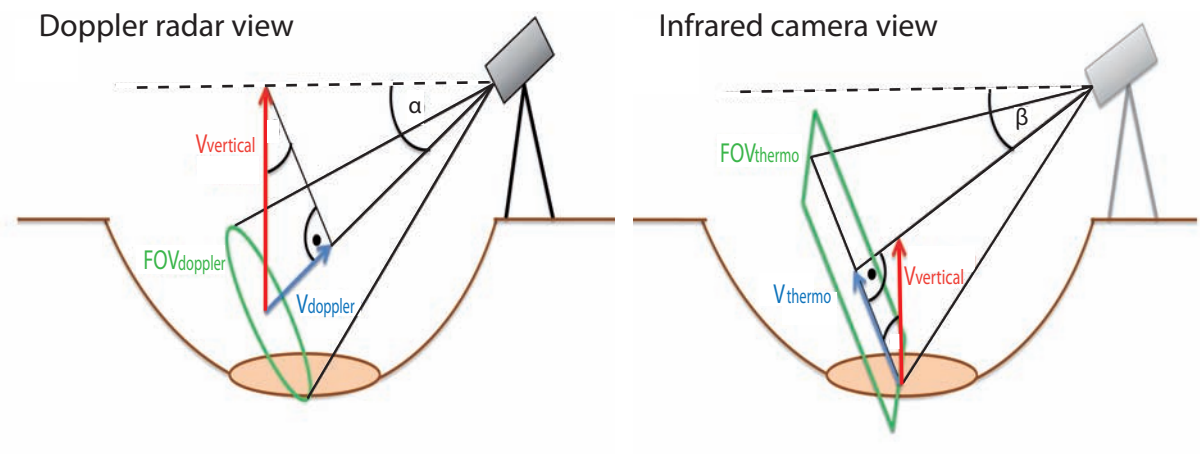

Figure 3.12: Schematic sketch of the velocity component measured by Doppler radar and infrared camera modified after *Walk* (2010). The relation between the velocities measured by Doppler radar and the actual vertical velocities is depicted on the left. The velocity component measured by the infrared camera and its relation to the actual vertical velocities is shown on the right.

3.2 On Infrasound Wave Propagation Effects in the Presence of Small Volcanic Clouds

3.2.1 Abstract

Infrasound is a powerful tool and a well-accepted technique to monitor volcanic surface activity. The recorded pressure traces are often used to estimate characteristics or the mechanism of the related source processes. For this purpose local wave propagation is often considered to be uniform. However, time-dependent changes in the propagation medium may cause signal alteration. To demonstrate this effect we modeled the propagation of infrasonic waves in the presence of volcanic clouds. Here, we compare three representative Strombolian-type scenarios, namely wave propagation in the presence of standard atmospheric conditions (1), of a fast-moving hot gas cloud (2) and of a slow-moving cold gas-ash mixture (3). Our results reveal a modification of the signals due to Doppler shifting, density, transmission and interference effects. In the ash-free scenario we observe frequency shifts of up to 1 Hz. These frequency shifts can be explained by a simple theoretical model. Comparing the total acoustic energy we identify an overestimation in the ash-free and an underestimation in the ash-rich case by a factor of 1.2 and 0.1, respectively. These factors relate to different amplitude characteristics in both scenarios. For real data they can be considered upper limits. Given the model setup they exclude signal components generated ahead of the cloud. In general, our findings highlight that contrasting infrasound signatures may result from potential changes in the propagation medium, and do not necessarily reflect changing source dynamics. A proper knowledge of local atmospheric properties is essential when interpreting source physics from infrasound observations.

3.2.2 Introduction

The analysis of infrasonic pressure traces has become a principal method to better understand volcanic explosion dynamics. Many researchers have estimated source characteristics (*Johnson et al.*, 2008), exit velocities (*Woulff and McGetchin*, 1976; *Caplan-Auerbach et al.*, 2010) or the mass flux of volcanic eruptions (*Johnson et al.*, 2004; *Caplan-Auerbach et al.*, 2008) via different techniques. Several studies are based on the calculation of the sound pressure level (*Johnson*, 2003) or the total acoustic energy (*Firstov and Kravchenko*, 1996; *Johnson*, 2003; *Vergniolle et al.*, 2004). These parameters are often used alone or along with other data types to study the changing nature of explosive eruptions or to intercompare explosion styles between different volcanoes (*Johnson et al.*, 2003; *Caplan-Auerbach and McNutt*,

2003; *Johnson and Aster*, 2005; *Marchetti et al.*, 2009). In order to asses the shallow source dynamics of a single volcanic system it is common to interpret the infrasonic waveform itself. This led to the postulation of bubble oscillations (*Vergniolle et al.*, 1996; *Cannata et al.*, 2009) or of resonator effects (*Buckingham and Garcés*, 1996). In addition to that, major progress has been made exploring telemetric infrasound. It is well-known that at large distances signals are modified by path effects (*Fee et al.*, 2011), and that telemetric recordings may be used to understand the structure of the atmosphere (*Le Pichon et al.*, 2009). Along the same lines long-range recordings can witness changes in the propagation setting. Large scale volcanic eruptions may perturb the atmospheric structure near the source and affect sound propagation (*Fee et al.*, 2010a; *Matoza et al.*, 2011). Yet it is a common assumption that in the direct volcanic environment no path effects are to be expected (e.g. *Arrowsmith et al.*, 2010). On local distances, i.e. distances up to 10 km, infrasonic airwaves are thought to offer a quite unfiltered representation of source motions as the atmosphere is considered a simple stationary propagation medium (*Johnson and Ripepe*, 2011).
Nonetheless, from several observations we know that also on local distances the propagation medium can be highly variable. Small scale ash plumes (*Patrick et al.*, 2007; *Bluth and Rose*, 2004; *Wilson and Self*, 1980) or developing eruption columns (*Fee et al.*, 2010b; *Petersen et al.*, 2006) may alter the wave propagation path. It is therefore likely that during an eruption the change in temperature and composition of the atmosphere due to the ejection of volcanic gas or a gas-ash mixture affects the local density and sound speed. Since the medium in and around the vent is a hot, multi-phase system of gas and particles moving at high velocities we can expect Doppler shifting (*Woulff and McGetchin*, 1976). Unfortunately, there is only scarce information on the possible attenuation and spectral behavior of infrasound signals under these conditions as source and propagation effects appear strongly interweaved. One indication is a study by *Mori et al.* (1989) who observed diminished acoustic radiation at Langila volcano during ash-loaded eruptions. Similar observations were made at Stromboli volcano where long lasting emissions of ash and fine incandescent ejecta produced low pressure infrasonic signals (*Ripepe and Marchetti*, 2002). Regarding the acoustic spectrum a shift to lower frequencies seems to be related to either ash bursting activity (*Caplan-Auerbach et al.*, 2010) or to the transition from a sustained to collapsed eruption column (*Fee et al.*, 2010b). These observations are corroborated by a recent study of *Meier et al.* (2014b) (see chapter 3) at Yasur volcano where a change in frequency content occurred along with a clear decrease in signal amplitude during a phase of increased ash loading.

A more general variability of acoustic energy radiated into the atmosphere was also found at other volcanoes. Yet the processes decreasing acoustic efficiency have been limited to a density increase of the erupted material, viscous flow losses in the conduit or source dimension variability (*Johnson and Aster*, 2005). To our knowl-

edge the influence of path effects related to the presence of a moving gas-particle mixture has not been discussed so far. This paper intends to fill that gap. To investigate whether local propagation effects may lead to different signal signatures we modeled infrasound wave propagation in temporally changing media. As our modeling approach strictly aims at the quantification of path effects we employed equal initial conditions defined by identical and stationary source signals. Based on this concept we compare three scenarios, namely wave propagation in the absence of any special medium, during high-velocity spreading of a hot gas cloud and during low-velocity spreading of a cold gas-ash mixture. The interpretation of the selected examples shows that high-velocity cloud movement causes Doppler shifting, and that the arising impedance contrasts result in a clear modification of the signal amplitude. Discussion of these findings with reference to real data recorded at Yasur demonstrates that contrasting signal signatures could possibly result from changes in the propagation medium.

3.2.3 Numerical Model

Basic Principles

To model and understand wave propagation in gas and gas-ash mixtures one has to consider general two-phase flow theory. In this context pressure waves are highly dispersive implying that waves propagate at the normal gas sound speed at short wavelengths, at the reduced mixture or pseudo-gas sound speed at large wavelengths, and are completely attenuated and blocked at intermediate wavelengths (*Bercovici and Michaut*, 2010). In order to determine the correct propagation regime it is necessary to compare the characteristic time scale of the wave field to the characteristic equilibration times of the particles inside the mixture. Following e.g. *Marble* (1970), the effects of suspended particles on wave propagation in a gas under the assumption of no particle interaction are drag and heat transfer processes. Assuming that particle drag is described by Stokes flow and heat transfer by a Nusselt number of unity the characteristic equilibration times between the particles and the gas are

$$\tau_v = \frac{m}{6\pi\sigma\mu} \tag{3.1}$$

$$\tau_t = \frac{m\zeta_p}{4\pi\sigma k} \tag{3.2}$$

Here, τ_v is the time required by a particle to adjust to the local motion of the gas, and τ_t the time for thermal equilibration. m, σ, ζ_p and k are the mass, radius,

specific heat capacity and thermal conductivity of a single particle in the mixture, and μ is the viscosity of the gas. In case of a volcanic cloud made up of ash particles smaller than 1 mm, and incorporating a specific heat capacity of 840 J/kgK, and a heat transfer coefficient of 80 W/m^{2}K (e.g. *Stroberg et al.*, 2010) this leaves us with times scales of $\tau_v = \mathcal{O}(1 \times 10^{-3})$ and $\tau_t = \mathcal{O}(1 \times 10^{-4})$. Comparing these to the time scale of the wave field τ which is in this study given by the infrasonic frequency range we find $\tau >> \tau_v, \tau_t$. The equilibration processes are thus quasi-instantaneous, and we can treat the gas-ash mixture as a pseudo-gas. In the validity range of this approximation wave propagation is described by the acoustic wave equation (*Bercovici and Michaut*, 2010; *Pelanti and Leveque*, 2006), and the density and the speed of sound inside the volcanic cloud are given by (e.g. *Valentine and Wohletz*, 1989)

$$\rho_{mix} = \theta\rho_s + (1-\theta)\rho_g \tag{3.3}$$

$$c_{mix} = \sqrt{\frac{c_{pg} + \phi c_{vs}}{c_{vg} + \phi c_{vs}} \frac{c_{vg}(1-\gamma_g)T}{1+\phi}} \tag{3.4}$$

The subscripts g and s denote the gas and solid phases while θ and ϕ are the volume and the mass fraction of the solid phase only. c_p and c_v are the heat capacities at constant pressure and volume, and γ is their ratio.

Model approach

Following the previous considerations we modeled infrasound wave propagation in gas and gas-ash mixtures via the acoustic wave equation

$$\frac{\partial}{\partial x}\left(\frac{1}{\rho}\frac{\partial P}{\partial x}\right) + \frac{\partial}{\partial y}\left(\frac{1}{\rho}\frac{\partial P}{\partial y}\right) + \frac{\partial}{\partial z}\left(\frac{1}{\rho}\frac{\partial P}{\partial z}\right) = \frac{1}{c^2\rho}\ddot{P} + \frac{s}{\rho} \tag{3.5}$$

Solving this equation one finds the pressure field $P(x, y, z, t)$ caused by a source signal s propagating at the speed of sound $c(x, y, z)$ through a density field $\rho(x, y, z)$. In order to obtain the pressure field we implemented a 2D and a 3D forward modeling algorithm adopting a Fourier method (*Kosloff and Baysal*, 1982). This method makes use of a numerical grid to calculate the spatial derivatives by a fast Fourier transform. The time derivatives in the wave equation are subsequently calculated by second order differencing.

Since our study aims at the quantification of path effects it was crucial to employ equal starting conditions in each modeling scenario. We therefore chose a Ricker wavelet with a main frequency of 1.6 Hz as a source term in all model runs. To investigate wave propagation in three different cases, i.e. (1) in the absence of any special medium, (2) during high-velocity spreading of a hot gas cloud and (3) during low-velocity spreading of a cold ash cloud, we set up a first scenario consisting of a background medium only, and a second and third scenario consisting of a background medium in which a cloud is expanding over time. The propagation medium is thus defined either by the density and the speed of sound of the background medium alone, or along with the density and speed of sound of the cloud.
The radial spreading of the cloud was implemented by updating the propagation medium depending on the cloud's spreading velocity v. In order to describe wave propagation inside the volcanic cloud we employed an effective motionless medium approximation (*Godin*, 2002). This approximation reduces wave propagation in a moving fluid to wave propagation in a resting fluid with an effective sound speed $c_e = c + v$ and an effective density $\rho_e = \rho c^2/c_e^2$. It holds as long as the medium velocity is small compared to its sound speed, and aligned along the direction of sound propagation. Considering the input parameter space presented in the following section this is valid in all simulations.

Input Parameter Space

To constrain the input parameter space we implemented a background medium representing standard atmospheric conditions at 25 °C in all three cases. In order to set up the cloud models we then calculated the density and the speed of sound using equations 3.3 and 3.4. Assuming a mean volcanic gas composition of 40 vol.% carbon dioxide and 60 vol.% water vapour (*Schmincke*, 2004) the density and the speed of sound depend on the gas mass fraction and the temperature as shown in figure 3.13. Here, the specific heat capacities of the gas mixture were obtained as a weighted sum of the heat capacities of the single gas components, and we used a polynominal description to specify their dependency on temperature (*Moran and Shapiro*, 2007). The specific heat of the solid ash component was again set to 840 J/kgK.

Based on the shown relationships we defined the cloud scenarios via their gas mass fraction, and their temperature along with their spreading velocity. Table 3.2 summarizes the selected parameters as well as the resulting original and effective density and speed of sound for each model run. Since there are several parameter combinations related to different types of volcanic activity we decided on modeling two end-member Strombolian-type scenarios. These eruption styles are most studied in terms

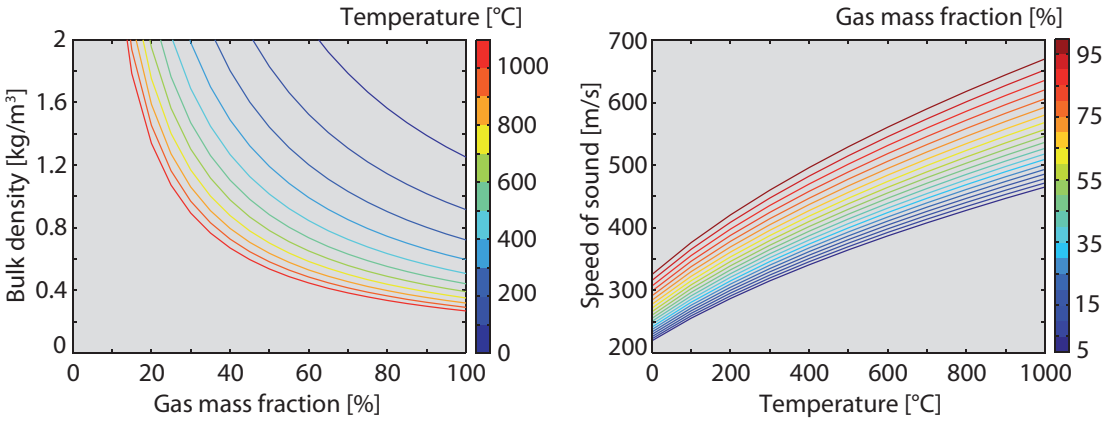

Figure 3.13: Density and speed of sound inside a volcanic cloud depending on gas mass fraction and temperature. The density is shown as a function of gas mass fraction color-coded by temperature on the right, as opposed to the speed of sound which is given as a function of temperature color-coded by gas mass fraction on the left. The density is decreasing with increasing gas mass fraction and increasing temperature, whereas the speed of sound is increasing under the same conditions. Note that both parameters are presented depending on the mass fraction of the gas phase as this is more intuitive.

Scenario	T [°C]	GMF [%]	ρ [kg/m^3]	c [m/s]	v [m/s]	ρ_e [kg/m^3]	c_e [m/s]
1	–	–	1.18	346	–	–	–
2	800	95	0.33	600	180	0.20	780
3	300	15	3.96	324	30	3.32	354

Table 3.2: Summary of the input parameters for all modeled scenarios. Temperatures (T) and gas mass fractions (GMF) are listed along with the related densities (ρ) and speeds of sound (c). The cloud spreading velocity (v) as well as the effective density (ρ_e) and effective speed of sound (c_e) are given for scenario (2) and (3).

of gas mass fractions, temperatures and cloud velocities (*Patrick*, 2007, and references therein). In this framework the case of a fast-moving hot gas cloud can be considered a Type 1 explosion, whereas a slow-moving cold gas-ash mixture corresponds to Type 2 activity. The gas mass fractions represent conditions close to the vent, and do not include longer-term processes such as air entrainment or particle sedimentation. The temperatures are average temperatures of the gas-ash mixture assuming instantaneous thermal equilibrium. Spreading velocities of Type 1 explosions relate to the initial velocity of the gas phase only, and recent Doppler Radar measurements at Yasur suggest 180 m/s being a reasonable upper limit (*Meier et al.*, 2009). The presented Type 2 velocities were averaged to 30 m/s based on measurements at Stromboli (*Blackburn et al.*, 1976; *Patrick et al.*, 2007). According to the explosion type the gas mass fractions and temperatures were chosen to mirror either a gas phase close to magmatic temperature, or a mixture of gas and entrained ash at ambient temperature. The initial cloud radius was set to 7.5 m corresponding to vent radii commonly found at Strombolian volcanoes.

Model Results

The model results were obtained in a stepwise process. To ensure a proper selection of the grid spacing, and the time step in the forward modeling procedure we first carried out a parameter study in the 2D domain. Based on our observations we selected a final grid spacing of 6 m, and a time step of 75 ms. Considering the input parameter space this selection is in line with a set up of a dispersion-free grid of at least 10 points per wavelength (*Kosloff and Baysal*, 1982). To guarantee the absence of artefacts in the 3D models, selected parts of the wave field were cross-validated with corresponding high-resolution results from the 2D domain.

Figure 3.14 presents a 2D snapshot of the 3D wave field, and the recorded waveform at 600 m source distance for each modeled scenario. The important part of the wave field is its exterior as the inner part is dominated by interference with internal cloud reflections. Comparing the ash-free waveform to the reference signal we find that the ash-free scenario is characterized by an earlier signal arrival, and higher frequencies. The average amplitude is comparable to the one in the reference scenario, but the onset of the signal is more pronounced. The positive onset of the waveform is almost doubled, and followed by a prominent negative component. Considering the spectra we observe a frequency shift from 1.6 Hz to 2.6 Hz. In contrast, the comparison of the ash-rich case and the reference scenario indicates a similar signal frequency. However, there is a clear attenuation of the amplitude in the presence of the ash cloud.

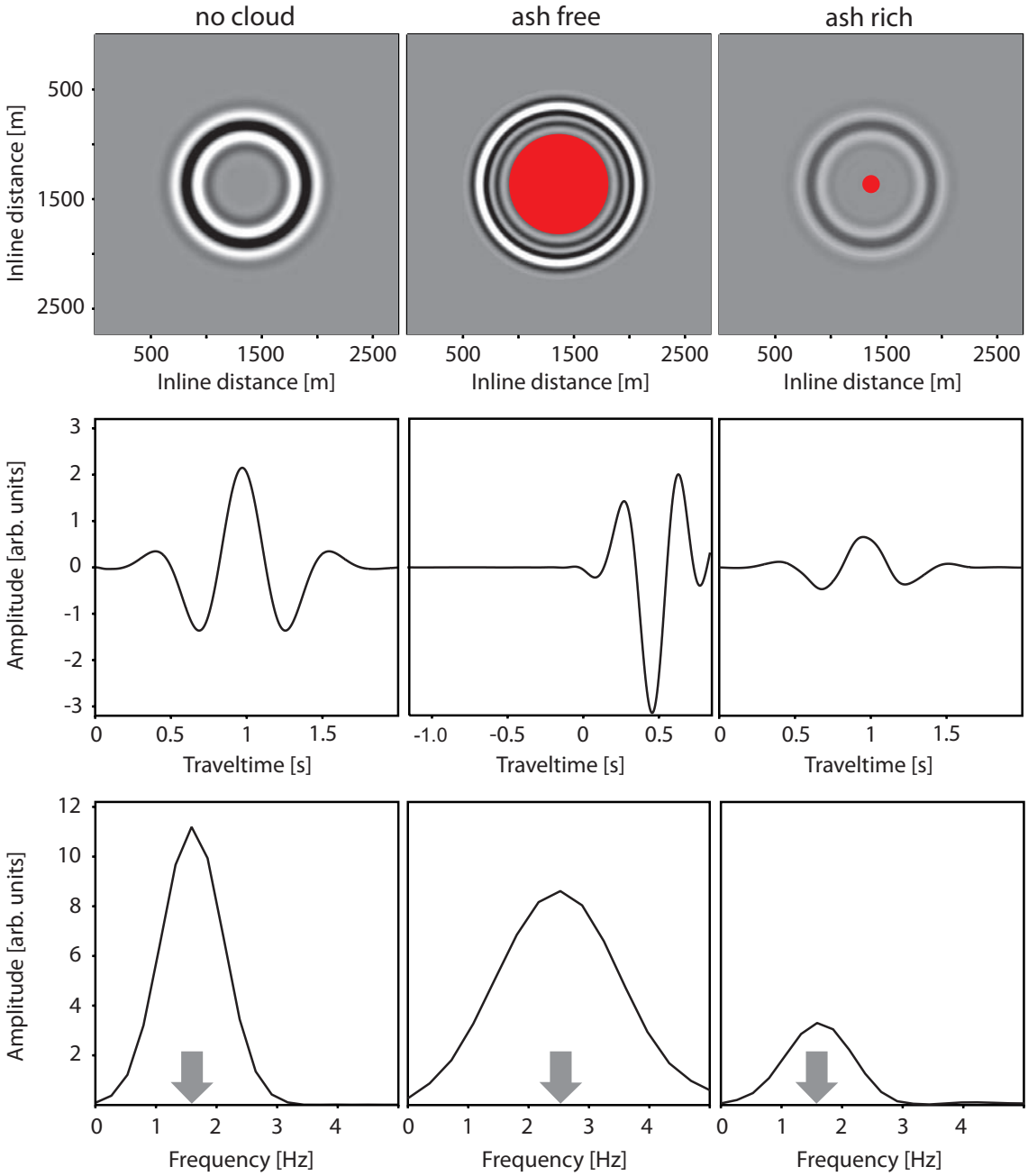

Figure 3.14: Comparison of the different 3D wave propagation scenarios. The results for each scenario are presented column-wise. The reference case is labeled as 'no cloud', whereas the fast-moving hot gas cloud scenario is labeled as 'ash free', and the slow-moving cold ash cloud scenario as 'ash rich'. On the top, a snapshot of the same wave field slice is displayed for each case, and a red circle indicates the position of the cloud. In the middle the recorded waveform at 600 m source distance is shown, and at the bottom the related spectra are given. Traveltimes are marked relative to the reference case. Grey arrows map the frequencies calculated in the frame of our theoretical model (see section 3.2.4 below). A comparison of the columns reveals that the arising impedance contrasts result in a clear modification of the signal amplitude, and that the high-velocity cloud movement causes frequency shifting.

3.2.4 Theoretical Interpretation

Frequency Shift

To explain the frequency shift we developed a simple theoretical model. Figure 3.15 shows its derivation for the ash-free case. Considering a traveltime diagram the propagation of a volcanic cloud is characterized by its spreading velocity v_{cloud} marked by the thick black line. At distances close to the vent infrasound waves propagate inside the cloud at the effective speed of sound c_{cloud}. When reaching the cloud boundary the signals are transmitted into the background medium, and propagate further at the speed of sound of warm air c_{air}. The slope of all lines is defined by the relation $c_{cloud} > c_{air} >> v_{cloud}$. The duration of signal generation at the source is given by the period of the source signal T_{src}, and T_{rec} is the duration, i.e. the period, of the corresponding recorded signal. Based on these relations we can relate the period of the source signal at zero distance to the period of the recorded signal at a certain distance X outside the expanding cloud via the auxiliary variable t. This leaves us with the equations

$$t = T_{src} + X/c_{cloud} \tag{3.6}$$
$$t = T_{rec} + X/c_{air} \tag{3.7}$$
$$t = X/v_{cloud} \tag{3.8}$$

Combing equations 3.6 and 3.8, and equations 3.7 and 3.8 we obtain one formula for T_{src} and one for T_{rec}. Building their ratio we end up relating the frequency of the recorded signal to the frequency of the source signal

$$f_{rec} = f_{src} \frac{1 - v_{cloud}/c_{cloud}}{1 - v_{cloud}/c_{air}} \tag{3.9}$$

Using this formula we calculated the recorded frequencies assuming the source frequency from the numerical model. To study the ash-free and the ash-rich scenario

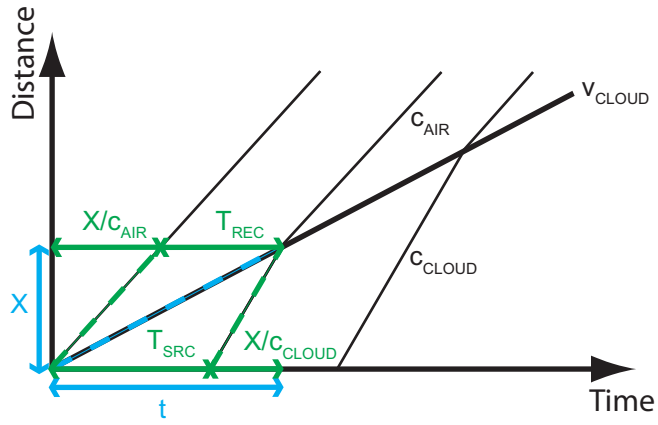

Figure 3.15: Derivation of the frequency shift for the ash-free scenario. The black lines correspond to the spreading volcanic cloud, as well as the infrasound signals propagating in- and outside the cloud. The color-coded parts of the figure are used to relate the period of the source signal to the period of the recorded signal. More details are given in the text.

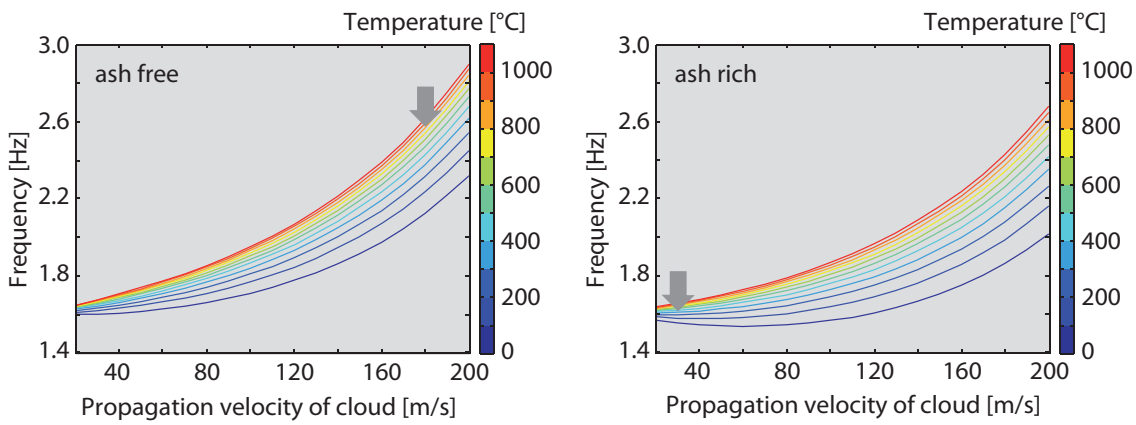

Figure 3.16: Relation between cloud spreading velocity and recorded frequency color-coded by temperature for the ash-free and ash-rich scenario. The recorded frequency is shown as a function of cloud spreading velocity starting at 20 m/s. On the left the gas mass fraction is fixed to 95 % to mirror the ash-free case, whereas on the right a gas mass fraction of 15 % represents the ash-rich scenario. In the ash-free case the recorded frequency is strongly increasing with increasing cloud spreading velocity and increasing temperature, while in the ash-rich scenario the recorded frequency increase is less pronounced due to the overall lower sound speed inside the cloud. Grey arrows mark the temperatures and the spreading velocities from the numerical model runs.

we fixed the gas mass fraction, and determined the frequency for a range of cloud spreading velocities and temperatures.

Figure 3.16 shows the resulting frequencies for the different scenarios. The calculations reveal that the ash-free case is characterized by a frequency increase with

increasing cloud spreading velocity and increasing temperature. A shift to lower frequencies is non-existent as the speed of sound inside the cloud is always larger than the one of the surrounding atmosphere. However, in the ash-rich scenario the speed of sound inside the cloud is generally lower (see figure 3.13). As a consequence the frequency increase is less pronounced, and a shift to lower frequencies is present at small spreading velocities and temperatures.
In any case, the frequency shift strongly depends on the cloud spreading velocity indicative of a Doppler shifting process. This interpretation is in good agreement with the results from the numerical model. According to the high cloud spreading velocity of 180 m/s we find the same frequency shift to about 2.6 Hz in the ash-free case. In the ash-rich scenario the low cloud spreading velocity results in almost no frequency shift.

Amplitude Characteristics

The processes controlling the amplitude characteristics of the signals can be divided into density, transmission and interference effects. As indicated by equation 3.5 the amplitude of the signal propagating away from the source equals the source wavelet divided by the density of the surrounding medium. Under standard atmospheric conditions this is the only process altering the signal amplitude.

According to this the recorded signal is the same, but smaller than the original source wavelet (see figure 3.17). In the cloud scenarios, however, the signal amplitude is not only influenced by the density of the surrounding medium, but also by the transmission through the cloud boundary. Depending on the impedance contrast the amplitude decreases or increases. Since the impedance of the background medium is larger than the one of the ash-free cloud only part of the signal is transmitted in this case. Yet the comparison of the resulting wavelet and the recorded signal in figure 3.17 reveals that the recorded signal is smaller than the density and transmission corrected wavelet. This demonstrates that the density and transmission effect only partly mirror the processes controlling the amplitude characteristics of the signal.
The ash-rich scenario supports this observation though under reversed conditions. Here, the large density inside the cloud leads to an attenuation of the source wavelet which subsequently experiences an amplification entering the lower impedance background medium. Like in the ash-free case differences between the resulting wavelet and the recorded signal remain. These differences result from interference effects between the primary signal and its reflections at the cloud boundary. Since the wavelength of the source wavelet is clearly larger than the cloud size this is a non-negligible process. During signal generation the head of the signal already reaches

the cloud boundary, and is transmitted and reflected. The reflected part of the signals then propagates back inside the cloud where it interferes with the primary signal. Due to the movement of the cloud the interference pattern depends on the reflection coefficient, but also on the cloud spreading velocity. As a consequence the amplitude characteristics are different in the ash-free and ash-rich case.

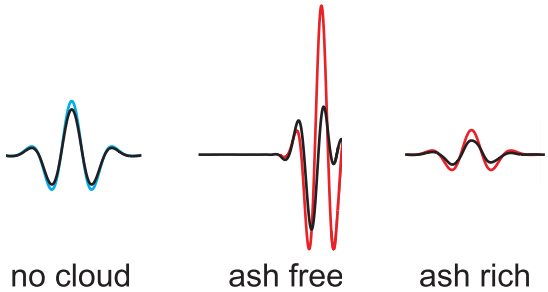

Figure 3.17: Source wavelet and recorded signal in the background medium compared to the density and transmission corrected wavelet and recorded signal in the ash-free and ash-rich case. The results of the background medium are given on the left, whereas the density and transmission corrected wavelet and recorded signal in the ash-free and ash-rich case are shown in the middle and on the right, respectively. The recorded signals are drawn in black. The source wavelet and the corrected wavelets are given in blue and red, respectively. In the absence of the cloud only the density effect is important, while in the presence of the cloud the signal is also altered by its transmission at the cloud boundary. The remaining differences between the corrected and recorded signals can be attributed to interference effects inside the cloud.

3.2.5 Discussion

The conditions explored in this study demonstrate the alteration of infrasound signals in the presence of volcanic clouds. High-velocity cloud movement leads to Doppler shifting, and thus to a modification of the signal spectral content. Differences in cloud temperature and ash-loading result in differences in cloud density and speed of sound, which in turn influence the signal amplitude characteristics via density, transmission and interference effects. All these factors cause different signal signatures already at local source distances as shown by the numerical approach. This is contrary to the usual assumption of no path effects in the direct volcanic environment. However, the presented findings only hold for regular infrasound signals generated inside a volcanic cloud. The given model setup neither allows for shock waves nor for waves propagating ahead of the cloud.

Still the results have several implications for the interpretation of volcanic infrasound signals. These signals are usually thought to originate from a non-stationary

volumetric flux of material displacing the surrounding atmosphere. The induced atmospheric displacement normally consists of a marked compression phase followed by a long-lasting decompression stage. Since the time scale of this decompression stage is large compared to the one of cloud propagation, only the onset of the related signal should be unaltered whereas the remaining part of the signal is subject to the effects explored in this study. As a consequence, different signal signatures in terms of peak-to-peak amplitude, frequency content, signal envelope and coda properties are likely. Therefore, parameters based on the pressure trace as a whole, like the acoustic energy or the acoustic power, require a careful interpretation. As shown in figure 3.18 conventional acoustic energy calculation may lead to false estimates. The presented values, however, can be regarded as upper limits given that they exclude any information propagating ahead of the cloud. Still they suggest that evaluation of acoustic energy is most reliable under similar atmospheric conditions rendering energy comparison between different sources and volcanoes a challenging task.
In view of the shown signal alteration, comprehension of the local propagation setting is even more required when studying a volcanic system in detail. Variable propagation conditions should be considered in the analysis of syn-eruptive processes like mass flux fluctuations or resonance effects. Moreover, changing signal signatures could arise from changes in the propagation medium alone. This may lead to ambiguities when interpreting source physical motion from raw waveforms. A proper knowledge of the propagation setting is of particular importance when assessing source physics from infrasound observations.

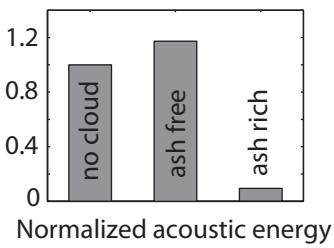

Figure 3.18: Normalized acoustic energy resulting from all three model scenarios shown in figure 3.14. The acoustic energy was calculated based on the formula given in *Johnson* (2003), and is given relative to the reference scenario. Due to the different amplitude characteristics the energy is overestimated in the ash-free and underestimated in the ash-rich case by a factor of 1.2 and 0.1, respectively.

Real data recorded at Yasur in figure 3.19 substantiate this argument. Without information on near-source conditions it would be common to relate the shown infrasonic waveforms to contrasting source dynamics. This is, however, at odds with Doppler radar observations which suggest similar explosion dynamics in terms of

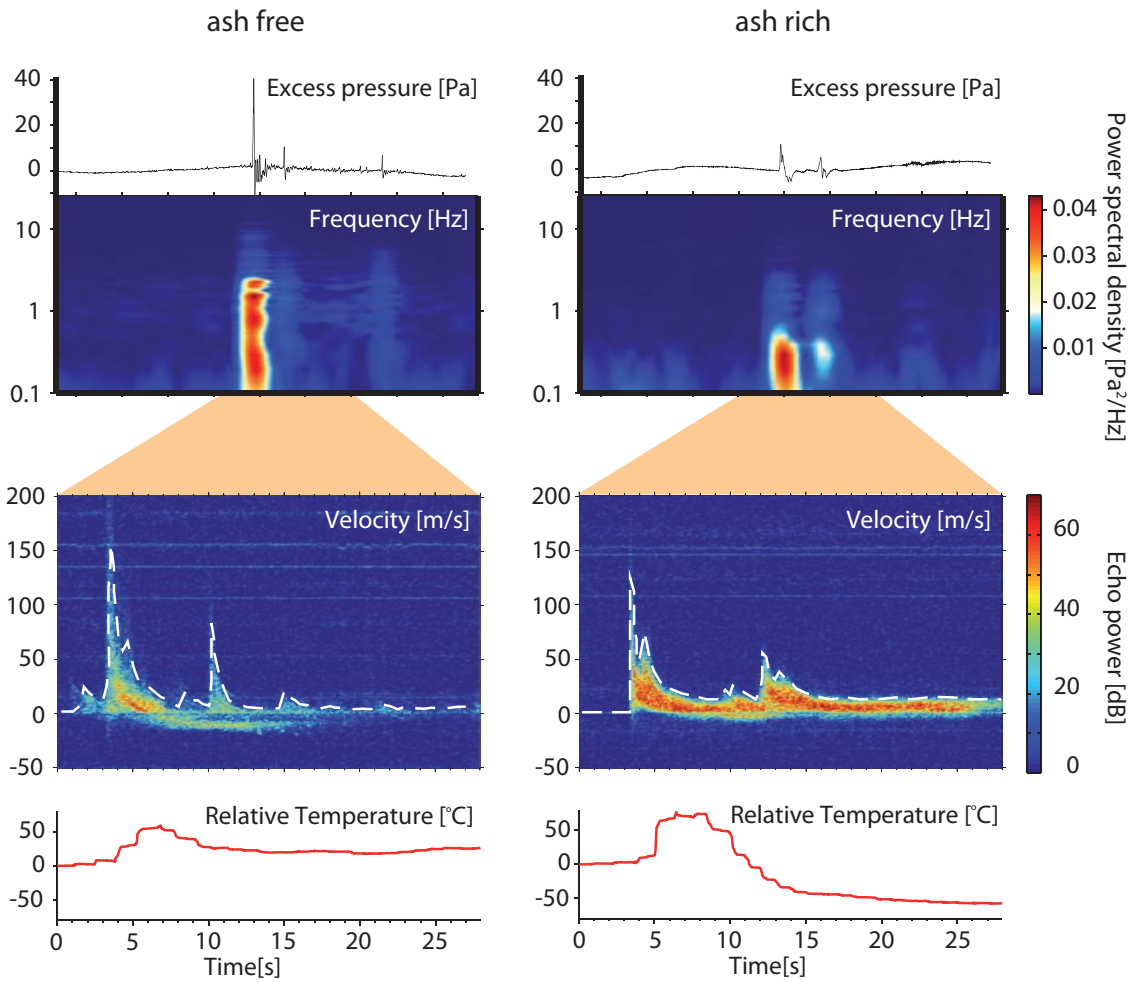

Figure 3.19: Data example of infrasound signals, Doppler radar spectra and relative infrared camera temperatures recorded during ash-free and ash-rich explosions at Yasur. Infrasound timelines in the upper part of the figure have a length of 95 seconds, and are shown along with their corresponding frequency content. The radar and infrared data are displayed in a zoomed perspective on the actual explosion. For the sake of comparison the same scaling is applied to all data sets. In terms of infrasound signals high amplitudes and high frequencies are related to ash-free activity, whereas low amplitudes and low frequencies accompany ash-rich explosions. Doppler radar data indicate that the maximum velocities of explosions (dashed white lines) are of the same order of magnitude. Recorded echo powers give valuable information about the near-source conditions in terms of ash content. During ash cloud movement more energy is scattered back by the eruptive cloud. This is in line with thermal observations. Ash inside the field of view of the infrared camera causes a decrease in relative temperature, i.e. temperature values decrease below initial values found before an explosion. The cooling ash cloud is opaque and masks the vent.

velocity. The presence of propagation effects could help to resolve this conflict. As described in figure 3.19 radar echo powers and thermal data indicate different near-source conditions in terms of ash-load. In the presence of path effects these different conditions would cause signal alteration. We therefore excluded potential path effects using the findings from section 3.2.4. When we account for density and transmission effects and correct the respective excess pressures of 40 and 10 Pa we find identical pressures of about 15 Pa in both cases. Back-calculation of frequency shifts via equation 3.9 transforms the recorded peak frequencies of 2 and 0.6 Hz to 1.4 and 0.5 Hz, respectively. These calculations demonstrate that part of the signal signatures may result from changes in the propagation medium. However, it is important to note that the actual presence of path effects clearly depends on the location of the infrasonic source. Due to the probable mingling of path and source effects in real data scenarios it is impossible to draw an exclusive conclusion. Nevertheless, this example suggests that an explicit assessment of pressures and frequencies as well as the interpretation of raw waveforms must be handled with care when in doubt about source location.

3.2.6 Conclusion

To investigate the alteration of infrasound signals in the presence of volcanic clouds we modeled wave propagation in temporally changing media. In order to quantify potential path effects we compared three end-member scenarios under equal initial conditions. The comparison reveals that different signal signatures result from wave propagation given standard atmospheric conditions, a fast-moving hot gas cloud or a slow-moving cold gas-ash mixture. The hot gas cloud scenario is characterized by a shift to higher signal frequencies. Comparing the signal amplitudes we note a clear attenuation of the waveform in the presence of the gas-ash mixture. The analysis of these observations indicates that high-velocity cloud movement causes Doppler shifting, and that the arising impedance contrasts control the signal amplitude characteristics via density, transmission and interference effects. All these factors are shown to be significant already at local source distances, and may cause different signal signatures in terms of peak-to-peak amplitude, frequency content, signal envelope and coda properties. This bears important implications for the interpretation of volcanic infrasound signals, and for precise source modeling in particular. Whenever infrasonic sources are located in volcanic clouds it is critical to consider the local propagation setting. This study is a first step toward a better understanding of how changing near-source conditions affect local infrasound recordings.

Chapter 4

Surface Activity Variability

To unravel the emergence of Yasur's different explosive styles in this chapter I investigate the temporal link between variations in surface activity and degassing behavior. For this purpose I follow a statistical approach. To quantify degassing behavior I characterize explosive activity in terms of explosion rate and use magnitude groups to specify explosion intensity. Compared to all other data types the infrasound event catalog appears most complete and forms the basis of the analysis. Akin to the general correlation between explosive style and explosion intensity, there is a general correlation between explosion number and explosion magnitude. High explosion numbers coincide with high-magnitude ash-free activity, whereas low explosion numbers are present during low-magnitude ash-rich episodes. A detailed analysis of explosion magnitudes and inter-explosion times demonstrates that explosive activity features power-law statistics. Changes in these statistics result from changes in degassing behavior and correlate with changes in surface activity. The examination of the related temporal dynamics exposes time-correlation structures on all time scales. An analog study of long term Doppler radar data recorded at Stromboli yields similar results. To explain these findings I propose a new model for active degassing at Strombolian volcanoes.

4.1 Temporal Variability of Normal Strombolian Activity at Yasur Volcano, Vanuatu

4.1.1 Abstract

Owing to its frequent activity Yasur volcano, Vanuatu, offers ideal conditions to improve our current understanding of normal Strombolian behavior. Here, we inves-

tigate the temporal variability of explosive degassing in the context of ash-free and ash-rich surface activity. For this purpose we exploit a continuous multi-parameter data set which we recorded during 15 days in 2008. By combination of different statistical methods we capture explosive gas release from Doppler radar, infrasound and seismic data. We analyze degassing behavior in terms of explosion rate and intensity as well as in terms of return time. Likewise we investigate the temporal structure of explosive gas release. Our analysis reveals a clear link between explosive degassing and surface activity. It moreover shows that explosive degassing is overall scale-invariant. Explosion magnitudes and return times feature power-law statistics. Variations in these statistics result from waxing and waining phases in degassing behavior and correlate with changes in surface activity. The power-law character of the temporal structure of explosive gas release further suggests that temporal fluctuations in degassing are correlated in time. The combination of these findings indicates that normal Strombolian activity is neither random nor stationary. Doppler radar measurements at Stromboli volcano support this idea. This is at odds with the common notions of normal Strombolian activity. We therefore propose a new model for active degassing at Strombolian volcanoes.

4.1.2 Introduction

At Strombolian volcanoes variations in explosive style or in activity level bear important information to understand the mechanisms that drive activity. It is well-known that changes in degassing behavior relate to variable gas flux within the conduit and can be used to track changes in magma supply (e.g. *Harris and Ripepe*, 2007a; *Ripepe et al.*, 2008). To asses variations in activity it is common to quantify differences in degassing rate and intensity via geophysical data (*Ripepe et al.*, 2002, 2004, 2005a; *Delle Donne et al.*, 2006; *Ripepe et al.*, 2009; *Spampinato et al.*, 2012). Infrasonic and thermal monitoring, for instance, showed that changes in event number and maximum excess pressure characterize the transition from effusive to normal activity at Stromboli volcano, Italy (*Ripepe et al.*, 2005b, 2007). In addition, detailed analysis of infrasonic amplitude distributions during normal Strombolian activity illustrated a direct link between explosive degassing and magma vesiculation (*Colò et al.*, 2010).

A complemental means to study volcanic activity is to investigate its return time (*Marzocchi and Bebbington*, 2012, and references therein). Although this technique is well-established in probabilistic eruption forecasting, it is rarely used to examine degassing behavior. At Stromboli volcano it was first applied by *Settle and McGetchin* (1980). Based on the return time distribution of 399 Strombolian explosions these authors inferred that Strombolian activity must be triggered by a random process. This is in line with later studies investigating the occurrence of Strombolian

explosion-quakes (*Bottiglieri et al.*, 2005; *De Lauro et al.*, 2009; *De Martino et al.*, 2011a,b). During normal activity inter-quake times follow an exponential distribution indicative of random explosion occurrence. The prevalence of this behavior over several months led to the perception of normal activity as a stationary phenomenon. This is however at odds with short-term changes in explosive style or degassing behavior (e.g. *Patrick et al.*, 2007; *Lautze and Houghton*, 2007; *Ripepe et al.*, 2008). The temporal structure in the sequence of Strombolian explosion-quakes further enforces this conflict. According to *Jaquet and Carniel* (2001) normal Strombolian activity exposes significant time-correlation which argues against the random occurrence of explosions. Conclusions from classical statistical methods that neglect temporal correlation should therefore be taken with care. Furthermore, it is still unclear whether each Strombolian explosion possess a seismic counterpart (*Carniel and Iacop*, 1996). This represents a serious drawback in previous investigations of normal activity.

To revisit earlier findings without the above mentioned problems, in this study we investigate the dynamics of normal Strombolian activity from a surface perspective. For this purpose we exploit a continuous multi-parameter data set of about 58000 Strombolian explosions recorded at Yasur volcano, Vanuatu. The data set provides an excellent basis to study the dynamics of normal Strombolian behavior as it exhibits different types of normal activity, namely ash-free and ash-rich activity. Here, we explore these differences mainly via Doppler radar and infrasound data. We quantify degassing behavior in terms of explosion rate and intensity as well as in terms of return time. Based on these data we show a link between variations in surface activity and degassing behavior. While ash-free activity relates to enhanced degassing, i.e. overall higher explosion numbers and magnitudes, ash-rich activity is characterized by less frequent explosions of lower intensity. In-depth analysis of explosion magnitudes and return times further demonstrates that degassing behavior features power-law statistics. Changes in these statistics correlate with changes in surface activity. Examination of the related temporal dynamics moreover exposes time-correlation structures on all time scales. The combination of these findings bears important implications for previous work, but also for the current paradigm of normal Strombolian activity. Common models fail to explain all observations. We therefore discuss a new model for active degassing at Strombolian volcanoes.

4.1.3 Background

Normal Strombolian Activity

Normal Strombolian activity, common at basaltic volcanoes, is characterized by intermittent, explosive gas release of mild to moderate vigor alongside permanent, quiescent passive degassing. Explosive gas release consists of regular explosions which are thought to originate from the bursting of individual gas slugs at the magma free surface (e.g. *Chouet et al.*, 1974; *Blackburn et al.*, 1976; *Ripepe et al.*, 1993; *Vergniolle and Brandeis*, 1996; *Harris and Ripepe*, 2007a, and references therein). Depending on explosion vigor there are two forms of explosive gas release: (1) puffing activity, where the repeated bursting of a continuous stream of small gas slugs releases gas in discrete packages, so that the emitted gas plume shows a distinct puffing behavior (*Ripepe et al.*, 1996; *Ripepe and Gordeev*, 1999; *Ripepe et al.*, 2002; *Harris and Ripepe*, 2007b); this form of gas release usually excludes the ejection of pyroclasts, and (2) Strombolian explosions, where the vigorous bursting of large, conduit-filling gas slugs causes sustained liberation of gas accompanied by the ejection of pyroclastic material (e.g. *Chouet et al.*, 1974; *Blackburn et al.*, 1976; *Vergniolle et al.*, 1996; *Burton et al.*, 2007a). Subject to the grain size of the ejected material explosions can further be divided into ash-free and ash-rich subtypes (*Chouet et al.*, 1999; *Ripepe and Marchetti*, 2002; *Patrick et al.*, 2007).

Long-standing research has helped to link the particular modes of gas release to different mechanisms of gas segregation, i.e. to how the exsolved gas separates from the melt (*Parfitt*, 2004; *Houghton and Gonnermann*, 2008; *Namiki and Manga*, 2008, compare chapter 1). While explosive gas release is mainly driven by gas overpressure, passive gas emissions relate to equilibrium pressure open-system degassing (*Allard et al.*, 1994; *Burton et al.*, 2007b; *Polacci et al.*, 2008). According to *Burton et al.* (2007b) continuous vesiculation drives the ascending magma towards the percolation transition above which it becomes permeable to gas flow. The evolution from closed- to open-system conditions thus allows passive gas escape without the eruption of magma, and the remaining degassed magma sinks back within the conduit. In this way permanent degassing is sustained via efficient magma circulation of ascending vesiculating and descending degassed magma (*Kazahaya et al.*, 1994; *Stevenson and Blake*, 1998; *Palma et al.*, 2011).
Explosive gas release, in contrast, is independent of magma circulation. It is widely agreed that gas slugs form by coalescence of smaller bubbles at depth, and rise separately from, and faster than the surrounding magma (e.g. *Vergniolle and Jaupart*, 1986; *Parfitt and Wilson*, 1995; *Burton et al.*, 2007a). However, the actual mechanism of slug genesis is still a matter of debate. As summarized by *Parfitt* (2004) two

models are in current usage. The first involves the accumulation of small bubbles in form of a foam layer at fixed geometrical discontinuities within the plumbing system. On reaching a critical thickness the foam layer collapses, and forms a gas slug which subsequently travels up the conduit (*Jaupart and Vergniolle*, 1988, 1989). The second model incorporates bubbles of many sizes which exhibit different ascent velocities due to their difference in size. Differential ascent velocity allows larger bubbles to coalesce with smaller ones leading to formation of a slug which ascends towards the surface (*Wilson and Head*, 1981; *Parfitt and Wilson*, 1995).

Irrespective of the model, investigations of the gas phase released during explosive activity suggest that slugs must rise as a separate phase under non-equilibrium pressure conditions. Gas compositions measured during small and large explosions at Stromboli volcano, Italy, correspond to those achieved by the equilibrium gas phase at ∼0.8 km and ∼2.7 km below the vent (*Burton et al.*, 2007a). Viscous and inertial forces are believed to hamper slug expansion upon ascent, and thus pressure equilibration (*Sparks*, 1978; *Prousevitch et al.*, 1993; *James et al.*, 2008, 2009). As a consequence gas slugs arrive at the magma free-surface with a certain amount of overpressure before bursting, as witnessed by their powerful explosions (*Gerst et al.*, 2013). Explosion vigor is mainly controlled by gas overpressure, and combination of analytical, numerical and laboratory evidence has helped to relate measurable burst effects and gas overpressure. For energetic activity of a particular system the magnitude of the measurable effects of overpressure, e.g. infrasonic signals and ejecta velocities, were shown to be proportional to the square root of the gas mass involved (*James et al.*, 2009).

The qualitative analysis of different regimes of 'burst vigor' furthermore strengthens the hypothesis that puffing activity and Strombolian explosions relate to the same degassing mechanism (*James et al.*, 2009). This is in line with field observations at Stromboli volcano, where the coupling between the rate of puffing and explosions is explained as a common response to the same magma degassing dynamics (*Ripepe et al.*, 2002; *Harris and Ripepe*, 2007b; *Ripepe et al.*, 2008). Correlated changes in scoria vesiculation, and the rate and energy of explosive activity moreover provide evidence for the interplay between vesiculation processes and explosive gas release (*Colò et al.*, 2010). While an increased volatile content in the magma column leads to elevated explosive degassing in terms of explosion vigor and frequency, lowered explosive gas release mirrors the presence of gas poor magma (*Ripepe et al.*, 2002, 2008). Reduced magma discharge is thought to promote magma maturation in the upper conduit involving changes in magma rheology. These may feed back to enhance fragmentation efficiency, and hence the ash load of explosions, determining the style of normal activity (*Lautze and Houghton*, 2005, 2007; *Taddeucci et al.*, 2002, 2004; *Andronico et al.*, 2009).

Volcanic Activity at Yasur

Yasur volcano is one of the most active volcanoes of Vanuatu volcanic arc (*Bani et al.*, 2012), which defines the convergent margin between the Australian plate and the spreading North Fiji basin (*Auzende et al.*, 1995; *Calmant et al.*, 2003). It is the youngest of a group of Holocene volcanic centers constructed over the down-dropped flank of the Pleistocene Tukosmeru volcano in the south-eastern part of Tanna island (*Carnay and MacFarlane*, 1979; *Nairn et al.*, 1988; *Robin et al.*, 1994). Mt. Yasur started to form about 1400 years ago, when eruptive activity began to focus at the western edge of the Yenkahe horst in the Siwi caldera (*Métrich et al.*, 2011). The actual growth of the presently active Yasur cone can be traced back to about 800 years ago (*Nairn et al.*, 1988). It has been considered as continuously active since its first sighting by Captain Cook in 1774, with a recent period of high activity since 1994 (*Simkin and Siebert*, 1994). Long term measurements of SO_2 emission rates however indicate strong variations in activity level (*Bani and Lardy*, 2007). Today Mt. Yasur rises 379 m above sea level and has a nearly circular 400-m-wide summit crater (*Nairn et al.*, 1988; *Oppenheimer et al.*, 2006). Volcanic gases are released from three active vents named A, B and C. Normal activity consists of sustained degassing along with explosions of Strombolian to mild-Vulcanian vigor (*Simkin and Siebert*, 1994). Explosions occur on average 1-3 times per minute erupting magma of basalt-trachyandesitic composition (*Métrich et al.*, 2011). Seismic signatures caused by explosions are similar to those found at Stromboli volcano pointing to a similar causative mechanism (*Nabyl et al.*, 1997). Differences in gas composition between explosive and passive gas emissions corroborate this idea (*Oppenheimer et al.*, 2006). Like at Stromboli, deep volatile exsolution drives explosive activity and bursting of pressurized gas slugs is thought to cause explosions at the magma free surface.

4.1.4 Data Basis

Throughout our 15-days field campaign, in August/September 2008, surface activity at Yasur was normal with sometimes several explosions per minute. Vent A was clearly most active, and direct observations of its exit showed permanent degassing and recurrent Strombolian explosions. Daily visual monitoring indicated a prominent transition in explosive style from ash-rich to ash-free explosions followed by a phase of high ash discharge. This was followed by a transitional phase during which activity evolved back towards nearly ash-free explosions. Observed explosion styles were similar to those found at Stromboli volcano, and consistent with changes in explosion intensity. Temporal tracking of surface activity moreover revealed the

regime-like persistence of a given explosive style through time (see *Meier et al.*, 2014b, chapter 3). In the following we will use the term 'ash-free', 'ash-rich' and 'transitional' to mark the respective episodes.

Data Acquisition

To measure activity at Yasur we installed two Doppler radars, one infrared camera, thirteen infrasound sensors as well sixteen seismic stations on and around the volcano. In detail we used: (1) one high- and one low-resolution 24 GHz frequency modulated continuous wave Doppler radar produced by Metek, (2) one 320 $\times$ 240 TVS-700 infrared (8 - 14 μm) camera produced by NEC-Avio, (3) twelve band-limited (0.05 - 5 Hz) SensorTechnics 144SM350D-PCB microphones plus one Martec MB2005 broadband (0.03 - 10 Hz) microbarometer, and (4) twelve short period (1 s) Mark L4C seismometers along with four long period (120 s) Streckeisen STS-2 seismometers. Time synchronization of all sensors was obtained using GPS receivers. Data were continuously recorded via five monitoring clusters at a sampling frequency of 25 Hz and 100 Hz for sensor group (1, 2) and (3, 4), respectively.

To monitor surface activity at vent A the first cluster was setup at the crater rim. It incorporated both Doppler radars, the infrared camera, one short period seismometer and two infrasound arrays of three sensors each. It was extended by a second monitoring cluster situated partly on the flanks of the volcano in the south-east. Here we deployed the microbarometer along with three short period and one broadband seismic station. Within the realm of possibilities this layout was most appropriate to record the broadband infrasonic signature related to explosions. The remaining three clusters were placed in the ash-plane north-west of the volcano. They were composed of one broadband seismometer and two or three short period seismic stations. In addition, we co-located two infrasound arrays with the broadband seismometers of the two larger clusters. This was necessary for a reliable assignment of acoustic signals to each vent. Further details on data acquisition can be found in (see *Meier et al.*, 2014b, chapter 3).

Event Catalog Creation

In order to characterize explosive activity at Yasur we created an event catalog for each data set. For this purpose we used different methods in accordance with each data type. Here, we describe these methods for Doppler radar, infrasound and seismic observations. A detailed analysis of infrared recordings is excluded from this work. Given the amount of data of $\sim 2 \times 10^6$ frames it was impossible to index each

event. However, it is worth noting that the overall temporal trend in thermal recordings clearly supports the observed variations in explosive style. Exemplary analysis of one arbitrary explosion per hour confirms visual observations from the field as well as the persistence of a given explosive style through time (for details, see *Meier et al.*, 2014b, chapter 3).

To identify explosive events recorded by Doppler radar we screened the velocity information contained in the data set. An event was declared once the velocity exceeded 10 m/s until returning to values smaller than 5 m/s. Based on these values we performed a simple threshold search to catalog all events. Event extraction was cross-checked via hand-picked data and successful in all cases. To gather information on explosion intensity the maximum velocity of each event was then determined (for details on this procedure, see *Scharff et al.*, 2012). In this context it is important to mention that the low-resolution Doppler radar replaced the high-resolution instrument on measurement day ten two twelve. This shifted the unambiguous velocity from 202 m/s to 50 m/s. As a consequence the cataloged explosion velocities are clipped during this period.

To detect infrasound events sourced at vent A we followed two different approaches after bandpass filtering all data from 0.1 to 20 Hz. First, we used theoretical travel times to the vent to delay all infrasound traces. Subsequently, traces from all short period sensors were summed and compared to the trace of the broadband station based on their coherence. An event was declared once the coherence and pressure exceeded 0.85 and 0.1 Pa, respectively. Based on this information the true event onset at the broadband station was then picked by selecting the maximum pressure and its corresponding time on the raw acoustic records. This time and maximum pressure built up the first event catalog.
The second approach consisted in simple STA/LTA detection on the delayed-and-summed trace of all infrasound stations. To declare events we chose a STA-window of 3 s length, a LTA-window of 9 s length and a critical threshold of 0.45. Once an event was detected, we determined its true onset time and maximum pressure measured at the crater rim. For this purpose we applied the same picking procedure as in the first approach to one infrasonic trace recorded at the rim. The so-selected time and respective maximum pressure then made up the second event catalog. Please note that both event catalogs were cross-checked at random against raw acoustic traces to optimize event extraction. Parameters were chosen to warrant the extraction of large but also of small events. This led to a trade-off between signal and noise which had to be handled in both approaches. The final parameter choice reported above prevented noise extraction in any case. As a result small events may be partly missing.

To extract events from seismic observations we focused on all broadband seismic recordings. Events were detected via a standard STA/LTA approach and an event was declared when detected at all stations. Based on the detected event time the true event onset was then picked in the same way as for infrasound data. To this end we selected the maximum seismic amplitude and its corresponding time on the raw seismic trace recorded at the broadband seismic station located south-east of the volcano. The so-selected time and seismic amplitude then formed the event catalog. As for infrasound data it was cross-checked at random against raw seismic records to tune event detection. A STA-window of 5 s length, a LTA-window of 30 s length and a critical threshold of 0.18 were most suitable to pick explosions quakes. Due to their prominent high frequency signature best results were achieved after high pass filtering all data above 0.1 Hz.

4.1.5 Level of Activity

To study explosive activity we combined several methods. At first, we assessed the level of activity to investigate the link between observed variations in surface activity and degassing behavior. For this purpose we quantified explosive degassing in terms of explosion rate and used magnitude groups to specify explosion intensity. Based on this data we then examined the general degassing history and analyzed the coupling between puffing and explosions.

Explosion Rate

To quantify explosion rate we calculated the number of events per hour contained in each event catalog. Figure 4.1 presents the resulting counts related to each data set. There are clear differences with regard to data type. While the number of seismic events is constant as demonstrated by the white line, the number of Doppler radar and infrasound events marked in blue, magenta/green shows strong variations. Furthermore, there is a disparity regarding the overall number of events. The seismic event catalog yields an explosion rate of about 100 explosions per hour. In contrast, the number of events detected by Doppler radar ranges between 100 and 650 per hour. Explosion rates derived from infrasound data further surpass these numbers. The first and second infrasound catalog exhibit maximum counts of 3000 and 2000 events per hour, respectively.

The differences in explosion rate can be explained by the degree of detail provided by each data set. Infrasound data furnish the most detailed measure of overall degassing behavior as they directly map the excess pressure of explosive gas release. All types of explosive gas release, i.e. puffing and Strombolian explosions, are equally

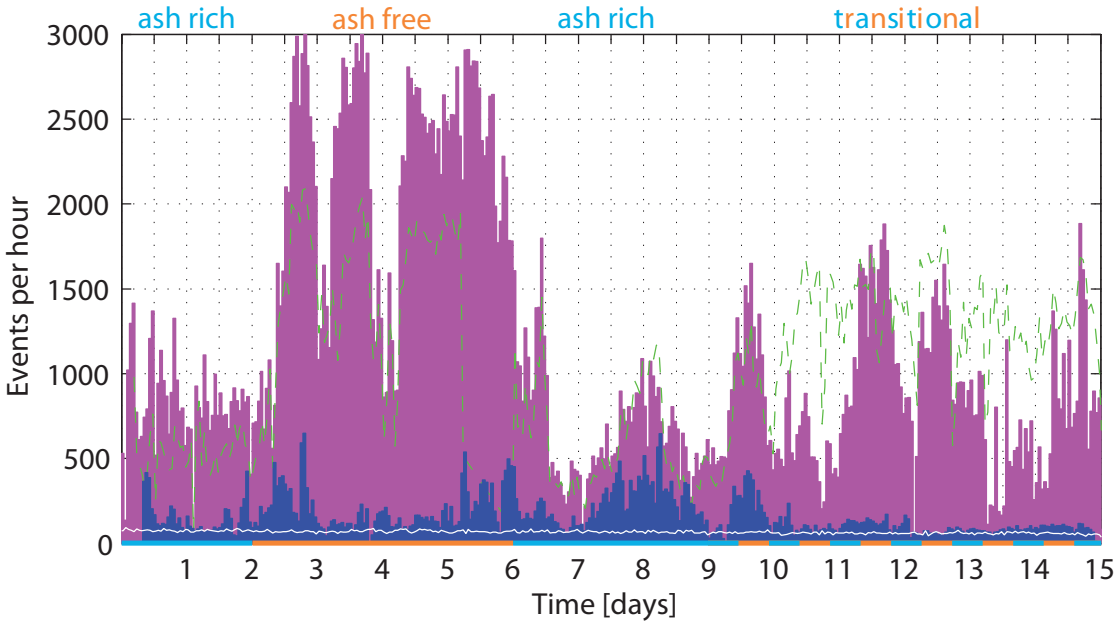

Figure 4.1: Number of events per hour as detected in Doppler radar, infrasound, and seismic data. Annotations on the x-axis mark the end of each measurement day. The different forms of surface activity are specified in blue and orange on top of the figure. Bars at the bottom of the figure indicate their duration. Doppler radar events are given in blue, while events from the first infrasound catalog are shown in magenta. Infrasound events from the second catalog and seismic events are depicted by the green dashed and continuous white line, respectively. Both infrasound catalogs appear most complete, and the temporal trend in event number is independent of detection approach until end of day ten. Low event numbers characterize ash-rich activity, whereas high event numbers are present in the ash-free regime. During the transitional phase STA/LTA detection of infrasound events yields higher event numbers than the coherence approach on day eleven and fourteen.

recorded independent of their intensity. Yet indexing of events is subject to detection approach. Detection based on coherence is in general more accurate as small transients are more reliably spotted via their coherence. Inspection of absolute event numbers demonstrates this effect. The first infrasound catalog features a greater number of events than the second one with minor exceptions. In these cases a change in wind direction may have caused smearing of the delayed-and-summed trace of all short period sensors, and thus a decrease in coherence. Nevertheless, the first infrasound catalog gives the most exhaustive description of explosive gas release.
Doppler radar data, on the contrary, offer less detail. Due to the fact that the speed of moving material is registered simple gas puffs are not detected, and degassing behavior is only imaged in terms of Strombolian explosions.
Seismic recordings bear even greater limitations. Comparison of all data types showed that low-intensity surface activity phenomena like small explosions or puffing

mostly lack ground movement at our broadband seismic stations. As a consequence the related events are not cataloged. Besides that, the relation between explosion quakes and surface activity is ambiguous. Several explosions quakes were missing a surface manifestation in terms of Doppler radar and/or infrasound data. We therefore discarded the seismic event catalog to investigate the general degassing history.

Instead we focused on the first infrasound event catalog to analyze degassing behavior. In the following we mainly consider observations until end of day ten. The reasons for this are twofold. First, the temporal trend in event number is independent of detection approach during this period, and can be considered as an actual trend. Second, changes in surface activity were well-defined. Ash-free activity was observed on days three to six, whereas ash-rich activity was observed on days one and two, and days seven to ten. The selected period thus offers ideal conditions to study the link between variations in surface activity and degassing behavior.

Figure 4.1 shows first evidence for the existence of this link. Explosion rates derived from infrasound clearly correlate with variations in surface activity. While low explosion rates coincide with ash-rich activity, high explosion rates characterize ash-free episodes. Given the number of Strombolian explosions detected by Doppler radar, variations in explosion rate are mainly driven by variations in puffing.

Magnitude of Explosions

In order to complement these observations, we additionally tracked the level of activity in terms of explosion intensity. To this end we evaluated the maximum Doppler velocity, maximum excess pressure and maximum seismic amplitude of each cataloged event. To facilitate the comparison between data types we classified the respective information in ten magnitude classes. For the sake of consistency we chose a simple logarithmic classification scheme for all data types. Details on the resulting Doppler velocity and excess pressure classes are reported in table 4.1. The respective temporal distribution of explosion magnitudes is shown in figures 4.2 and 4.3. Magnitudes derived from seismic data are not presented as they provide no further information. The amplitude of explosion quakes mirrors the temporal trend in Doppler velocities and excess pressure.

As demonstrated in figures 4.2 and 4.3 the temporal trend in explosion magnitude is independent of data type. Variations in magnitude are consistently mapped in terms of Doppler velocity and excess pressure. However, there are relative differences between reported magnitudes. These differences relate again to the degree of detail provided by each data type. Unlike the Doppler radar event catalog, the

Magnitude	Doppler velocity range [m/s]		Excess pressure range [Pa]	
1	10.08	13.60	0.10	0.21
2	13.60	18.35	0.21	0.43
3	18.35	24.76	0.43	0.88
4	24.76	33.40	0.88	1.82
5	33.40	45.06	1.82	3.77
6	45.06	60.80	3.77	7.79
7	60.08	82.03	7.79	16.10
8	82.03	110.67	16.10	33.27
9	110.67	149.31	33.27	68.76
10	149.31	201.45	68.76	142.09

Table 4.1: Summary of Doppler velocity and excess pressure classes used to specify explosion intensity. Magnitude classes are listed together with their respective Doppler velocity and excess pressure range. Doppler velocities were recorded 276 m away from vent A, and were measured along the radar beam. Excess pressures refer to the first infrasound catalog, and were recorded by the broadband microbarometer located 640 m away from the vent.

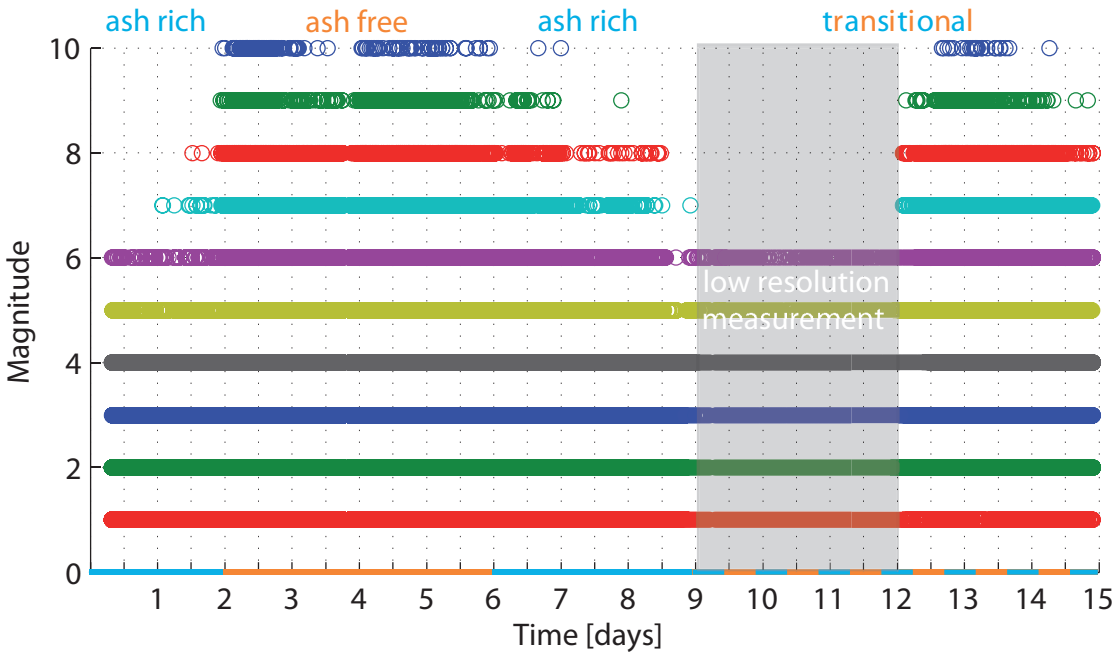

Figure 4.2: Magnitude of events as recorded by Doppler radar. Magnitude classes are color-coded, and annotations on the x-axis equal those in figure 4.1. Different forms of surface activity are again tagged in blue and orange on the top and bottom of the figure. The installation of the low resolution Doppler radar is marked in gray. Owing to the clipping in explosion velocity absolute magnitudes are incomparable during this period. Still a clear waxing and waning in magnitude can be observed. Variations in explosion magnitude coincide with variations in surface activity. While an increase in explosion magnitude indicates the transition to ash-free activity, high explosion magnitudes die our during ash-rich episodes. The trend in magnitude during the transitional phase is in line with the temporary occurrence of ash-free explosions.

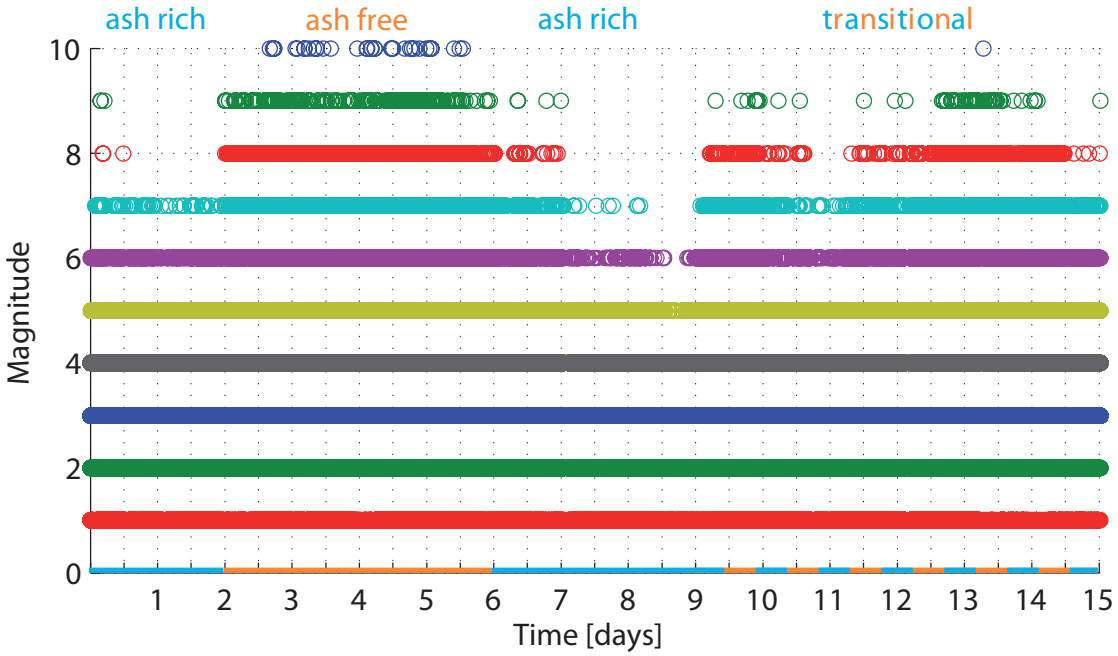

Figure 4.3: Magnitude of events as recorded by infrasound. Magnitude classes are color-coded in the same way as in figure 4.2, and annotations on the x-axis again equal those in figure 4.1. Different forms of surface activity are again denoted in blue and orange. Explosion magnitudes show clear waxing and waining like in figure 4.2, and correlate with variations in surface activity. Low-magnitude explosions are present in all surface activity regimes. High-magnitude explosions mainly occur during ash-free activity, but also during the transitional phase.

infrasound catalog includes puffing events. Thus all types of explosive gas release are included in the magnitude classification scheme. Doppler radar events, on the contrary, represent a 'zoomed-in' perspective on the process of Strombolian explosions. A subset of explosive events is therefore classified in this case. The magnitudes derived from Doppler radar and infrasound are hence unequal. Nonetheless, there is a general correlation between explosion magnitude and variations in surface activity. Low-magnitude explosions occur during all forms of surface activity, whereas high-magnitude explosions emerge during ash-free episodes. Magnitudes of the transitional phase are consistent with the temporary occurrence of ash-free explosions.

With respect to the first infrasound catalog variations in explosion magnitude are further in line with variations explosion rate (shown in figure 4.1). Seeing that the latter mostly indicate variations in puffing, the intensity of explosions increases when puffing is accelerated and vice versa. This suggests that puffing and explosions respond to the same magma degassing dynamics.

Analysis of Magnitude Distribution

As reviewed in the background section the coupling between puffing and explosions is a typical feature of Strombolian degassing behavior. To investigate it in detail we analyzed the infrasonic magnitude distribution from a statistical perspective. For this purpose we first determined the overall number of events contained in each magnitude class. The resulting distribution is presented on the left in figure 4.4 in form of a double-logarithmic plot. For reasons of clarity event numbers are normalized. Magnitudes are distributed according to a power-law as depicted by the green line. Deviations from power-law behavior at small and large magnitudes result from the limited resolution of the infrasound event catalog at low and high pressures. While the low pressure limit is given by the signal/noise boundary, the high pressure limit relates to the finite extent of the data set. The presence of a power-law apart from these limits indicates that the remaining events are driven by a single,

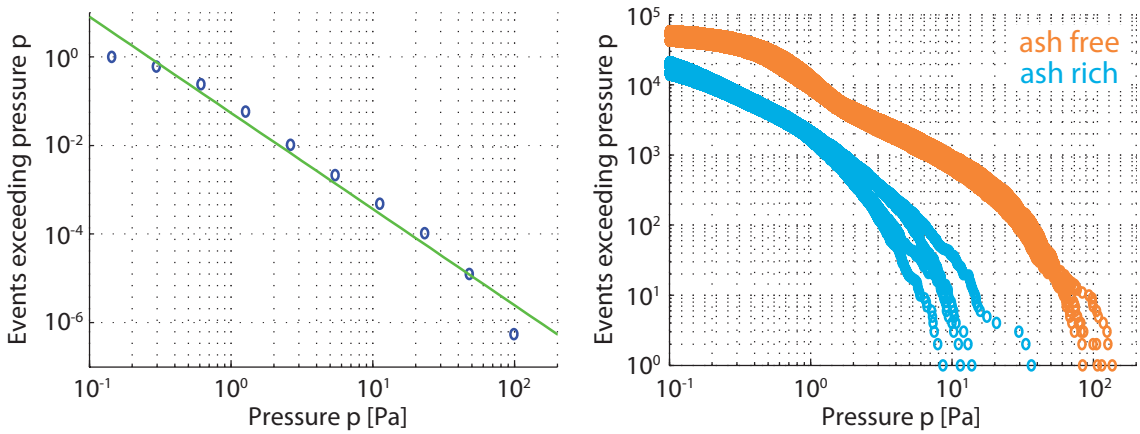

Figure 4.4: Magnitude distribution of events as recorded by infrasound. On the left the magnitude distribution of the entire first event catalog is shown. Magnitude classes are the same as in figure 4.3, and their corresponding pressures are marked on the x-axis. On the y-axis the normalized number of events in each magnitude class is given, and the green line depicts the best power-law fit to the data. A deviation from power-law behavior can be observed at low and high pressures. On the right the cumulative infrasonic amplitude distribution is presented for four ash-free and ash-rich days in orange and blue, respectively. In this part of the figure the y-axis maps the absolute number of events recorded during each day. The shape of the distributions reflects differences in degassing behavior coincident with different forms of activity. High event numbers coincide with high-intensity ash-free activity, whereas low event numbers are present during low-intensity ash-rich episodes. The overall magnitude distribution on the left is a superposition of the different distributions in each activity regime.

scale-invariant process. All forms of explosive gas release must therefore share the same degassing mechanism irrespective of their intensity.

To link this observation to changes in surface activity we followed a similar approach to the one presented in *Colò et al.* (2010). To this end we calculated the cumulative infrasonic amplitude distribution for four ash-free and ash-rich days (days two to nine). The resulting distributions are displayed on the right in figure 4.4 again via a double-logarithmic plot. To demonstrate the differences in event number between ash-free and ash-rich activity the absolute number of events is shown. Qualitative results summarize previous observations. Ash-free activity relates to enhanced explosive degassing in terms of explosion frequency and intensity. High-intensity explosions are present, and the number of small puffing events is elevated. Ash-rich activity, on the contrary, features an overall lower event number along with explosions of lower intensity indicative of reduced explosive gas release. Changes in activity correlate with changes in degassing behavior which modify the underlying power-law statistics in turn.

4.1.6 Temporal Behavior

The analyses of the previous section confirm and improve several results on normal Strombolian behavior. They highlight that puffing and explosions respond to the same magma degassing dynamics (*Ripepe et al.*, 2002; *Harris and Ripepe*, 2007b; *Ripepe et al.*, 2008), and support the hypothesis that all forms of explosive gas release share the same degassing mechanism (*James et al.*, 2009). Moreover, they establish a systematic link between explosive degassing and variations in surface activity. According to earlier studies this link can be explained by changes in magma supply. Enhanced supply of fresh gas-rich magma results in an increased gas flux within the conduit. This leads to elevated explosive gas release as witnessed by vigorous puffing activity and high-intensity ash-free explosions (*Ripepe et al.*, 2002, 2008; *Colò et al.*, 2010). A reduction in magma supply, in contrast, favors magma outgassing. This decreases the volatile content in the magma column as testified by lowered explosive gas release. Reduced magma discharge promotes magma maturation entailing an increase in magma viscosity. Fragmentation becomes more efficient; the ash load of explosion increases (*Lautze and Houghton*, 2005, 2007; *Taddeucci et al.*, 2002, 2004; *Andronico et al.*, 2009).

Irrespective of this interpretation, it is clear that explosive degassing at Yasur cycles through periods of high and low activity. To get a deeper comprehension of the underlying dynamics we therefore studied the temporal behavior of explosive degassing in detail. For this purpose we characterized the sequence of detected events in terms

of a point process, i.e. we dropped any information on event intensity. Based on this representation we then used several measures to analyze temporal behavior. In particular, we combined interval-based and count-based measures as well as measures based on the point process itself (*Lowen and Teich*, 2005, for review). This was necessary to properly map the dynamics of the process in the context of time-correlation structures. In the following we demonstrate this approach on basis of the first infrasound event catalog as the results are well-supported and offer most detail. They parallel results from the second infrasound catalog and are in line with those from Doppler radar observations. Results from seismic data however do not compare due to their limited resolution. The seismic event catalog misses records of various degassing events as explained above. As a consequence we discarded the seismic event catalog to investigate the dynamics of explosive degassing.

Analysis of Return Time

In analogy to other work (e.g. *Settle and McGetchin*, 1980; *Bottiglieri et al.*, 2005; *De Martino et al.*, 2011b,a), at first we used interval-based measures to characterize temporal behavior. For this purpose we followed the same procedure as in *De Lauro et al.* (2009) and examined the time intervals between two successive events. In case of random behavior, their distribution should be exponential indicative of a Poisson process (*Cox and Lewis*, 1966). To test this hypothesis we evaluated the coefficient of variation of the recorded time intervals τ, i.e. $C_v = \sigma_\tau/\mathrm{E}(\tau)$. To this end we calculated their standard deviation σ_τ and their mean $\mathrm{E}(\tau)$ on an hourly basis. The result is shown in figure 4.5. Here, the value for random behavior is given by a red line at $C_v = 1$ owing to the fact that the standard deviation of an exponential distribution is equal to its mean. The actual process shows strong deviations from this behavior. The coefficient of variation is either greater or less than one indicative of clustered or periodic event occurrence. Transitions between these states further coincide with changes in surface activity. Whereas ash-rich activity features clustered event occurrence, ash-free activity exhibits more regular behavior. Observations of the transitional phase only partly demonstrate this trend due to the possible incompleteness of the first infrasound event catalog during this time. In any case it is clear that explosive degassing displays non-random behavior.

To elaborate this finding we analyzed the return time distribution of the recorded time intervals. For the sake of consistency we adopted the same approach as for explosion magnitudes. We ranked the recorded intervals in ten return time classes via a logarithmic classification scheme as summarized in table 4.2. To evaluate their distribution we then determined the number of events contained in each return time class. The resulting distribution is given on the left in figure 4.6. For reasons of

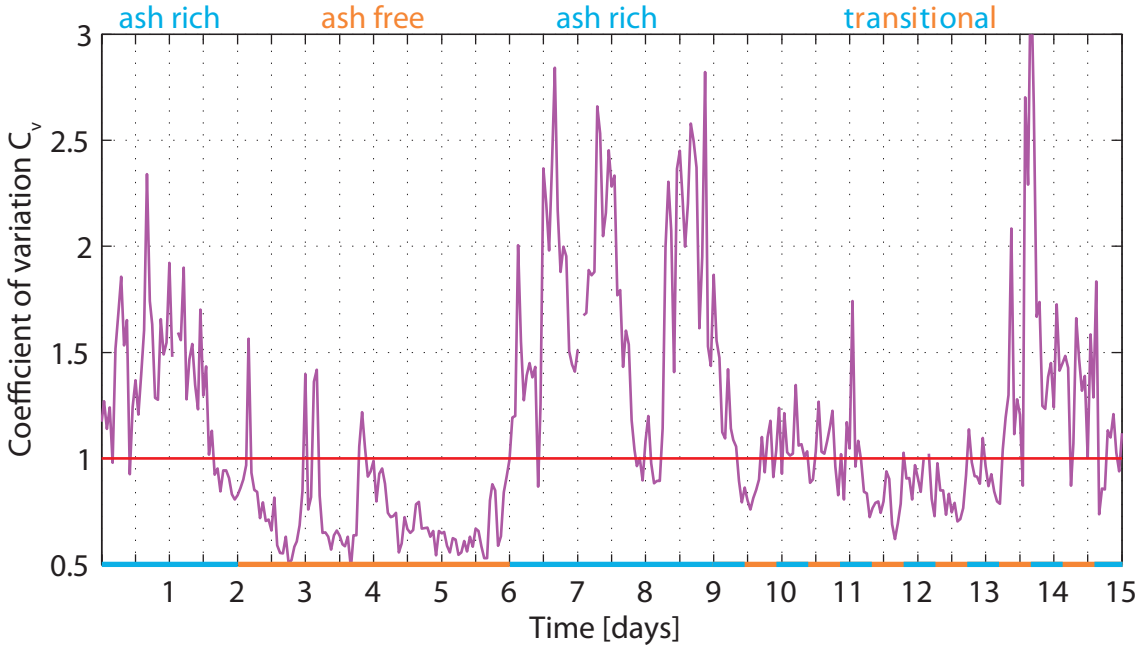

Figure 4.5: Coefficient of variation per hour as recorded by infrasound. Annotations on the x-axis equal those in figure 4.1. Different forms of surface activity are again denoted in blue and orange on the top and bottom of the figure. The coefficient of variation of the recorded time intervals is given in magenta. The red line marks the standard case of a random Poisson process. Compared to the standard case the actual process shows strong deviations. The coefficient of variation is either greater or less than one, and in line with changes in surface activity until end of ten. After this time it exhibits several outliers, which result from the possible incompleteness of the first infrasound event catalog during this time (compare to figure 4.1).

Rank	Return time range [s]	
1	0.50	0.96
2	0.96	1.85
3	1.85	3.55
4	3.55	6.82
5	6.82	13.10
6	13.10	25.18
7	25.18	48.38
8	48.38	92.97
9	92.97	178.65
10	178.65	343.30

Table 4.2: Summary of return time classes used to analyze the return time distribution. The classes are ranked according to their respective return time range.

clarity event numbers are normalized like in figure 4.4. Return times are distributed according to a power-law as shown by the green line. Deviations from this behavior stem again from the limited resolution of the infrasound event catalog. In general, small return times relate to puffing events which are sparsely detected at the signal/noise boundary. Large return times are not fully mapped due to the finite extent of the data set. The presence of a power-law apart from these limits demonstrates that the recurrence of explosive degassing is scale-invariant.

To assess the role of surface activity we calculated the cumulative return time distribution for four ash-free and ash-rich days. For this purpose we used the same days as in figure 4.4. The resulting distributions are displayed on the right in figure 4.6. To highlight the differences between ash-free and ash-rich activity the absolute number of events is presented in this part of the figure. Qualitative results are in line with changes explosion rate shown in figure 4.1. Whereas large return times characterize ash-rich activity, ash-free episodes feature smaller return times. Changes in surface activity relate to changes in explosion rate which entail changes in return time. This alters the underlying power-law statistics as for explosion magnitudes.

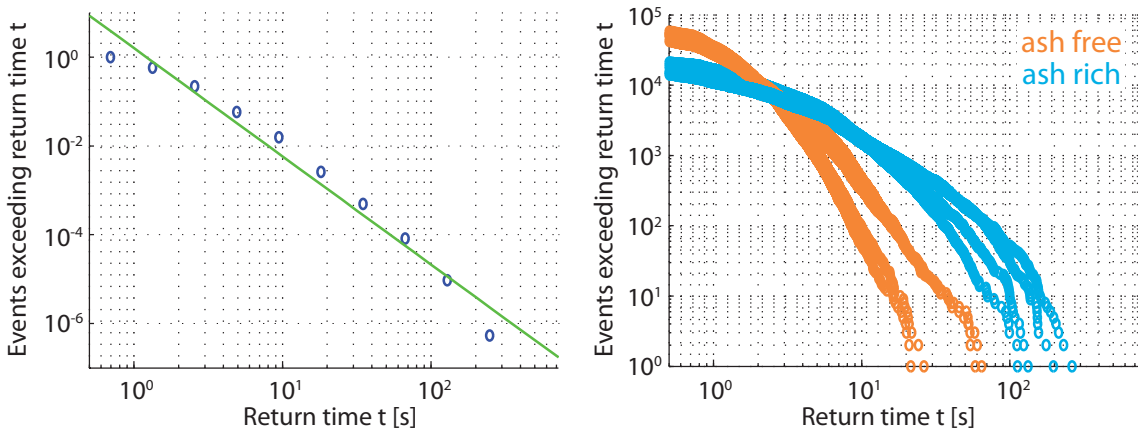

Figure 4.6: Return time distribution of events as recorded by infrasound. On the left the return time distribution of the entire event catalog is presented. Return times are marked on the x-axis which covers a time range between 0.5 seconds and twelve minutes. The y-axis displays the normalized number of events in each return time class, and the green line shows the best power-law fit to the data. At low and high return times there is a deviation from power-law behavior. On the right the cumulative return time distribution is given for four selected ash-free and ash-rich days in orange and blue, respectively. Here, the y-axis indicates the absolute number of events recorded during each day. The shape of the distributions mirrors differences in degassing behavior coincident with different forms of activity. During ash-free activity smaller return times prevail and the number of small return times is elevated. Ash-rich episodes result in opposite conditions. As for explosion magnitudes (figure 4.4) the overall return time distribution on the left is a superposition of the different distributions in each activity regime.

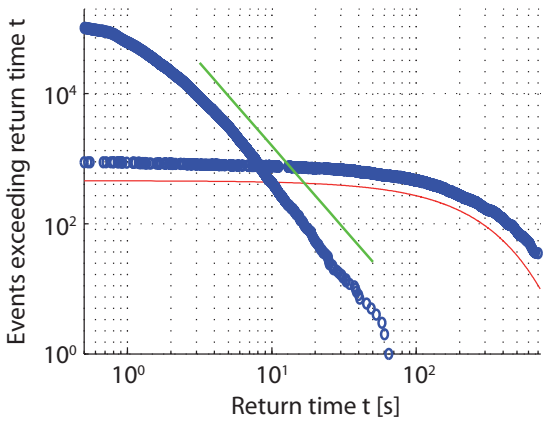

Figure 4.7: Return time distribution of the original event catalog versus the distribution of high-intensity events only as recorded by infrasound during two selected ash-free days. Return times are shown on the x-axis which covers a time range between 0.5 seconds and seventeen minutes. On the y-axis the absolute event number is given to clarify the differences between both cases. Return times of the original event catalog follow a power-law during the selected episode as indicated by the green line. In the case of high-intensity events only, return times become larger and their distribution exhibits exponential behavior as illustrated by the red line.

In order to understand these results it is essential to compare them to other work (*Settle and McGetchin*, 1980; *Bottiglieri et al.*, 2005; *De Lauro et al.*, 2009; *De Martino et al.*, 2011b,a). In this context it is important to note that previous studies were based on visual observations or on seismic data. This implies that low-intensity degassing phenomena like small explosions or puffing were not considered. For the sake of comparison we therefore removed these events from our catalog. To this end we discarded events with a magnitude smaller than seven, i.e. with an excess pressure of less than ∼8 Pa. Based on this data we then recalculated the intervals between two successive events and studied the resulting return times. Despite the same methodology our findings are different in this case. The distribution of return times is exponential. To demonstrate this issue in figure 4.7 we compare the cumulative return time distribution for two ash-free days (days five and six). Return times of the original event catalog follow a power-law as expected. However, when low-intensity events are removed return times are larger and their distribution becomes exponential. Deletion of low-intensity events alters the variability of the process. This causes the resulting process to mimic Poissonian behavior as observed in other work. Yet the variability of the process bears important information on degassing dynamics as shown above. It is thus worthwhile to analyze it in greater detail.

Analysis of Normalized Variance

In general, there are several methods to complete this task. One method that proved to be useful is the analysis of normalized variance, also known as Fano factor analysis (e.g. *Turcott and Teich*, 1996; *Thurner et al.*, 1997; *Lowen and Teich*, 2005). In volcano research it was first applied by *Telesca et al.* (2002) to investigate the temporal dynamics of volcanic activity world wide. Other than interval-based measures, it is based on the sequence of event numbers N_i rather than on the sequence of time intervals τ_i. This makes it a count-based method.
To obtain an event number sequence the time axis is divided into equally spaced contiguous counting time windows of duration T, and the number of events in the ith window is counted. The resulting sequence N_i then forms a discrete-time random counting process. The number of events in figure 4.1 is one example of such a process. An attractive feature of this representation is that the sequence N_i reflects the temporal behavior on the time scale T of the counting window (e.g. one hour in the case of figure 4.1). Varying the length of the counting window thus allows an examination of temporal fluctuations on arbitrary time scales. This is a major advantage compared to interval-based measures where the time scale of information is fixed by the mean inter-event interval of the process under consideration. It offers the possibility to detect temporal correlations by studying the normalized variance:

$$V(T) = \frac{\mathrm{Var}(N_i(T))}{\mathrm{E}(N_i(T))} \tag{4.1}$$

where $\mathrm{Var}(N_i(T))$ is the event number variance normalized by its mean $\mathrm{E}(N_i(T))$. In general, $V(T)$ is a function of counting time T. It indicates the degree of event clustering relative to a Poisson process, for which $V(T) = 1$ for all counting times. For a Poisson process the event number variance is always equal to its mean. Any derivation from unity in the value of $V(T)$ hence evidences non-random behavior. In particular, an excess over unity for a counting time T indicates clustering in the event number sequence at that time scale, while values below unity imply more regular behavior. A power-law dependence of the from $V(T) \sim T^{\alpha}$ is expected in the presence of scale-invariant temporal fluctuations, i.e. in case of global time-correlation.

In order to analyze the normalized variance of the sequence of detected events we followed a two step procedure. At first, we constructed the event number sequence for different counting times. For this purpose we used a time window range between

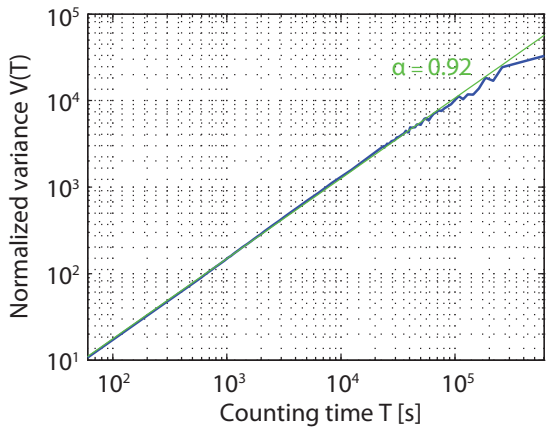

Figure 4.8: Normalized variance of event number sequence as recorded by infrasound. The monotonic increase of variance is well-fitted by a power-law for all counting times as depicted by the green line. The counting time windows range between one minute and seven days.

one minute and seven days. We then calculated the normalized variance for each counting time. The resulting $V(T)$ curve is presented in figure 4.8. There is clear evidence for non-random behavior. The normalized variance increases monotonically with counting time and is well-fitted by a power-law with $\alpha \sim 1$. This power-law increase demonstrates the existence of time-correlation structures on all time scales. In contrast to the standard Poisson process, where the number of recorded events are independent, the number of recorded events are correlated in time. This result is in good agreement with the observed cycles in activity. It moreover argues for the presence of such cycles on arbitrary time scales.

Analysis of Power Spectrum

To corroborate this finding we investigated the power spectrum of the event time sequence itself. The reasons for this are two fold. First, the normalized variance may suffer from bias for counts that exhibit dependence (*Thurner et al.*, 1997; *Lowen and Teich*, 1995). Second, information is lost when transforming a point process to a counting process as the specific occurrence times of events within each counting window are ignored. The power spectrum of the event time sequence does not have this limitation. It furnishes information about the power of the process on all time scales at resolution of the data. In the presence of scale-invariant temporal fluctuations it reads (e.g. *Lowen and Teich*, 2005):

$$S(f) = (\frac{f}{f_s})^{-\alpha} \tag{4.2}$$

where the exponent α characterizes the relative strength of the fluctuations at different frequencies or times as for the normalized variance, and f_s is a multiplicative constant indicating their absolute strength. As for the normalized variance $\alpha = 0$ for random behavior. In case of temporal correlations $S(f)$ normally grows with time, and an increasing share of temporal fluctuations is admitted at lower frequencies. As a result the exponent α generally takes on negative values.

In contrast to the normalized variance, the estimation of $S(f)$ is straightforward. It can be determined via the fast Fourier transform for an equally sampled data set. To analyze the power spectrum of the sequence of detected events we thus sampled the event catalog at 1 Hz, and calculated its Fourier transform. To cover the same time range as for the normalized variance we used a frequency range of four decades. The resulting power spectrum is shown in figure 4.9. It confirms previous observations. The spectrum exhibits a clear 1/f like monotonic decrease characterized by a power-law with $\alpha \sim -1$. For times scales smaller than 100 s ($f > 10^{-2}$ Hz) it deviates from this behavior. This deviation can be attributed to the limited resolution of the event catalog. At time scales smaller than 100 s temporal fluctuations are mainly controlled by puffing events which are sparsely detected at the signal/noise boundary. However, in case of the normalized variance this deviation is smoothed out by the inherent counting process. The same is valid for oscillations in the remaining part of the spectrum. Despite these differences both measures provide consistent results. Their power-law behavior reveals the presence of scale-invariant temporal fluctuations.

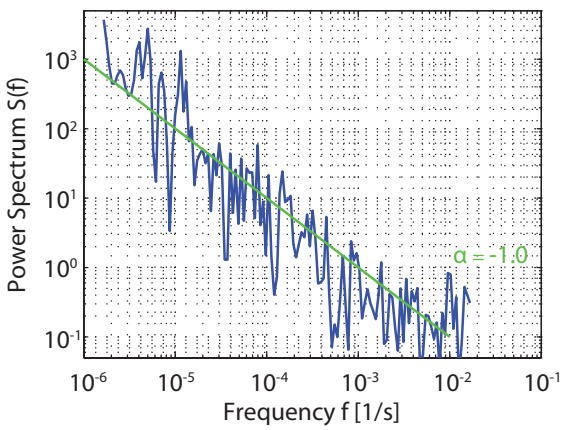

Figure 4.9: Power spectrum of event time sequence as recorded by infrasound. The spectrum shows a clear 1/f like monotonic decrease characterized by power-law behavior over four decades as illustrated by the green line. The considered frequency range covers time scales from seven days to one minute.

4.1.7 Discussion

The above results demonstrate that explosive degassing at Yasur is scale-invariant in every aspect. Explosion magnitudes and return times feature power-law statistics. Variations in these statistics result from waxing and waining phases in degassing behavior and correlate with changes in surface activity. The scale-invariance of the temporal recurrence of explosive degassing further shows that temporal fluctuations in degassing behavior are correlated in time. The combination of these findings indicates that normal Strombolian activity at Yasur is neither random nor stationary. Similar observations at Stromboli volcano support this idea (see Appendix). This is at odds with previous work (*Settle and McGetchin*, 1980; *Bottiglieri et al.*, 2005; *De Lauro et al.*, 2009; *De Martino et al.*, 2011b,a, compare section 4.1.6). It moreover bears important implications for the current models of normal Strombolian activity as we will discuss in the following.

To start we base our argument on three key points:

(1) The overall scale-invariance of explosive degassing suggests that a single process is driving explosive gas release. The genesis of all explosive events is therefore controlled by the same mechanism.

(2) According to the work of *James et al.* (2009) we may conclude that low-magnitude events involve smaller gas volumes than high-magnitude events. The scale-invariance in explosion magnitude can thus be transferred to a scale-invariance in terms of explosion size.

(3) The recurrence of explosive degassing is correlated in time and hence controlled by a non-random process.

We require the current models for active degassing to explain all three key points to assess their validity.

In the foam collapse model (*Jaupart and Vergniolle*, 1988, 1989) there are two general scenarios for gas slug formation. Either all slugs form at the same depth or at different depths within the plumbing system. The first scenario would imply the presence of a single geometrical discontinuity at depth. The entire size range of slugs would then form at this discontinuity. Yet as pointed out in *Jaupart and Vergniolle* (1988) the slug size depends on the magma viscosity and surface tension. The validation of this scenario would hence require temporal changes of these parameters. These changes must however occur at an unreasonable rate to explain the co-existence of small and large explosions. As a consequence we discard this scenario.

In contrast, the second scenario would be independent of temporal changes. Here, slugs would form at several discontinuities within the plumbing system. Each discontinuity would then produce slugs of a particular size. This is however at odds with the continuous size range of explosions observed at the surface. We therefore conclude that the foam collapse model is limited by the scale-invariance in terms of explosion size.

The rise speed dependent model (*Wilson and Head*, 1981; *Parfitt and Wilson*, 1995) does not have this limitation. Here, the basic mechanism for slug genesis is bubble coalescence. Provided that the fundamental coalescence process is independent of bubble volume the resulting slug size distribution could indeed be of power-law form (*Lovejoy et al.*, 2004, and references within). The rise speed dependent model could thus account for the scale-invariance in terms of explosion size.
Nevertheless, a complete approval of the model proves difficult in view of the non-randomness of the degassing process. In general, bubble coalescence is a random phenomenon. The only way to explain the observed recurrence behavior is to impose a scale-invariant coalescence rate. However, there is no real argument in favor of this theory. In summary, neither the foam collapse model nor the rise speed dependent model can account for all observations. A different model for slug genesis is required to satisfy all three key points.

In theory there are several mechanisms which might explain all observations (for a review of the principal mechanisms generating power-law behavior see *Newman*, 2005; *Lowen and Teich*, 2005). One particular attractive mechanism in the context of Strombolian activity is that of percolation (e.g. *Stauffer and Aharony*, 1991). It was already used in the model of closed- and open-system degassing proposed by *Burton et al.* (2007b). According to percolation theory - as discussed below - it may account for the scale-invariance in terms of explosion size. In the framework of self-organized critical phenomena it may moreover explain the temporal scale-invariance of explosive degassing, namely the 1/f like power spectrum (*Bak et al.*, 1987). We therefore sketch a new 'percolation' model of active degassing based on previous considerations.

'Percolation' Model for Active Degassing

The framework for our model stems from the model of *Burton et al.* (2007b). In this model differences in density and viscosity of volatile-rich and volatile-poor magma drive convective overturn inside the conduit. Volatile-rich magma then ascends in quasi closed-system conditions until it becomes sufficiently vesiculated to allow for efficient passive degassing. One important aspect of magma ascent is continuous

vesiculation. During ascent the void fraction of the magma increases and bubbles start to interconnect. At a vesicularity of about 0.3 the magma bubble mixture reaches the critical point of percolation (CPP). The passage of this point is the key element in our model for several reasons.
First, the bubble size distribution should be scale-invariant at the CPP. Given that bubbles coalesce once they adjoin bubble coalescence can be treated as a general problem of connected geometric clusters. The study of these clusters - percolation theory - then predicts that their size distribution is self-similar (e.g. *Isichenko*, 1992; *Stauffer and Aharony*, 1991). The CPP may thus account for the scale-invariance in terms of explosion size.
Second, permeability should develop only above the CPP (compare *Burton et al.*, 2007b). The main degassing pathways are established further up inside the conduit. The CPP itself may hence provoke slug genesis given that bubbles decouple from the magma. The time scale of their ascent must therefore exceed the time scale of magma ascent. This implies that larger bubbles ascend from deeper parts inside the conduit[1], and might explain the different gas composition of large and small Strombolian explosions (*Oppenheimer et al.*, 2006; *Burton et al.*, 2007a).
Third, gas exsolution continuously drives the magmatic system towards the CPP. Criticality appears naturally and is an attractor for the system's dynamics. The magmatic system can hence be considered a self-organized critical, or SOC system (e.g. *Bak et al.*, 1988; *Turcotte*, 1999; *Frigg*, 2003)[2]. This offers a simple explanation for the temporal scale-invariance of explosive gas release (*Bak et al.*, 1987).

The concept of our model is shown in figure 4.10. It can be summarized as follows: (1) upon magma ascent gas exsolution drives the magmatic system towards the CPP, where the bubble size distribution becomes scale-invariant, (2) owing to their size a certain range of bubbles gradually exhibits a rise speed exceeding the magma ascent speed; these bubbles start to rise as a separate phase in form of a slug to cause explosions at the surface, (3) very small bubbles remain with the ascending parental magma due to their negligible rise speed; their growth contributes to an increase in vesicularity which then promotes the transition to open-system degassing as described by *Burton et al.* (2007b).
In essence, slug genesis is caused by a change of the bubble size distribution from mono-disperse to power-law. This induces a change in bubble rise velocity which

[1] in case of a fixed magma viscosity and density of ascending magma and an increasing magma rise rate as discussed by *Burton et al.* (2007b)

[2] Formally, SOC is a property of a dissipative dynamic system with extended degrees of freedom possessing the following properties: (1) highly non-linear behavior, namely a critical point, (2) a slow driving force inducing small perturbations from the critical state and (3) scale-invariance. In our model the first property corresponds to the CPP. The second property is given by permanent gas exsolution, and the third property reflects the scale-invariance of the bubble size distribution.

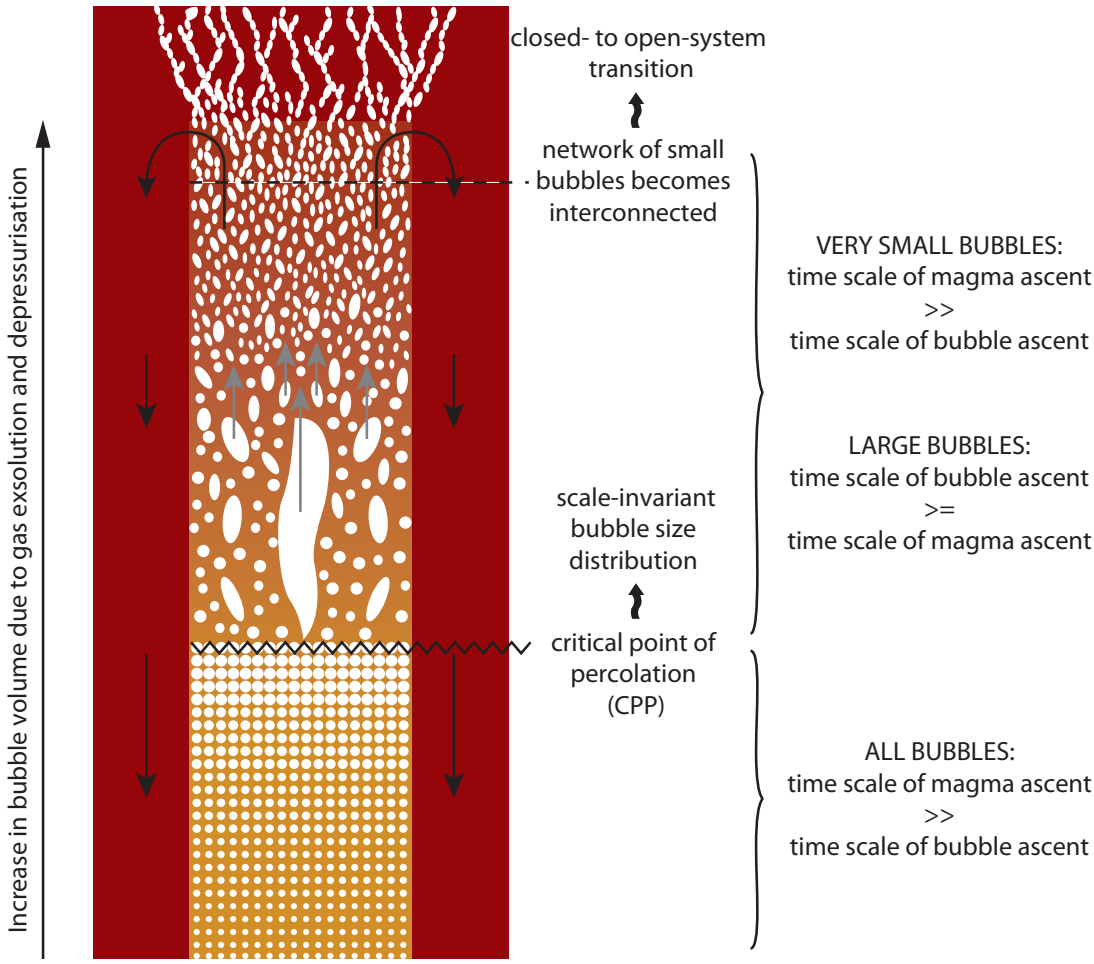

Figure 4.10: Schematic sketch of the 'percolation' model for active degassing. Volatile-rich magma ascends through an annulus of descending degassed volatile-poor magma. On ascent bubbles inside the magma form and increase in volume due to gas exsolution and depressurisation. At a vesicularity of about 0.3 the magma bubble mixture reaches the CPP, and the bubble size distribution becomes scale-invariant. The rise speed of large bubbles now exceeds the rise speed of the ascending magma. Therefore large bubbles start to rise as a separate phase in form of a slug. Smaller-sized bubbles have to grow further to ascend freely, i.e. they are sourced at shallower depth. Very small bubbles remain with the ascending magma due to their negligible rise speed. This leads to a permanent increase in vesicularity until the transition from closed- to open-system degassing takes place as discussed by *Burton et al.* (2007b).

allows the separate ascent of slugs and magma. The overall scale-invariance of explosive degassing would then simply reflect the nature of the bubble size distribution and the self-organization of the magmatic system towards the CPP. Superordinate changes in explosive degassing in terms of explosion rate and explosion magnitude would however indicate changes in the entire magmatic system.

Implications of Changes in Explosive Degassing

As proposed in section 4.1.6 changes in explosive degassing observed at Yasur may be explained by variations in magma supply - a scenario widely discussed in literature (e.g. *Stevenson and Blake*, 1998; *Ripepe et al.*, 2002, 2005b, 2008; *Lautze and Houghton*, 2007; *Palma et al.*, 2011). New supply of fresh gas-rich melt increases the overall gas concentration inside the conduit. In the 'percolation' model fresh magma recharge would shift the CPP to greater depth. Due to the overall higher gas concentration the CPP is reached earlier during magma rise. A disruption in magma supply promotes the contrary. Ongoing degassing decreases the volatile content of the entire magma column. As a consequence the CPP would migrate to shallower depth.
Variable supply of fresh melt may further account for the observed link between explosive degassing and surface activity. During phases of enhanced supply juvenile, low-viscous magma charges the conduit. Explosive fragmentation is dominated by inertia (*Namiki and Manga*, 2008) and high-intensity ash-free explosions occur (compare e.g. *Ripepe et al.*, 2008). Reduced magma recharge in contrast involves melt maturation. The magma becomes brittle, and the ash load of explosion increases (e.g. *Lautze and Houghton*, 2007; *Taddeucci et al.*, 2004; *Andronico et al.*, 2009).

To explain our observations at Yasur we combine both aspects to describe the cyclic fashion of active degassing. We consider the model as discussed before, i.e. in the absence of magma recharge, as reference for normal activity characterized by a standard explosion rate and magnitude (figure 4.11(a)). Ongoing degassing then gradually decreases the volatile content inside the conduit (figure 4.11(b)). As a result the CPP migrates to shallower depth. Slugs are sourced from shallower levels and the overall size of explosions is smaller. Due to the lowered gas concentration the number of explosions also decreases. The reduction of magma discharge promotes melt maturation. Differences in the rheology of ascending and descending magma become less pronounced. Convective overturn is slow and fragmentation efficient. The ash-load of explosions is high. After a time a batch of juvenile magma then enters the conduit (figure 4.11(c)). This increases the volatile content in the lower part of the magma column. The CPP shifts to greater depth and larger explosions start to occur. Due to the strong differences between ascending and descending magma convection increases again. Yet the overall explosion number remains low due to the degassed state of the major part of magma column[3]. Once the juvenile magma occupies the entire conduit (figure 4.11(d)) the gas concentration is high and the number of explosions is elevated. The overall size of explosions remains large.

[3]This would explain the delay between the increase in explosion magnitude and explosion rate seen from comparison of figure 4.1 and figure 4.3 around the start of day three and day ten.

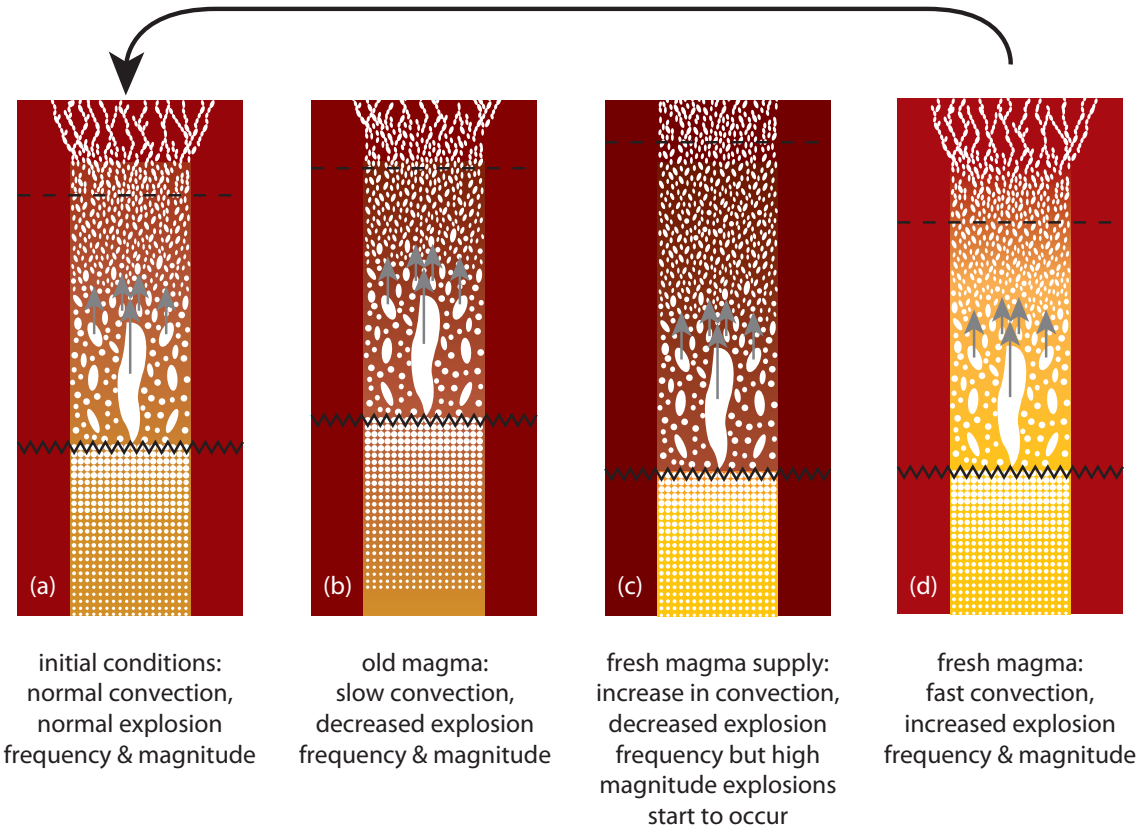

Figure 4.11: Schematic sketch of a cycle of active degassing. (a) At first the magmatic system is characterized by normal activity as shown in figure 4.10. (b) Ongoing degassing decreases the gas concentration in the magma column. As a consequence the CPP migrates to shallower depth, and the number and size of explosions decreases. Magma discharge is reduced and convection is slow. Fragmentation becomes more efficient, and the ash-load of explosions increases. (c) Degassing of old magma continues while a batch of juvenile magma enters the conduit. The volatile content in the lower part of the magma column increases, the CPP shifts to greater depth and larger explosions start to occur. Convection increases again, but the overall explosion number remains low due to the degassed state of the main part of magma. (d) Once the juvenile magma is present in the entire conduit the number and size of explosions is high. Fragmentations is dominated by inertia, and ash-free explosions occur. Fast convective overturn entails efficient degassing which drives the system back to state (a).

Fragmentation is inertia-dominated and ash-free explosions occur. Fast convective overturn entails efficient degassing which drives the system back to the reference state (figure 4.11(a)). The described cycle then starts anew.

In summary, we suggest that time-variant magma recharge induces changes in explosive degassing and that concomitant changes in magma rheology cause concurrent changes in surface activity at Yasur in a similar way as at other Strombolian volca-

noes. We further argue that low-magnitude explosions stem from shallower parts of the conduit, whereas high-magnitude events originate from greater depth in agreement with the work of *Oppenheimer et al.* (2006); *Burton et al.* (2007a); *Bani et al.* (2013). Yet the overall scale-invariance of explosive degassing contradicts previous ideas regarding the mechanism of gas slug formation. We propose that the power-law behavior finds a unifying explanation within the model of 'percolation' in which overall changes in volatile concentration shift the depth of slug formation inside the conduit. This modifies explosive degassing in terms of explosion rate and magnitude, and explains the waxing and waining phases in degassing behavior. Long-term application of OP-FTIR spectroscopy (e.g. *Mori et al.*, 1995; *Francis et al.*, 1998; *Horrocks et al.*, 2001) could provide evidence for the associated systematic variation in volcanic gas emissions.

4.1.8 Conclusion

Our study illustrates the time variability of normal Strombolian activity at Yasur volcano, Vanuatu, and helps to assess previous results on normal Strombolian behavior. It highlights the value of a continuous multi-parameter data base to reliably capture the statistics of explosive degassing. In comparison to seismic and Doppler radar data infrasound recordings provide the most detailed measure of explosive gas release. It further demonstrates the need to integrate different statistical measures to obtain meaningful results. Non-random behavior does not necessarily show in simple return time statistics. Additional statistics are essential for a proper mapping of the temporal structure of the degassing process. Future studies on degassing behavior should take these aspects into account.

4.1.9 Appendix

Analysis of Activity at Stromboli volcano, Italy

To generalize our observations we analyzed the activity of Stromboli volcano, Italy. For this purpose we used a Doppler radar data set of 10100 Strombolian explosions which we recorded in 2011 together with M. Ripepe. The data set maps the explosive activity of Stromboli's north-eastern vent during 79 days. When compared to the data set from Yasur it offers less detail. Due to a different viewing geometry of the radar it mainly comprises records of intermediate to high-intensity explosions. Nevertheless, it provides the possibility to extend our work to longer time scales as we will show below.

To analyze the data we followed the same approach as for Yasur. At first we cataloged all events based on the recorded velocity information. We then used magnitude groups to specify their intensity. To this end we evaluated their maximum Doppler velocity via the magnitude classification scheme given in table 4.1. The resulting temporal distribution of explosion magnitudes is shown in figure 4.12. Like at Yasur, the magnitude of explosions varies over time. Explosive activity cycles through periods of high and low intensity. Owing to the lack of complementary observations, it was however impossible to assess these periods in detail. The role of changes in surface activity and the coupling between puffing and explosions remains unclear.

Nevertheless, we studied the explosions' magnitude distribution. For this purpose we determined the distribution of the entire event catalog as well as the cumulative velocity distribution of every two days. The results are presented in figure 4.13 on the left and right, respectively. The shape of the magnitude distribution is in line with observations at Yasur. However, the velocity range of one decade is too short to postulate power-law behavior. Still the trend in magnitude suggests that all explosions are driven by the same process. Like at Yasur, this process exhibits a certain temporal behavior as witnessed by the changing shape of the cumulative velocity distribution.

To further elucidate this behavior we investigated the distribution of the recorded inter-event time intervals. For the sake of consistency we ranked the recorded intervals again via a logarithmic classification scheme. The respective return time classes are reported in table 4.3. The resulting return time distribution is displayed on the left in figure 4.14. Other than at Yasur, there is no clear trend in the data. The return time distribution rather exhibits two separate domains (see figure 4.14, left). To better understand this feature it is worth considering the time scales of each domain. While the first domain covers time scales in the range of the explosions' duration ($\tau < 10\ s$) , the time scales of the second domain are partly larger than those observed at Yasur. This implies that the first domain maps the time between explosive sub-events instead of the time between successive explosions. The return times of the second domain between 100 s and 30 minutes are more typical of the latter seeing that mainly intermediate to high-intensity explosions were recorded.
Despite these differences, the recurrence of explosive degassing exhibits temporal variations similar to those found at Yasur. To demonstrate this effect we compare the cumulative return time distribution of every two days on the right in figure 4.14. The changing shape of the distributions indicates temporal variations in recurrence behavior. However, their overall shape is better described by an exponential distribution. This is in line with the limited resolution of the data set as discussed in the final paragraph of section 4.1.6 (see figure 4.7). Yet it does not imply random behav-

ior. For random behavior the return time distribution should be stationary in time, i.e. its shape should only depend on the length and not on the time of observation. In other words, explosions should occur at the same average rate at all times. This is at odds with the observed variations in event rate as shown by the cumulative velocity and return time distributions.

To substantiate this argument we determined the power spectrum of the recorded event time sequence. To exploit the length of the data set we adapted the frequency range to time scales between ten minutes and forty days. The resulting spectrum is presented in figure 4.15. It provides clear evidence for non-random behavior in form of a 1/f like monotonic decrease over two and a half decades. For time scales smaller than 1.4 h ($f > 2 \times 10^{-4}$ Hz) there is a significant deviation from this behavior. It is probable that temporal fluctuations in activity cannot be resolved due to the scarce recording of low-intensity explosions.
To illustrate this issue we created a suitable surrogate data set based on our Doppler radar recordings from Yasur, i.e. we discarded events with a Doppler velocity of less than ∼25 m/s. Figure 4.16 contrasts the respective power spectrum of the true and surrogate observations. The spectrum of the original event time sequence shows a clear 1/f like monotonic decrease as expected. However, when low-intensity explosions are removed as in the surrogate case, a deviation similar to the one at Stromboli can be observed (compare figure 4.15). Temporal correlations in activity cannot be resolved due to the removal of low-intensity explosions.

In all, the results at Stromboli support our findings at Yasur, and extend them to longer time scales. Despite the limited resolution of the data set key observations are similar. Explosive degassing is scale-invariant and subject to temporal variations as witnessed by changes in explosion intensity and recurrence behavior. The related temporal dynamics exposes significant time-correlation which argues against a random occurrence of explosions. Non-random behavior is however not manifested in the global return time statistics due to the limited resolution of the data set. Additional statistics are essential for a proper mapping of the dynamics of the process.

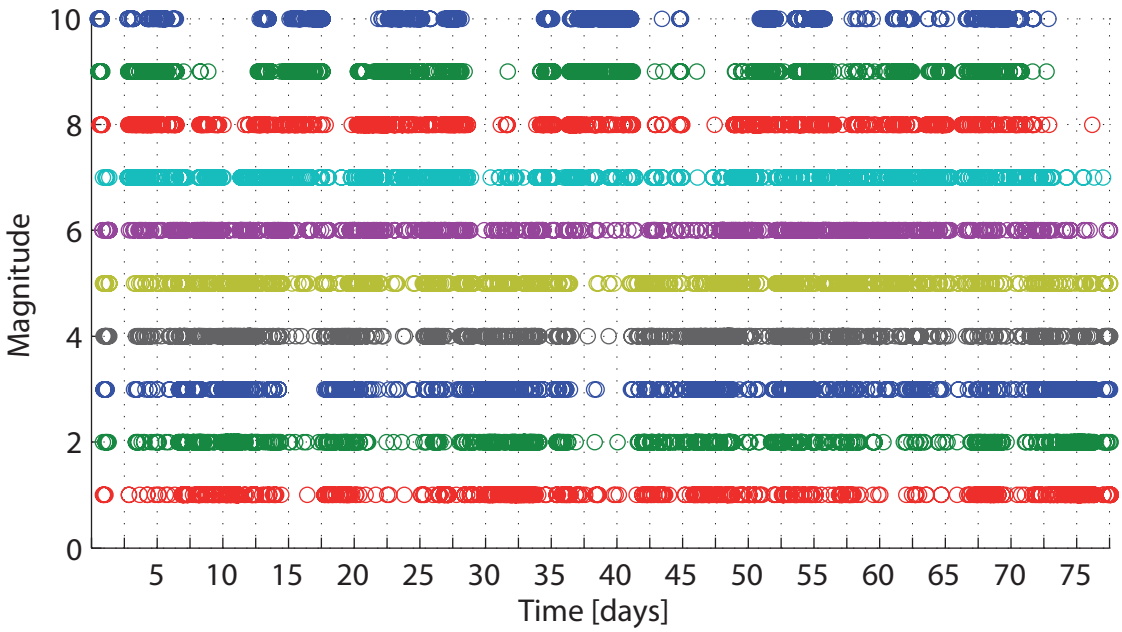

Figure 4.12: Magnitude of events as recorded by Doppler radar at Stromboli. The origin of the x-axis is 23.06.2011 and annotations on the x-axis mark the end of every fifth measurement day. Magnitude classes are color-coded in the same way as in figure 4.2. Activity varies over time. Explosion magnitudes show phases of waxing and waining like in figure 4.2. The potential link between these phases and changes in surface activity remains unclear due to the lack of complementary observations.

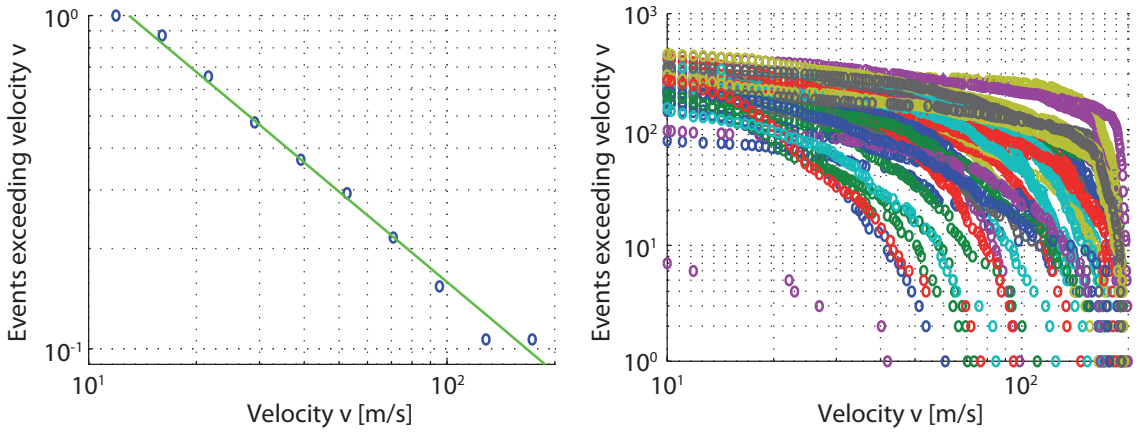

Figure 4.13: Magnitude distribution of events as recorded by Doppler radar at Stromboli. On the left the magnitude distribution of the entire event catalog is shown. Magnitude classes are the same as in figure 4.12, and their corresponding velocities are marked on the x-axis. On the y-axis the normalized number of events in each magnitude class is given, and the green line depicts the best fit to the data. On the right the temporal change of the cumulative velocity distribution is presented. Cumulative distributions were calculated using time intervals of 48 hours, and are recurrently color-coded. In this part of the figure the y-axis maps the absolute number of events to demonstrate differences in event number. The shape of the distributions reflects temporal changes in activity. The overall magnitude distribution on the left is a superposition of the different distributions on the right.

Rank	Return time range [s]	
1	0.72	1.57
2	1.57	3.43
3	3.43	7.49
4	7.49	16.39
5	16.39	35.86
6	35.86	78.43
7	78.43	171.56
8	171.56	375.26
9	375.26	820.84
10	820.84	1795.50

Table 4.3: Summary of return time classes used to analyze the return time distribution at Stromboli. The classes are ranked according to their respective return time range.

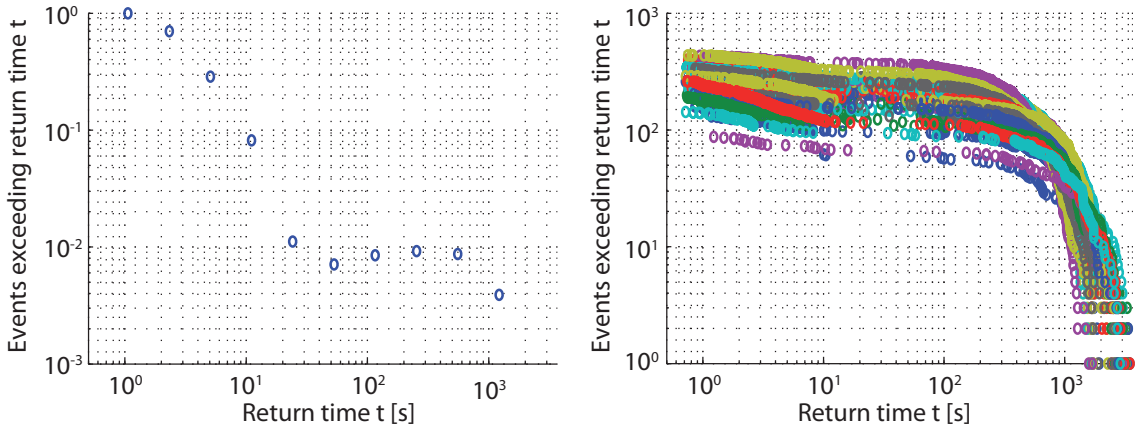

Figure 4.14: Return time distribution of events as recorded by Doppler radar at Stromboli. On the left the return time distribution of the entire event catalog is presented. Return times are denoted on the x-axis, which covers a time range between 0.5 seconds and thirty minutes. The y-axis maps the normalized number of events in each return time class, and there is no clear trend in the data. On the right the temporal change of the cumulative return time distribution is shown. Cumulative distributions were calculated using time intervals of 48 hours, and are color-coded like in figure 4.13. Please note that the y-axis indicates the absolute number of events in this part of the figure. The changing shape of the distributions mirrors changes in activity. Their overall shape is best described by an exponential distribution when compared to figure 4.7.

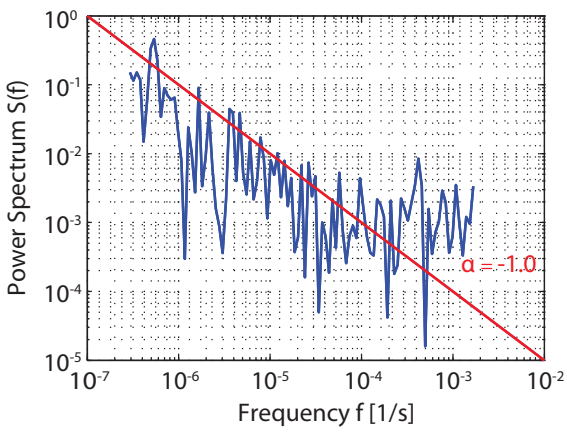

Figure 4.15: Power spectrum of event time sequence as recorded by Doppler radar at Stromboli. The spectrum exhibits a 1/f like monotonic decrease over two and a half decades as illustrated by the red line. At smaller time scales there is a significant deviation from this behavior. The considered frequency range covers time scales from about forty days to ten minutes.

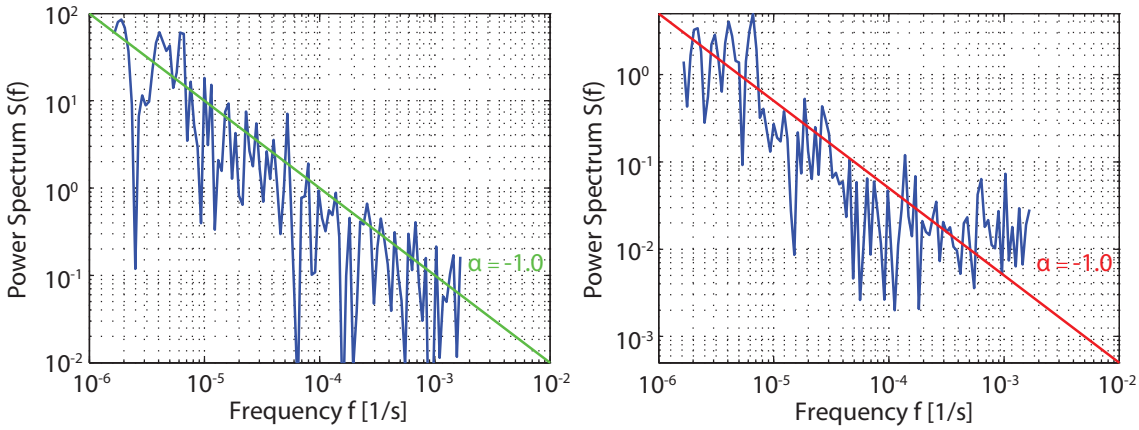

Figure 4.16: Power spectrum of the entire event time sequence as recorded by Doppler radar at Yasur versus the spectrum of the time sequence without low-intensity events. On the left the power spectrum of the entire event time sequence is presented. It shows a clear 1/f like monotonic decrease characterized by power-law behavior as depicted by the green line. In the surrogate case illustrated on the right, a deviation form power-law behavior can be observed at smaller time scales. The considered frequency range covers time scales from seven days to ten minutes.

Chapter 5

Conclusions and Outlook

In this thesis I presented a comprehensive analysis of different geophysical measurements and numerical modeling. The combination of these research fields allowed for an improvement of our understanding of Strombolian activity and its associated geophysical signals. Comparison of activity at Yasur volcano, Vanuatu, and Stromboli volcano, Italy, further helped to put the obtained results into a wider perspective.

Via an extensive measurement campaign it was possible to study the activity of Yasur volcano in the context of different explosive styles. Doppler radar, infrared and infrasound recordings permitted to determine the geophysical signature of ash-free and ash-rich explosions in terms of material movement, temperature, and excess pressure. Joint analysis of these data revealed the regime-like persistence of a given explosive style through time. Detailed investigations showed significant differences between individual explosive forms in agreement with observations at Stromboli volcano. A combined interpretation of all observations further helped to elucidate the origin of ash-free and ash-rich explosions. Changes in magma rheology are thought to be the main cause of ash-rich fragmentation. Temporal tracking of activity likewise gave first indications for a link between surface activity and explosive degassing. In terms of explosion velocity and excess pressure there is a general correlation between explosive style and intensity. Careful inspection of selected pressure signals however showed that contrasting infrasonic waveforms relate to each explosive regime. This is in line with a different explosion dynamics, but may also denote changes in wave propagation.

The impact of changes in wave propagation was therefore assessed by a numerical study. Explicit comparison of three representative Strombolian-type scenarios showed that different signal signatures result from wave propagation under ash-free and ash-rich conditions. In-depth analysis of all observations revealed a modifica-

tion of signals due to Doppler shifting, density, transmission and interference effects. With reference to real data recorded at Yasur this finding suggests that the observed infrasonic signatures may partly derive from changes in wave propagation. Theory implies that the compressive signal onset is pristine, while the remaining part of the signal is altered by above mentioned effects. This contradicts the common assumption of uniform wave propagation in the direct volcanic environment. A proper comprehension of the propagation setting is crucial for a correct interpretation of the explosion dynamics. As a consequence, only the signal onset was considered to further elucidate the link between surface activity and explosive degassing.

In view of Yasur's frequent activity a new statistical approach was used for this task. Through integration of different statistical measures it was shown that explosive degassing is overall scale-invariant. Thorough analysis of explosion magnitudes and return times illustrated the power-law character of explosive gas release. Temporal changes in this character were found to correlate with changes in surface activity. Additional examination of the related temporal dynamics further exposed the temporal structure of explosive degassing. Explosive activity features scale-invariance also in terms of its temporal structure. This is at odds with the current paradigm of normal Strombolian behavior. The combination of all findings indicates that explosive degassing is controlled by a single, non-random process. Similar observations at Stromboli volcano corroborate this idea. A different model for active degassing at Strombolian volcanoes thus had to be developed.

In accordance with previous work on passive degassing a new 'percolation' model was proposed. In this model slugs form during magma rise due to a change of the bubble size distribution at the critical point of percolation. Time-variant magma recharge induces changes in gas supply which shifts the depth of percolation in the conduit. This modifies the onset of gas-melt segregation and should hence alter the composition of the rising gas phase in a systematic fashion. Continuous OP-FTIR measurements could therefore help to validate the model as they may track long-term variations in volcanic gas emissions during Strombolian activity. They should moreover complement the used measurement techniques to quantify the temporal variability of the degassing process.

In summary the results of this work illustrate the importance of combined studies that overcome the limitations of a single field of research. They clearly demonstrate the need for a more comprehensive view of Strombolian activity and the associated observations. This holds in particular for the scale-invariant nature of explosive gas release which was only captured through combination of different analysis techniques. Finally, the results highlight the value of a continuous multi-parameter data acquisition campaign. Based on the continuity of the data set this study was the

first to establish a solid link between surface activity and explosive degassing. The integration of different data types likewise helped to improve our understanding of explosion style characteristics and explosion style transitions. Besides that it safeguarded the formation and use of a representative data base. It showed that surface measurements are essential for a reliable characterization of the degassing process. Similar studies at other volcanoes should take these aspects into account in order to contribute to a better understanding of volcanic processes and the related hazards.

Bibliography

Abramoff, M. D., Magalhaes, P. J. and Ram, S. J., 2004. Image processing with ImageJ. *Biophotonics International*, 11:36–42.

Allard, P., Carbonnelle, J., Metrich, N., Loyer, H. and Zettwoog, P., 1994. Sulphur output and magma degassing budget of Stromboli volcano. *Nature*, 368:326–330. doi: 10.1038/368326a0.

Allen, S., 2005. Complex spatter-and pumice-rich pyroclastic deposits from an andesitic caldera-forming eruption: The Siwi pyroclastic sequence, Tanna, Vanuatu. *Bulletin of Volcanology*, 67:27–41. doi: 10.1007/s00445-004-0358-6.

Andronico, D., Cristaldi, A., Del Carlo, P. and Taddeucci, J., 2009. Shifting styles of basaltic explosive activity during the 2002–03 eruption of Mt. Etna, Italy. *Journal of Volcanology and Geothermal Research*, 180:110–122. doi: 10.1016/j.jvolgeores.2008.07.026.

Arrowsmith, S. J., Johnson, J. B., Drob, D. P. and Hedlin, M. A. H., 2010. The seismoacoustic wavefield: A new paradigm in studying geophysical phenomena. *Reviews of Geophysics*, 48:RG4003. doi: 10.1029/2010RG000335.

Auzende, J. M., Pelletier, B. and Eissen, J. P. The North Fiji Basin: Geology, structure and geodynamic evolution. In Taylor, B., editor, *Back-Arc Basin: Tectonics and Magmatism*, pages 139–175. Springer, 1995. ISBN 0306449374.

Bak, P., Tang, C. and Wiesenfeld, K., 1987. Self-organized criticality: An explanation of the 1/f noise. *Physical Review Letters*, 59:381–384. doi: 10.1103/PhysRevLett.59.381.

Bak, P., Tang, C. and Wiesenfeld, K., 1988. Self-organized criticality. *Physical Review A*, 38:364–374. doi: 10.1103/PhysRevA.38.364.

Bani, P. and Lardy, M., 2007. Sulphur dioxide emission rates from Yasur volcano, Vanuatu archipelago. *Geophysical Research Letters*, 34:L20309. doi: 10.1029/2007GL030411.

Bani, P., Oppenheimer, C., Allard, P., Shinohara, H., Tsanev, V., Carn, S., Lardy, M. and Garaebiti, E., 2012. First estimate of volcanic SO_2 budget for Vanuatu island arc. *Journal of Volcanology and Geothermal Research*, 211/212:36–46. doi: 10.1016/j.jvolgeores.2011.10.005.

Bani, P., Harris, A. J. L., Shinohara, H. and Donnadieu, F., 2013. Magma dynamics feeding Yasur's explosive activity observed using thermal infrared remote sensing. *Geophysical Research Letters*, 40:3830–3835. doi: 10.1002/grl.50722.

Barberi, F., Rosi, M. and Sodi, A., 1993. Volcanic hazard assessment at Stromboli based on review of historical data. *Acta Vulcanologica*, 3:173–187.

Belousov, A., Voight, B. and Belousova, M., 2007. Directed blasts and blast-generated pyroclastic density currents: a comparison of the Bezymianny 1956, Mount St Helens 1980, and Soufrière Hills, Montserrat 1997 eruptions and deposits. *Bulletin of Volcanology*, 69:701–740. doi: DOI:10.1007/s00445-006-0109-y.

Bercovici, D. and Michaut, C., 2010. Two-phase dynamics of volcanic eruptions: Compaction, compression and the conditions for choking. *Geophysical Journal International*, 182:843–864. doi: 10.1111/j.1365-246X.2010.04674.x.

Blackburn, E., Wilson, L. and Sparks, R., 1976. Mechanism and dynamics of Strombolian activity. *Journal of the Geological Society*, 132:429–440. doi: 10.1144/gsjgs.132.4.0429.

Bluth, G. J. S. and Rose, W. I., 2004. Observations of eruptive activity at Santiaguito volcano, Guatemala. *Journal of Volcanology and Geothermal Research*, 136:297–302. doi: 10.1016/j.jvolgeores.2004.06.001.

Bottiglieri, M., Martino, S. D., Falanga, M., Godano, C. and Palo, M., 2005. Statistics of inter-time of Strombolian explosion-quakes. *Europhysics Letters*, 72(3): 493–498. doi: 10.1209/epl/i2005-10258-0.

Buckingham, M. J. and Garcés, M. A., 1996. Canonical model of volcano acoustics. *Journal of Geophysical Research*, 101:8129–8151. doi: 10.1029/95JB01680.

Burton, M., Allard, P., Mure, F. and La Spina, A., 2007a. Magmatic gas composition reveals the source depth of slug-driven Strombolian explosive activity. *Science*, 317:227 – 230. doi: 10.1126/science.1141900.

Burton, M., Mader, H. and Polacci, M., 2007b. The role of gas percolation in quiescent degassing of persistently active basaltic volcanoes. *Earth and Planetary Science Letters*, 264:46–60. doi: 10.1016/j.epsl.2007.08.028.

Calmant, S., Pelletier, B., Lebellegard, P., Bevis, M., Taylor, F. W. and Phillips, D. A., 2003. New insights on the tectonics along the New Hebrides subduction zone based on GPS results. *Journal of Geophysical Research*, 108:2319. doi: 10.1029/2001JB000644.

Calvari, S. and Pinkerton, H., 2004. Birth, growth and morphologic evolution of the 'Laghetto' cinder cone during the 2001 Etna eruption. *Journal of Volcanology and Geothermal Research*, 132:225–239. doi: 10.1016/S0377-0273(03)00347-0.

Cannata, A., Montalto, P., Privitera, E., Russo, G. and Gresta, S., 2009. Tracking eruptive phenomena by infrasound: May 13, 2008 eruption at Mt. Etna. *Geophysical Research Letters*, 36:L05304. doi: 10.1029/2008GL036738.

Caplan-Auerbach, J., Bellesiles, A. K. and Fernandes, J. J., 2008. Estimates of gas flux from infrasonic recordings of Vulcanian blasts at Augustine volcano, Alaska. *Eos Transactions AGU, Fall Meeting Supplement*, 89:V51E–2088.

Caplan-Auerbach, J. and McNutt, S. R., 2003. New insights into the 1999 eruption of Shishaldin volcano, Alaska, based on acoustic data. *Bulletin of Volcanology*, 65:405–417. doi: 10.1007/s00445-002-0267-5.

Caplan-Auerbach, J., Bellesiles, A. and Fernandes, J. K., 2010. Estimates of eruption velocity and plume height from infrasonic recordings of the 2006 eruption of Augustine volcano, Alaska. *Journal of Volcanology and Geothermal Research*, 189:12–18. doi: 10.1016/j.jvolgeores.2009.10.002.

Carnay, J. N. and MacFarlane, A., 1979. Geology of Tanna, Aneityum, Futuna and Aniva. *New Hebrides Geological Survey Report*, 1:5–29.

Carniel, R. and Iacop, F., 1996. On the persistency of crater assignment criteria for Stromboli explosion-quakes. *Annals of Geophysics*, 39:347–359. doi: 10.4401/ag-3964.

Chen, J. K., Taylor, F. W., Edwards, R. L., Cheng, H. and Burr, G. S., 1995. Recent emerged reef terraces of the Yenkahe resurgent block, Tanna, Vanuatu: Implications for volcanic, landslide and tsunami hazards. *The Journal of Geology*, 103:577–590. doi: 10.1086/629777.

Chouet, B., Saccorotti, G., Dawson, P., Martini, M., Scarpa, R., De Luca, G., Milana, G. and Cattaneo, M., 1999. Broadband measurements of the sources of explosions at Stromboli volcano, Italy. *Geophysical Research Letters*, 26:1937–1940. doi: 10.1029/1999GL900400.

Chouet, B., Dawson, P., Ohminato, T., Martini, M., Saccorotti, G., Giudicepietro, F., De Luca, G., Milana, G. and Scarpa, R., 2003. Source mechanisms of explosions at Stromboli volcano, Italy, determined from moment-tensor inversions of very-long-period data. *Journal of Geophysical Research*, 108:2019. doi: 10.1029/2002JB001919.

Chouet, B., Dawson, P. and Arciniega-Ceballos, A., 2005. Source mechanism of Vulcanian degassing at Popocatépetl Volcano, Mexico, determined from waveform inversions of very long period signals. *Journal of Geophysical Research*, 110: B07301. doi: 10.1029/2004JB003524.

Chouet, B., Hamisevicz, N. and McGetchin, T. R., 1974. Photoballistics of volcanic jet activity at Stromboli, italy. *Journal of Geophysical Research*, 79:4961–4976. doi: 10.1029/JB079i032p04961.

Colò, L., Ripepe, M., Baker, D. R. and Polacci, M., 2010. Magma vesiculation and infrasonic activity at Stromboli open conduit volcano. *Earth and Planetary Science Letters*, 292:274–280. doi: 10.1016/j.epsl.2010.01.018.

Cole, P., Fernandez, E., Duarte, E. and Duncan, A., 2005. Explosive activity and generation mechanisms of pyroclastic flows at Arenal volcano, Costa Rica between 1987 and 2001. *Bulletin of Volcanology*, 67:695–716. doi: 10.1007/s00445-004-0402-6.

Cox, D. R. and Lewis, P. A. W. *The Statistical Analysis of Series of Events*. Chapman & Hall, 1966. ISBN 978-0412218002.

De Lauro, E., De Martino, S., Falanga, M. and Palo, M., 2009. Modelling the macroscopic behavior of Strombolian explosions at Erebus volcano. *Physics of the Earth and Planetary Interiors*, 176:174–186. doi: 10.1016/j.pepi.2009.05.003.

De Martino, S., Falanga, M., Palo, M., Montalto, P. and Patane, D., 2011a. Statistical analysis of the volcano seismicity during the 2007 crisis of Stromboli, Italy. *Journal of Geophysical Research*, 116:B09312. doi: 10.1029/2010JB007503.

De Martino, S., Palo, M. and Cimini, G. B., 2011b. A statistical study of the Stromboli volcano explosion quakes before and during 2002–2003 eruptive crisis. *Journal of Geophysical Research*, 116:B04303. doi: 10.1029/2010JB008047.

Decker, R. W. and Decker, B. *Mountains of fire: The nature of volcanoes*. Cambridge University Press, 1991. ISBN 0521312906.

Del Bello, E., Llewellin, E. W., Taddeucci, J., Scarlato, P. and Lane, S. J., 2012. An analytical model for gas overpressure in slug-driven explosions: Insights into

Strombolian volcanic eruptions. *Journal of Geophysical Research*, 117:B02206. doi: 10.1029/2011JB008747.

Delle Donne, D., Marchetti, E., Ripepe, M., Ulivieri, G. and G., L., 2006. Monitoring explosive volanic activity using thermal images, Stromboli volcano, Italy. *Eos Transactions AGU, Fall Meeting Supplement*, 87:V43B–1795.

Donnadieu, F., Valade, S. and Moune, S., 2011. Three dimensional transport speed of wind-drifted ash plumes using ground-based radar. *Geophysical Research Letters*, 38:L18310. doi: 10.1029/2011GL049001.

D'Oriano, C., Bertagnini, A. and Pompilio, M., 2010. Ash erupted during normal activity at Stromboli (Aeolian islands, Italy) raises questions on how the feeding system works. *Bulletin of Volcanology*, 73:471–477. doi: 10.1007/s00445-010-0425-0.

Edmonds, M., 2008. New geochemical insights into volcanic degassing. *Philosophical Transactions of the Royal Society A*, 366:4559–4579. doi: 10.1098/rsta.2008.0185.

Fee, D., Steffke, A. and Garces, M., 2010a. Characterization of the 2008 Kasatochi and Okmok eruptions using remote infrasound arrays. *Journal of Geophysical Research*, 115:D00L10. doi: 10.1029/2009JD013621.

Fee, D., Garcés, M. and Steffke, A., 2010b. Infrasound from Tungurahua Volcano 2006-2008: Strombolian to Plinian eruptive activity. *Journal of Volcanology and Geothermal Research*, 193:67–81. doi: 10.1016/j.jvolgeores.2010.03.006.

Fee, D., McNutt, S. R., Lopez, T. M., Arnoult, K. M., Szuberla, C. A. and Olson, J. V., 2011. Combining local and remote infrasound recordings from the 2009 Redoubt Volcano eruption. *Journal of Volcanology and Geothermal Research*, 259:100–114. doi: 10.1016/j.jvolgeores.2011.09.012.

Firstov, P. and Kravchenko, N., 1996. Estimation of the amount of explosive gas released in volcanic eruptions using air waves. *Volcanology and Seismology*, 17: 547–560.

Francis, P., Burton, M. and Op, 1998. Remote measurements of volcanic gas compositions by solar occultation spectroscopy. *Nature*, 396:567–570. doi: 10.1038/25115.

Frigg, R., 2003. Self-organised criticality—what it is and what it isn't. *Studies in History and Philosophy of Science Part A*, 34:613–632. doi: 10.1016/S0039-3681(03) 00046-3.

Gerst, A., Hort, M., Aster, R. C., Johnson, J. B. and Kyle, P. R., 2013. The first second of volcanic eruptions from the Erebus volcano lava lake, Antarctica—Energies,

pressures, seismology, and infrasound. *Journal of Geophysical Research*, 118:3318–3340. doi: 10.1002/jgrb.50234.

Gerst, A. *The first second of a Strombolian volcanic eruption*. PhD thesis, Institut für Geophysik, Universität Hamburg, 2010. URL: http://ediss.sub.uni-hamburg.de/volltexte/2010/4251/.

Godin, O. A., 2002. An effective quiescent medium for sound propagating through an inhomogeneous, moving fluid. *The Journal of the Acoustical Society of America*, 112:1269–1275. doi: 10.1121/1.1504853.

Harris, A. and Ripepe, M., 2007a. Synergy of multiple geophysical approaches to unravel explosive eruption conduit and source dynamics: A case study from Stromboli. *Chemie der Erde - Geochemistry*, 67:1–35. doi: 10.1016/j.chemer.2007.01.003.

Harris, A. and Ripepe, M., 2007b. Temperature and dynamics of degassing at Stromboli. *Journal of Geophysical Research*, 112:B03205. doi: 10.1029/2006JB004393.

Harris, P. D., Branney, M. J. and Storey, M., 2011. Large eruption-triggered ocean-island landslide at Tenerife: Onshore record and long-term effects on hazardous pyroclastic dispersal . *Geology*, 39:951–954. doi: 10.1130/G31994.1.

Horrocks, L. A., Oppenheimer, C., Burton, M. R., Duffell, H. J., Davies, N. M., Martin, N. A. and Bell, W., 2001. Open-path Fourier transform infrared spectroscopy of SO_2: An empirical error budget analysis, with implications for volcano monitoring. *Journal of Geophysical Research*, 106:27647–27659. doi: 10.1029/2001JD000343.

Hort, M., Seyfried, R. and Vöge, M., 2003. Radar Doppler velocimetry of volcanic eruptions: Theoretical considerations and quantitative documentation of changes in eruptive behaviour at Stromboli volcano, Italy. *Geophysical Journal International*, 154:515–532. doi: 10.1046/j.1365-246X.2003.01982.x.

Horwell, C. J. and Baxter, P. J., 2006. The respiratory health hazards of volcanic ash: A review for volcanic risk mitigation. *Bulletin of Volcanology*, 69(1):1–24. doi: 10.1007/s00445-006-0052-y.

Houghton, B. and Gonnermann, H., 2008. Basaltic explosive volcanism: Constraints from deposits and models. *Chemie der Erde - Geochemistry*, 68:117–140. doi: 10.1016/j.chemer.2008.04.002.

Isichenko, M. B., 1992. Percolation, statistical topography, and transport in random media. *Reviews of Modern Physics*, 64:961–1043. doi: 10.1103/RevModPhys.64.961.

James, M. R., Lane, S. J. and Corder, S. B. Modelling the rapid near-surface expansion of gas slugs in low-viscosity magmas. In Lane, S. J. and Gilbert, J. S., editors, *Fluid Motion in Volcanic Conduits: A Source of Seismic and Acoustic Signals*, pages 147–167. Geological Society, 2008. ISBN 1862392625.

James, M. R., Lane, S. J., Wilson, L. and Corder, S. B., 2009. Degassing at low magma-viscosity volcanoes: Quantifying the transition between passive bubble-burst and Strombolian eruption. *Journal of Volcanology and Geothermal Research*, 180:81–88. doi: 10.1016/j.jvolgeores.2008.09.002.

Jaquet, O. and Carniel, R., 2001. Stochastic modelling at Stromboli: A volcano with remarkable memory. *Journal of Volcanology and Geothermal Research*, 105: 249–262. doi: 10.1016/S0377-0273(00)00254-7.

Jaupart, C. and Vergniolle, S., 1989. The generation and collapse of a foam layer at the roof of a basaltic magma chamber. *Journal of Fluid Mechanics*, 203:347–380. doi: 10.1017/S0022112089001497.

Jaupart, C. and Vergniolle, S., 1988. Laboratory models of Hawaiian and Strombolian eruptions. *Nature*, 331:58–60. doi: 10.1038/331058a0.

Johnson, J. and Aster, R., 2005. Relative partitioning of acoustic and seismic energy during Strombolian eruptions. *Journal of Volcanology and Geothermal Research*, 148:334–354. doi: 10.1016/j.jvolgeores.2005.05.002.

Johnson, J., Aster, R., Jones, K., Kyle, P. and McIntosh, W., 2008. Acoustic source characterization of impulsive Strombolian eruptions from the Mount Erebus lava lake. *Journal of Volcanology and Geothermal Research*, 177:673–686. doi: 10.1016/j.jvolgeores.2008.06.028.

Johnson, J. B., 2003. Generation and propagation of infrasonic airwaves from volcanic explosions. *Journal of Volcanology and Geothermal Research*, 121:1–14. doi: 10.1016/s0377-0273(02)00408-0.

Johnson, J. B., Aster, R. C., Ruiz, M. C., Malone, S. D., McChesney, P. J., Lees, J. M. and Kyle, P. R., 2003. Interpretation and utility of infrasonic records from erupting volcanoes. *Journal of Volcanology and Geothermal Research*, 121:15–63. doi: 10.1016/s0377-0273(02)00409-2.

Johnson, J. B., Aster, R. C. and Kyle, P. R., 2004. Volcanic eruptions observed with infrasound. *Geophysical Research Letters*, 31:L14604. doi: 10.1029/2004GL020020.

Johnson, J. B. and Ripepe, M., 2011. Volcano infrasound: A review. *Journal of Volcanology and Geothermal Research*, 206:61–69. doi: 10.1016/j.jvolgeores.2011.06.006.

Kazahaya, K., Shinohara, H. and Saito, G., 1994. Excessive degassing of Izu-Oshima volcano: magma convection in a conduit. *Bulletin of Volcanology*, 56:207–216. doi: 10.1007/BF00279605.

Kling, G. W., Evans, W. C., Tanyileke, G., Kusakabe, M., Ohba, T., Yoshida, Y. and Hell, J. V., 2005. Degassing lakes nyos and monoun: Defusing certain disaster. *Proceedings of the National Academy of Sciences*, 102:14185 – 14190. doi: 10.1073/pnas.0502274102.

Kosloff, D. D. and Baysal, E., 1982. Forward modeling by a Fourier method. *Geophysics*, 47:1402–1412. doi: 10.1190/1.1441288.

Kremers, S., Hanson, J., Lavallée, Y., Hess, K.-U., Chevrel, O., Wassermann, J. and Dingwell, D., 2012. Shallow magma-mingling-driven Strombolian eruptions at Yasur volcano, Vanuatu. *Geophysical Research Letters*, 39:L21304. doi: 10.1029/2012GL053312.

Kremers, S., Wassermann, J., Meier, K., Pelties, C., van Driel, M., Vasseur, J. and Hort, M., 2013. Inverting the source mechanism of Strombolian Explosions at Mt. Yasur, Vanuatu, using a multi-parameter dataset. *Journal of Volcanology and Geothermal Research*, 262:104–122. doi: 10.1016/j.jvolgeores.2013.06.007.

Lautze, N. and Houghton, B., 2005. Physical mingling of magma and complex eruption dynamics in the shallow conduit at Stromboli volcano, Italy. *Geology*, 33:425–428. doi: 10.1130/G21325.1.

Lautze, N. and Houghton, B., 2007. Linking variable explosion style and magma textures during 2002 at Stromboli volcano, Italy. *Bulletin of Volcanology*, 69:445–460. 10.1007/s00445-006-0086-1.

Le Pichon, A., Blanc, E. and Hauchecorne, A. *Infrasound Monitoring for Atmospheric Studies*. Springer, 2009. ISBN 9781402095078.

Louat, R., Hamburger, M. and Monzier, M. Shallow and intermediate-depth seismicity in the New Hebrides arc: Constraints on the subduction process. In Greene, H. and Wong, F., editors, *Geology and Offshore Resources of Pacific Island Arcs – Vanuatu Region*, pages 329–356. Circum-Pacific Council for Energy and Mineral Resources Earth Science Series, 1988. ISBN 0933687095.

Lovejoy, S., Gaonach, H. and Schertzer, D., 2004. Bubble distributions and dynamics: The expansion-coalescence equation. *Journal of Geophysical Research*, 109:B11203. doi: 10.1029/2003JB002823.

Lowen, S. B. and Teich, M. C. *Fractal-based Point Processes*. Wiley-Interscience, 2005. ISBN 978-0471383765.

Lowen, S. B. and Teich, M. C., 1995. Estimation and simulation of fractal stochastic point processes. *Fractals*, 3:183–210. doi: 10.1142/S0218348X95000151.

Marble, F. E., 1970. Dynamics of dusty gases. *Annual Review of Fluid Mechanics*, 2:397–446. doi: 10.1146/annurev.fl.02.010170.002145.

Marchetti, E. and Ripepe, M., 2005. Stability of the seismic source during effusive and explosive activity at Stromboli volcano. *Geophysical Research Letters*, 32: L03307. doi: 10.1029/2004GL021406.

Marchetti, E., Ripepe, M., Harris, A. and Donne, D. D., 2009. Tracing the differences between Vulcanian and Strombolian explosions using infrasonic and thermal radiation energy. *Earth and Planetary Science Letters*, 279:273–281. doi: 10.1016/j.epsl.2009.01.004.

Marzocchi, W. and Bebbington, M. S., 2012. Probabilistic eruption forecasting at short and long time scales. *Bulletin of Volcanology*, 74:1777–1805. doi: 10.1007/s00445-012-0633-x.

Matoza, R., Le Pichon, A., Vergoz, J., Herry, P., Lalande, J., Lee, H., Che, I. and Rybin, A., 2011. Infrasonic observations of the June 2009 Sarychev Peak eruption, Kuril islands: Implications for infrasonic monitoring of remote explosive volcanism. *Journal of Volcanology and Geothermal Research*, 200:35–48. doi: 10.1016/j.jvolgeores.2010.11.022.

McGreger, A. D. and Lees, J. M., 2004. Vent discrimination at Stromboli volcano, Italy. *Journal of Volcanology and Geothermal Research*, 137:169–185. doi: 10.1016/j.jvolgeores.2004.05.007.

McNutt, S., 2005. Volcanic seismology. *Annual Review of Earth and Planetary Sciences*, 32:461–491. doi: 10.1146/annurev.earth.33.092203.122459.

Meier, K., Garaebiti, E., Gerst, A., Harrison, M., Hort, M., Kremers, S., Wassermann, J. and Weiss, B., 2009. Preliminary insights into an integrated geophysical approach for a better understanding of Strombolian activity at Yasur volcano, Vanuatu. *Eos Transactions AGU, Fall Meeting Supplement*, 90(52):V23D–2098.

Meier, K., Hort, M., Blender, R., Wassermann, J. and Garaebiti, E., 2014a. Temporal variability of normal Strombolian activity at Yasur volcano, Vanuatu. *in preparation*.

Meier, K., Hort, M., Wassermann, J. and Garaebiti, E., 2014b. Strombolian surface activity regimes at Yasur volcano, Vanuatu, as observed by Doppler radar, infrared camera and infrasound. *in preparation*.

Meijering, E., Dzyubachyk, O. and Smal, I. Methods for cell and particle tracking. In *Imaging and Spectroscopic Analysis of Living Cells: Optical and Spectroscopic Techniques*, Methods in Enzymology, pages 183 – 200. Academic Press, 2012. doi: 10.1016/B978-0-12-391857-4.00009-4.

Mercalli, G., 1881. Natura delle eruzioni dello Stromboli ed in generale dell' attività sismo-vulcanica delle Isole Eolie. *Atti della Società Italiana di Scienze Naturali*, 27:184–199.

Métrich, N., Allard, P., Aiuppa, A., Bani, P., Bertagnini, A., Shinohara, H., Parello, F., Dimuro, A., Garaebiti, E., Belhadj, O. and Massare, D., 2011. Magma and volatile supply to post-collapse volcanism and block resurgence in Siwi caldera (Tanna island, Vanuatu arc). *Journal of Petrology*, 52:1077–1105. doi: 10.1093/petrology/egr019.

Monzier, M., Maillet, P., Foyo Herrera, J., Louat, R., Missegue, F. and Pontoise, B., 1984. The termination of the southern New Hebrides subduction zone (southwestern Pacific). *Tectonophysics*, 101:177–184. doi: 10.1016/0040-1951(84)90050-7.

Moran, M. J. and Shapiro, H. N. *Fundamentals of Engineering Thermodynamics*. Wiley, 2007. ISBN 0471787353.

Mori, J., Patia, H., McKee, C., Itikarai, I., Lowenstein, P., De Saint Ours, P. and Talai, B., 1989. Seismicity associated with eruptive activity at Langila volcano, Papua New Guinea. *Journal of Volcanology and Geothermal Research*, 38:243–255. doi: 10.1016/0377-0273(89)90040-1.

Mori, T., Notsu, K., Tohjima, Y., Wakita, H., Nuccio, P. M. and Italiano, F., 1995. Remote detection of fumarolic gas chemistry at Vulcano, Italy, using an FT-IR spectral radiometer . *Earth and Planetary Science Letters*, 134:219–224. doi: 10.1016/0012-821X(95)00119-W.

Nabyl, A., Dorel, J. and Lardy, M., 1997. A comparative study of low-frequency seismic signals recorded at Stromboli volcano, Italy, and at Yasur volcano, Vanuatu. *New Zealand Journal of Geology and Geophysics*, 40:549–558. doi: 10.1080/00288306.1997.9514783.

Nairn, I. A., Scott, B. J. and Giggenbach, W. F., 1988. Yasur volcano investigations, Vanuatu, Sept 1988. *New Zealand Geological Survey Report G*, 136:1 – 74.

Namiki, A. and Manga, M., 2008. Transition between fragmentation and permeable outgassing of low viscosity magmas. *Journal of Volcanology and Geothermal Research*, 169:48–60. doi: 10.1016/j.jvolgeores.2007.07.020.

Neef, G., Zhao, J. X., Collerson, K. D. and Zhang, F. S., 2003. Late quaternary uplift and subsidence of the west coast of tanna, south vanuatu, southwest pacific: U–th ages of raised coral reefs in the median sedimentary basin. *Australian Journal of Earth Sciences*, 50:39–48. doi: 10.1046/j.1440-0952.2003.00972.x.

Newman, M. E. J., 2005. Power laws, Pareto distributions and Zipf"s law. *Contemporary Physics*, 46:323–351. doi: 10.1080/00107510500052444.

Oppenheimer, C., Bani, P., Calkins, J. A., Burton, M. R. and Sawyer, G. M., 2006. Rapid FTIR sensing of volcanic gases released by Stromboilian explosions at Yasur volcano, Vanuatu. *Applied Physics B: Lasers and Optics*, 85:453–460. doi: 10.1007/s00340-006-2353-4.

Palma, J. L., Blake, S. and Calder, E. S., 2011. Constraints on the rates of degassing and convection in basaltic open-vent volcanoes. *Geochemistry, Geophysics, Geosystems*, 12:Q11006. doi: 10.1029/2011GC003715.

Parfitt, E. A., 2004. A discussion of the mechanisms of explosive basaltic eruptions. *Journal of Volcanology and Geothermal Research*, 134:77–107. doi: 10.1016/j.jvolgeores.2004.01.002.

Parfitt, E. A. and Wilson, L., 1994. The 1983–86 Pu'u 'O'o eruption of Kilauea volcano, Hawaii: a study of dike geometry and eruption mechanisms for a long-lived eruption. *Journal of Volcanology and Geothermal Research*, 59:179–205. doi: 10.1016/0377-0273(94)90090-6.

Parfitt, E. A. and Wilson, L., 1995. Explosive volcanic eruptions: The transition between Hawaiian-style lava fountaining and Strombolian explosive activity. *Geophysical Journal International*, 121:226–232. doi: 10.1111/j.1365-246X.1995.tb03523.x.

Patrick, M. R., 2007. Dynamics of Strombolian ash plumes from thermal video: Motion, morphology, and air entrainment. *Journal of Geophysical Research*, 112:B06202. doi: 10.1029/2006JB004387.

Patrick, M., Harris, A., Ripepe, M., Dehn, J., Rothery, D. and Calvari, S., 2007. Strombolian explosive styles and source conditions: insights from thermal (FLIR) video. *Bulletin of Volcanology*, 69:769–784. doi: 10.1007/s00445-006-0107-0.

Pelanti, M. and Leveque, R. J., 2006. High-resolution finite volume methods for dusty gas jets and plumes. *Siam Journal on Scientific Computing*, 28:1335–1360. doi: 10.1137/050635018.

Pelletier, B., Calmant, S. and Pillet, R., 1998. Current tectonics of the Tonga-New Hebrides region. *Earth and Planetary Science Letters*, 164:263–276. doi: 10.1016/S0012-821X(98)00212-X.

Petersen, T., De Angelis, S., Tytgat, G. and McNutt, S. R., 2006. Local infrasound observations of large ash explosions at Augustine Volcano, Alaska, during January 11-28, 2006. *Geophysical Research Letters*, 33:L12303. doi: 10.1029/2006GL026491.

Polacci, M., Baker, D., Bai, L. and Mancini, L., 2008. Large vesicles record pathways of degassing at basaltic volcanoes. *Bulletin of Volcanology*, 70:1023–1029. doi: 10.1007/s00445-007-0184-8.

Prousevitch, A. A., Sahagian, D. L. and Anderson, A. T., 1993. Dynamics of diffusive bubble growth in magmas: Isothermal case. *Journal of Geophysical Research*, 98: 22283–22307. doi: 10.1029/93JB02027.

Ripepe, M., Rossi, M. and Saccorotti, G., 1993. Image processing of explosive activity at Stromboli. *Journal of Volcanology and Geothermal Research*, 54:335–351. doi: 10.1016/0377-0273(93)90071-X.

Ripepe, M., Poggi, P., Braun, T. and Gordeev, E., 1996. Infrasonic waves and volcanic tremor at Stromboli. *Geophysical Research Letters*, 23:181–184. doi: 10.1029/95GL03662.

Ripepe, M., Marchetti, E., Poggi, P., Harris, A. J. L., Fiaschi, A. and Ulivieri, G., 2004. Seismic, acoustic, and thermal network monitors the 2003 eruption of Stromboli volcano. *Eos Transactions AGU*, 85:329–332. doi: 10.1029/2004EO350001.

Ripepe, M., Harris, A. and Marchetti, E., 2005a. Coupled thermal oscillations in explosive activity at different craters of Stromboli volcano. *Geophysical Research Letters*, 32:L17302. doi: 10.1029/2005GL022711.

Ripepe, M., Marchetti, E., Ulivieri, G., Harris, A., Dehn, J., Burton, M., Tommaso, C. and Giuseppe, S., 2005b. Effusive to explosive transition during the 2003 eruption of Stromboli volcano. *Geology*, 33:341–344. doi: 10.1130/G21173.1.

Ripepe, M., Marchetti, E. and Ulivieri, G., 2007. Infrasonic monitoring at Stromboli volcano during the 2003 effusive eruption: Insights on the explosive and degassing process of an open conduit system. *Journal of Geophysical Research*, 112:B09207. doi: 10.1029/2006JB004613.

Ripepe, M., Donne, D. D., Harris, A., Marchetti, E. and Ulivieri, G. Dynamics of Strombolian activity. In *The Stromboli Volcano: An Integrated Study of the 2002–2003 Eruption*, Geophysical Monograph Series, pages 39–48. American Geophysical Union, 2008. doi: 10.1029/182GM05.

Ripepe, M., Donne, D. D., Lacanna, G., Marchetti, E. and Ulivieri, G., 2009. The onset of the 2007 Stromboli effusive eruption recorded by an integrated geophysical network. *Journal of Volcanology and Geothermal Research*, 182:131–136. doi: 10.1016/j.jvolgeores.2009.02.011.

Ripepe, M. and Gordeev, E., 1999. Gas bubble dynamics model for shallow volcanic tremor at Stromboli. *Journal of Geophysical Research*, 104:10639–10654. doi: 10.1029/98JB02734.

Ripepe, M. and Marchetti, E., 2002. Array tracking of infrasonic sources at Stromboli volcano. *Geophysical Research Letters*, 29:L2076. doi: 10.1029/2002GL015452.

Ripepe, M., Harris, A. J. and Carniel, R., 2002. Thermal, seismic and infrasonic evidences of variable degassing rates at Stromboli volcano. *Journal of Volcanology and Geothermal Research*, 118:285–297. doi: 10.1016/s0377-0273(02)00298-6.

Robin, C., Eissen, J. P. and Monzier, M., 1994. Ignimbrites of basaltic andesite and andesite compositions from Tanna, New Hebrides Arc. *Bulletin of Volcanology*, 56:10–22. doi: 10.1007/BF00279725.

Robock, A., 2002. Pinatubo eruption - The climatic aftermath. *Science*, 295(5558): 1242–1244. doi: DOI:10.1126/science.1069903.

Sahetapy-Engel, S. T. M., Flynn, L. P., Harris, A. J. L., Bluth, G. J., Rose, W. I. and Matias, O., 2004. Surface temperature and spectral measurements at Santiaguito lava dome, Guatemala. *Geophysical Research Letters*, 31:L19610. doi: 10.1029/2004GL020683.

Scarpa, R. and Tilling, R. *Monitoring and Mitigation of Volcano Hazards*. Springer, 1996. ISBN 9783540607137.

Scharff, L., Hort, M., Harris, A., Ripepe, M., Lees, J. and Seyfried, R., 2008. Eruption dynamics of the SW crater of Stromboli volcano, Italy – An interdisciplinary approach. *Journal of Volcanology and Geothermal Research*, 176:565–570. doi: 10.1016/j.jvolgeores.2008.05.008.

Scharff, L., Ziemen, F., Hort, M., Gerst, A. and Johnson, J. B., 2012. A detailed view into the eruption clouds of Santiaguito volcano, Guatemala, using Doppler radar. *Journal of Geophysical Research*, 117:B04201. doi: 10.1029/2011JB008542.

Schmincke, H. U. *Volcanism.* Springer, 2004. ISBN 3540436502.

Settle, M. and McGetchin, T. R., 1980. Statistical analysis of persistent explosive activity at stromboli, 1971: Implications for eruption prediction. *Journal of Volcanology and Geothermal Research*, 8:45–58. doi: 10.1016/0377-0273(80)90006-2.

Simkin, T. and Siebert, L. *Volcanoes of the World: A Regional Directory, Gazetteer, and Chronology of Volcanism during the last 10,000 Years.* Geoscience Press, 1994. ISBN 0945005121.

Small, C. and Naumann, T., 2001. The global distribution of human population and recent volcanism. *Global Environmental Change B: Environmental Hazards*, 3:93–109. doi: 10.1016/S1464-2867(02)00002-5.

Spampinato, L., Oppenheimer, C., Cannata, A., Montalto, P., Salerno, G. and Calvari, S., 2012. On the time-scale of thermal cycles associated with open-vent degassing. *Bulletin of Volcanology*, 74:1281–1292. doi: 10.1007/s00445-012-0592-2.

Spampinato, L., Calvari, S., Oppenheimer, C. and Boschi, E., 2011. Volcano surveillance using infrared cameras. *Earth-Science Reviews*, 106:63–91. doi: 10.1016/j.earscirev.2011.01.003.

Sparks, R., 1978. The dynamics of bubble formation and growth in magmas: A review and analysis. *Journal of Volcanology and Geothermal Research*, 3:1–37. doi: 10.1016/0377-0273(78)90002-1.

Spieler, O., Kennedy, B., Kueppers, U., Dingwell, D., Scheu, B. and Taddeucci, J., 2004. The fragmentation threshold of pyroclastic rocks. *Earth and Planetary Science Letters*, 226:139–148. doi: 10.1016/j.epsl.2004.07.016.

Stauffer, D. and Aharony, A. *Introduction to Percolation Theory.* Taylor and Francis, 1991. ISBN 0748402535.

Stevenson, D. S. and Blake, S., 1998. Modelling the dynamics and thermodynamics of volcanic degassing. *Bulletin of Volcanology*, 60:307–317. doi: 10.1007/s004450050234.

Stroberg, T. W., Manga, M. and Dufek, J., 2010. Heat transfer coefficients of natural volcanic clasts. *Journal of Volcanology and Geothermal Research*, 194:214–219. doi: 10.1016/j.jvolgeores.2010.05.007.

Taddeucci, J., Pompilio, M. and Scarlato, P., 2002. Monitoring the explosive activity of the July–August 2001 eruption of Mt. Etna (Italy) by ash characterization. *Geophysical Research Letters*, 29:1230. doi: 10.1029/2001GL014372.

Taddeucci, J., Pompilio, M. and Scarlato, P., 2004. Conduit processes during the July–August 2001 explosive activity of Mt. Etna (Italy): Inferences from glass chemistry and crystal size distribution of ash particles. *Journal of Volcanology and Geothermal Research*, 137:33–54. doi: 10.1016/j.jvolgeores.2004.05.011.

Taddeucci, J., Scarlato, P., Capponi, A., Del Bello, E., Cimarelli, C., Palladino, D. M. and Kueppers, U., 2012. High-speed imaging of Strombolian explosions: The ejection velocity of pyroclasts. *Geophysical Research Letters*, 39:L02301. doi: 10.1029/2011GL050404.

Taylor, F. W., Bevis, M. G., Schutz, B. E., Kuang, D., Recy, J., Calmant, S. S., Charley, D., Reigner, M., Perin, B., Jackson, M. and Reichenfeld, C., 1995. Geodetic measurements of convergence at the New Hebrides island arc indicate arc fragmentation caused by an impinging aseismic ridge. *Geology*, 23:1011–1014. doi: 10.1130/0091-7613.

Telesca, L., Cuomo, V., Lapenna, V. and Macchiato, M., 2002. Time-clustering analysis of volcanic occurrence sequences. *Physics of the Earth and Planetary Interiors*, 131:47–62. doi: 10.1016/S0031-9201(02)00015-8.

Thurner, S., Lowen, S. B., Feurstein, M. C., Feichtinger, H. G. and Teich, M. C., 1997. Analysis, synthesis, and estimation of fractal-rate stochastic point processes. *Fractals*, 5:565–596. doi: 10.1142/S0218348X97000462.

Tinti, S., Maramai, A., Armigliato, A., Graziani, L., Manucci, A., Pagnoni, G. and Zaniboni, F., 2006. Observations of physical effects from tsunamis of December 30, 2002 at Stromboli volcano, southern Italy. *Bulletin of Volcanology*, 68:450–461. doi: 10.1007/s00445-005-0021-x.

Torrence, C. and Compo, G. P., 1998. A practical guide to wavelet analysis. *Bulletin of the American Meteorological Society*, 79:61–78. doi: 10.1175/1520-0477(1998)079<0061:APGTWA>2.0.CO;2.

Turcott, R. G. and Teich, M. C., 1996. Fractal character of the electrocardiogram: Distinguishing heart-failure and normal patients. *Annals of Biomedical Engineering*, 24:269–293. doi: 10.1007/BF02667355.

Turcotte, D. L., 1999. Self-organized criticality. *Reports on Progress in Physics*, 62: 1377–1429. doi: 10.1088/0034-4885/62/10/201.

Valentine, G. and Wohletz, K., 1989. Numerical models of Plinian eruption columns and pyroclastic flows. *Journal of Geophysical Research*, 94(B2):1867–1887. doi: doi:10.1029/JB094iB02p01867.

Vergniolle, S., 1996. Bubble size distribution in magma chambers and dynamics of basaltic eruptions. *Earth and Planetary Science Letters*, 140:269–279. doi: 10.1016/0012-821X(96)00042-8.

Vergniolle, S. and Jaupart, C., 1990. Dynamics of degassing at Kilauea volcano, Hawaii. *Journal of Geophysical Research*, 95:2793–2809. doi: 10.1029/JB095iB03p02793.

Vergniolle, S. and Brandeis, G., 1996. Strombolian explosions: A large bubble breaking at the surface of a lava column as a source of sound. *Journal of Geophysical Research*, 101:20433–20447. doi: 10.1029/96JB01178.

Vergniolle, S. and Jaupart, C., 1986. Separated two-phase flow and basaltic eruptions. *Journal of Geophysical Research*, 91:12842–12860. doi: 10.1029/JB091iB12p12842.

Vergniolle, S., Brandeis, G. and Mareschal, J.-C., 1996. Strombolian explosions: Eruption dynamics determined from acoustic measurements. *Journal of Geophysical Research*, 101:20449–20466. doi: 10.1029/96JB01925.

Vergniolle, S., Boichu, M. and Caplan-Auerbach, J., 2004. Acoustic measurements of the 1999 basaltic eruption of Shishaldin volcano, Alaska: Origin of Stromolian activity. *Journal of Volcanology and Geothermal Research*, 137:109–134. doi: 10.1016/j.jvolgeores.2004.05.003.

Vicari, A., Ganci, G., Behncke, B., Cappello, A., Neri, M. and Negro, D., 2011. Near-real-time forecasting of lava flow hazards during the 12–13 January 2011 Etna eruption. *Geophysical Research Letters*, 38:L13317. doi: doi:10.1029/2011GL047545.

Vöge, M. and Hort, M., 2009. Installation of a Doppler radar monitoring system at Merapi volcano, Indonesia. *IEEE Transactions on Geoscience and Remote Sensing*, 47:251–271. doi: 10.1109/TGRS.2008.2002693.

Wagner, R. Der SO_2-Fluss am Mount Yasur, Vanuatu. Bachelorsthesis, Institut für Geophysik, University of Hamburg, 2011.

Walk, F. Entschluesselung der Eruptionsdynamik des Yasur mittels thermischer Beobachtungen. Bachelorsthesis, Institut für Geophysik, University of Hamburg, 2010.

Walker, G., 1990. Review article: Geology and volcanology of the Hawaiian islands. *Pacific Science*, 44:315–347. ISSN 0030-8870.

Waythomas, C. F., Pierson, T. C., Major, J. J. and Scott, W. E., 2012. Voluminous ice-rich and water-rich lahars generated during the 2009 eruption of Redoubt volcano, Alaska. *Journal of Volcanology and Geothermal Research*, 259:389–413. doi: 10.1016/j.jvolgeores.2012.05.012.

Wilson, L. and Self, S., 1980. Volcanic explosion clouds: Density, temperature, and particle content estimates from cloud motion. *Journal of Geophysical Research*, 85:2567–2572. doi: 10.1029/JB085iB05p02567.

Wilson, L. and Head, J. W., 1981. Ascent and eruption of basaltic magma on the earth and moon. *Journal of Geophysical Research*, 86:2971–3001. doi: 10.1029/JB086iB04p02971.

Woulff, G. and McGetchin, T., 1976. Acoustic noise from volcanoes: Theory and experiment. *Geophysical Journal of the Royal Astronomical Society*, 45:601–616. doi: 10.1111/j.1365-246X.1976.tb06913.x.

Acknowledgements

An dieser Stelle möchte ich mich bei allen bedanken, die mir bei der Erstellung dieser Doktorarbeit geholfen haben.

Mein besonderer Dank gilt Herrn Prof. Matthias Hort für die Betreuung und die Unterstützung dieser Arbeit. Er hat mich ermutigt den Schritt in die Vulkanologie zu wagen, und die Gespräche mit ihm haben im wesentlichen zum Gelingen dieser Arbeit beigetragen.

Ebenfalls danke ich Joachim Wassermann für den gemeinsamen wissenschaftlichen Austausch und die Unterstützung des gesamten Vanuatu-Projektes. Ausserdem möchte ich ihm dafür danken, dass er sich als Zweitgutachter zur Verfügung gestellt hat.

Ich danke auch Richard Blender für die Diskussionen zum pinken Rauschen und der selbst-organisierten Kritikalität. Diese haben mir eine neue Welt eröffnet. Spezieller Dank gebührt zudem Ekkehart Tessmer für den Austausch zur Wellenausbreitung.

Für den Aufenthalt am Yasur möchte ich mich bei der Leiterin des Vanuatu Geohazards Observatory Esline Garaebiti und Ihren Mitarbeitern bedanken. Sie haben das Projekt mit Kräften gefördert, ohne die es nicht gelungen wäre. Zudem danke ich Maurizio Ripepe und seinem Team für die immer wieder wunderbare Arbeit am Stromboli.

Des Weiteren bedanke ich mich bei allen Mitgliedern der Arbeitsgruppe Vulkanologie. Ganz besonders danke ich Alexander Gerst, dafür dass ich von ihm lernen durfte und für die schöne gemeinsame Zeit. Großer Dank gebührt auch Lea Scharff für die Diskussionen wissenschaftlicher aber auch jeglich anderer Natur. Außerdem danke ich Jörg Hasenclever für die netten spontanen Pausen zwischen Tür und Angel.

Auch allen anderen Mitarbeitern des Instituts für Geophysik sei an dieser Stelle für die gute und entspannte Arbeitsatmosphäre gedankt. Besonders die Zeit mit Christian, Bene, und Sönke hat immer wieder für die nötige Entspannung gesorgt.

Die gemeinsamen Gespräche mit Sebastian waren auch jedes Mal sehr erfreulich. Ein ganz spezieller Dank geht weiterhin an Christel Mynarik für ihre Hilfe in ganz unterschiedlichen Angelegenheiten.

Abschließend möchte ich mich bei allen bedanken, die mir diese Arbeit ermöglicht haben:

Ein ganz, ganz großer Dank geht an meine Eltern und meine Schwester. Vielen Dank dafür, dass ich in anstrengenden Phasen immer wieder abschalten und neue Energie tanken konnte, auch in Form von leckerstem Essen.

Allen meinen lieben Freunden danke ich für ihre Geduld und ihr Verständnis für diese Arbeit. Ihre Freundschaft bedeutet mir sehr viel.

Schließlich gilt mein tiefster Dank Micha. Seine ausdauernde und liebevolle Unterstützung hat mich durch einen Großteil dieser Arbeit getragen.

Das Vanuatu-Projekt wurde von der Deutschen Forschungsgemeinschaft unter HO 1411 17-1, 17-2 und WA 1493 4-1 gefördert.

Hiermit erkläre ich an Eides statt, dass ich die vorliegende Dissertationsschrift selbst verfasst und keine anderen als die angegebenen Quellen und Hilfsmittel benutzt habe.

Hamburg, den 12. Mai 2014

Kristina Meier